



PHYSICS



EMERGING THEMES IN FUNDAMENTAL
AND APPLIED SCIENCES



EDITORS

RABA'AH SYAHIDAH AZIS

MOHD MUSTAFA AWANG KECHIK

**EMERGING THEMES IN FUNDAMENTAL AND APPLIED
SCIENCES - PHYSICS**

Editors

Raba'ah Syahidah Azis

Mohd Mustafa Awang Kechik

**Faculty of Science
Universiti Putra Malaysia
Serdang
Selangor
Malaysia**

**UPM Press
Universiti Putra Malaysia
Serdang
Selangor
Malaysia**

Hak Cipta Universiti Putra Malaysia
Copyright Universiti Putra Malaysia, 2018
Universiti Putra Malaysia

Hak cipta terpelihara.

Tiada bahagian daripada buku ini boleh diterbitkan semula, disimpan untuk pengeluaran atau ditukarkan ke dalam sebarang bentuk atau dengan sebarang alat, sama ada dengan cara elektronik, gambar serta rakaman dan sebagainya tanpa kebenaran bertulis daripada Penerbit UPM terlebih dahulu

All right reserved.

No part of this publication may be reproduced or transmitted in any form or by any means, electronic or mechanical including photocopy, recording, or any information storage and retrieval system, without permission in writing from UPM Press

Diterbitkan di Malaysia oleh/Published in Malaysia by

Penerbit UPM

Universiti Putra Malaysia

43400 UPM, Serdang Selangor

Hakcipta terpelihara: www.science.upm.edu.my/ebook-3213

Perpustakaan Negara Malaysia

Cataloguing-in Publication Data/ Data pengkatalogan- dalam- Penerbitan

Emerging Themes in Fundamental and Applied Sciences - Physics

Editor: Dr. Raba'ah Syahidah Azis dan Dr. Mohd Mustafa Awang Kechik

eISBN 978-967-334-813-5

TABLE OF CONTENTS

Preface

Contributors

Chapter 1 Introduction

Chapter 2 Theoretical Quantum Physics

2.1 Interactive quantum harmonic oscillator with C++

2.2 First Passage Time Problem on Growing Geometrical Network

Chapter 3 Magnetic Materials and Their Applications

3.1 Structure, Magnetic and Magneto-transport Properties of La-Sr-Mn-O/NiO Composite

3.2 Structural properties of yttrium aluminum iron garnet (YAIG) nanoferrite prepared via auto combustion sol-gel synthesis

3.3 Microwave-absorbing properties of $\text{Sr}_4\text{Me}_2\text{Fe}_{36}\text{O}_{60}$ Me= (Mg-Zn, Mn-Zn) composite in X-band and Ku-band frequencies

3.4 Role of Magnetite Nanoparticles for Metal Absorbents in Waste Water Treatment

3.5 The structural and magnetic behavior of Yttrium Iron Garnet ($\text{Y}_3\text{Fe}_5\text{O}_{12}$) nanoparticles

Chapter 4 Superconductors and Their Applications

4.1 Development of Bi-2212 via Thermal Treatment Method Using PVP as Capping Agent

4.2 The comparative studies of YBCO prepared by co-precipitation and thermal treatment Methods

Chapter 5 Metal Oxide Varistor and Their Applications

5.1 The effect of sintering time on the microstructural and nonlinear electrical properties of Zn-V-Mn-Nb-Gd-O low-voltage varistor ceramics

Chapter 6 Carbon Nanomaterials

6.1 Synthesis of carbon nanomaterials by chemical vapor deposition: Effect of catalyst

Chapter 7 Surface and Coating Technology

7.1 Effects of PTFE coating on the Stainless Steel Surface for the Reduction of Powder Stickiness during Spray Drying Process

Chapter 8 WLAN Positioning System

8.1 WLAN Positioning Based on Enhanced k-Nearest Neighbour Classifier

PREFACE

This book is a compilation of research papers presented at the Fundamental Science Congress 2017 at Universiti Putra Malaysia on November 21-22, 2017. The congress served as a platform for scientific researchers from Malaysia and across the world to share their knowledge, initiate collaboration and to establish network. Participants are involved the academician, researchers and postgraduate students in the field of pure sciences (biologists, chemists, physicists), applied sciences (engineers, biomedical scientists). Researchers and administrators from the industry are also join and contribute ideas and viewpoints from the industrial perspective. This book presents the research findings in various fields of ranging from fundamental physics, material science and technology in the field of magnetic materials, superconductors, metal oxides varistors, nanomaterials, surface coatings and WLAN networking principles. All the authors are researchers in various universities from Malaysia as well as from overseas.

Chapter 2 comprises papers on theoretical and computational works that covers the aspect of quantum harmonic oscillator in C++ programming language and the construction of mean first passage time (MFPT) on a growing geometrical network via hyperbolic tessellation of modular group are presented in this chapter.

Chapter 3 consist papers discusses the magnetic and electrical properties of magnetic solid materials. The papers discussed the properties of ceramic ferrites, nanocomposites and magnetic nanoparticles. These material has high potential application as magnetic field sensing element (based on magnetoresistive effect), ceramic ferrites and absorbing materials (RAM). Review on magnetic nanoparticles for metal removal in waste water treatment process (WWT) also highlighted.

Chapter 4 covers papers related to the properties of oxide superconductors depend strongly on the techniques and processing conditions used to synthesis the bulk sample. Unlike the conventional solid state method, wet methods are proven to yield better results in terms of homogeneity and better control of stoichiometry since the materials and reactions can be chemically controlled to obtain the desired product Co-precipitation method (COP) and thermal treatment method (TT) are two of the wet methods used in this study.

Chapter 5 highlight the electrical properties of metal oxides varistors ceramics. The purpose of the work is to investigate the effect of sintering time on the microstructural and the nonlinear electrical properties of the low voltage varistors ceramics.

Chapter 6 comprises the synthesis of carbon nanomaterials (CNMs) using chemical vapour deposition (CVD) technique. The paper highlight the production of carbon nanomaterials using different type of catalyst. CVD-synthesized carbon nanotubes has been produces by using iron oxide (Fe_3O_4) and nickel oxide (NiO) powder as a catalyst and copper (Cu) foil used as catalyst to produce graphene films.

Chapter 7 covers a paper related to a chemical surface coating using spray drying process. This paper feature a simple surface coating modification using polytetrafluoroethylene on the stainless steel slide as one of the potential to reduce the powder stickiness on the wall of spray dryer.

Chapter 8 covers a paper that talks about the development of an enhanced k-Nearest Neighbor (kNN) classifier algorithm for positioning in wireless local area network (WLAN). The main

principle of the algorithm is based on statistical learning classification technique. The algorithm is build and tested in realistic WLAN environment. The proposed algorithm is efficient in different WLAN environment conditions such as in reduced number of fingerprint samples and lower number of access points.

Raba'ah Syahidah Azis

CONTRIBUTORS

PREFACE

Raba'ah Syahidah Azis, Department of Physics, Faculty of Science, Universiti Putra Malaysia, 43400 Serdang, Selangor, Malaysia.

CHAPTER 1 INTRODUCTION

Raba'ah Syahidah Azis, Department of Physics, Faculty of Science, Universiti Putra Malaysia, 43400 Serdang, Selangor, Malaysia.

CHAPTER 2 THEORETICAL QUANTUM PHYSICS

2.1 Nurisya Mohd Shah^{1,2} and Siti Rahimah Sarnua¹

¹Department of Physics, Faculty of Science, Universiti Putra Malaysia, 43400 Serdang, Selangor, Malaysia.

²Laboratory of Computational Sciences & Mathematical Physics, Institute for Mathematical Research (INSPEM), 43400 UPM Serdang, Selangor, Malaysia.
risya@upm.edu.my

2.2 Nurul Nasha Amalina Shamsul Kamal¹, Chan Kar Tim^{1, 2}, Nurisya Mohd Shah^{1, 2} and Hishamuddin Zainuddin^{1, 2}

¹Laboratory of Computational Sciences and Mathematical Physics, Institute for Mathematical Research (INSPEM), Universiti Putra Malaysia, Malaysia.

²Department of Physics, Faculty of Science, Universiti Putra Malaysia, 43400 UPM Serdang, Selangor, Malaysia.
chankt@upm.edu.my

CHAPTER 3 MAGNETIC MATERIALS AND APPLICATIONS

3.1 Lim Kean Pah, Abdul Halim Shaari, Jumiah Hassan, Chen Soo Kien, Mohd Mustafa Awang Kechik, Ng Siau Wei and Tan Chew Ling

Department of Physics, Faculty of Science, Universiti Putra Malaysia, 43400 Serdang, Selangor, Malaysia.

limkp@upm.edu.my

3.2 Makiyyu Abdullahi Musa^{1, 3}, Raba'ah Syahidah Azis^{1, 2}, Nurul Huda Osman¹ and Jumiah Hassan^{1,2}

¹Department of Physics, Faculty of Science, University Putra Malaysia, 43400 UPM, Serdang, Selangor, Malaysia

²Institute of Advanced Materials, Universiti Putra Malaysia, 43400 UPM Serdang, Selangor, Malaysia

³Department of Science Laboratory Technology, Hussaini Adamu Federal Polytechnic, 705101 Kazaure, Nigeria

rabaah@upm.edu.my

3.3 Muhammad Misbah Muhammad Zulkimi¹, Raba'ah syahidah Azis^{1,2}, Ismayadi Ismail¹, Khamirul Amin Matori^{1,2}, Zulkifly Abbas², Fadzidah Mohd Idris¹, Farah Nabilah Binti Shafiee¹

¹Materials Synthesis and Characterisation Laboratory, Institute of Advanced Technology (ITMA),Universiti Putra Malaysia,43400 Serdang, Selangor.

²Physics Department, Faculty of Science,Universiti Putra Malaysia,43400 Serdang, Selangor, Malaysia.

rabaah@upm.edu.my

3.4 Nur Asyikin Ahmad Nazri^{1,3}, Raba'ah Syahidah Azis^{1,2}, Abdul Halim Shaari¹, Norlaily Mohd Saiden², Ismayadi Ismail¹, Jumiah Hassan^{1,2} and Hasfalina Che Man⁴

¹Materials Synthesis and Characterisation Laboratory, Institute of Advanced Technology (ITMA), Universiti Putra Malaysia, 43400 Serdang, Selangor, Malaysia.

²Physics Department, Faculty of Science, Universiti Putra Malaysia, 43400 Serdang, Selangor.

³Universiti Teknologi MARA, Cawangan Selangor, Malaysia.

⁴Department of Biological and Agricultural Engineering, Faculty of Engineering, Universiti Putra Malaysia, 43400 Serdang, Selangor, Malaysia.

rabaah@upm.edu.my

3.5 Raba'ah Syahidah Azis^{1,2}, Nuraine Mohd Shahrani² and Jumiah Hassan^{1,2}

¹Physics Department, Faculty of Science, Universiti Putra Malaysia, 43400 Serdang, Selangor, Malaysia.

²Materials Synthesis and Characterisation Laboratory, Institute of Advanced Technology (ITMA), Universiti Putra Malaysia, 43400 Serdang, Selangor, Malaysia.

rabaah@upm.edu.my

CHAPTER 4 SUPERCONDUCTORS AND APPLICATIONS

4.1 Safia Izzati Abd Sukor, Mohd Mustafa Awang Kechik, Abdul Halim Shaari, Chen Soo Kien, Hussein Baqiah

Laboratory of Superconductor & Thin Film, Department of Physics, 43400 UPM Serdang, Selangor
mmak@upm.edu.my

4.2 Nur Nabilah Mohd. Yusuf, Mohd Mustafa Awang Kechik, Abdul Halim Shaari, Chen Soo Kien and Hussein Baqiah

Laboratory of Superconductor & Thin Film, Department of Physics, Faculty of Science, 43400 UPM Serdang, Selangor, Malaysia
mmak@upm.edu.my

CHAPTER 5 METAL OXIDE VARISTOR

5.1 Nor Hasanah Isa¹, Rabaah Syahidah Azis^{1,2}, Nor Kamilah Sa'at¹, Azmi Zakaria¹, Raheleh Mohammadi¹ and Rosnu Kinsu¹

¹Department of Physics, Faculty of Science, Universiti Putra Malaysia, 43400 UPM Serdang, Selangor, Malaysia.

²Materials Synthesis and Characterisation Laboratory, Institute of Advanced Technology, Universiti Putra Malaysia, 43400 Serdang, Selangor, Malaysia.

rabaah@upm.edu.my

CHAPTER 6 CARBON NANOMATERIALS

6.1 Yazid Yaakob¹, Mohammad Adib Hazan¹, Ellyanie Balqis Hasmuei¹, Mackinley Bujang Anak Guma¹, Mohamad Shuhazly Mamat¹, Mohamad Saufi Rosmi², Subash Sharma³, and Masaki Tanemura³

¹Department of Physics, Faculty of Science, Universiti Putra Malaysia (UPM), Serdang, Selangor, Malaysia.

²Department of Chemistry, Faculty of Science and Mathematics, Universiti Pendidikan Sultan Idris (UPSI), Tanjung Malim, Selangor, Malaysia.

³Department of Frontier Materials, Nagoya Institute of Technology, Nagoya, Japan.

yazidakob@upm.edu.my

CHAPTER 7 SURFACE AND COATING TECHNOLOGY

7.1 Nadiah Ramlan, Mohamad Yusof Maskat, Saiful Irwan Zubairi

School of Chemical Sciences and Food Technology, Faculty of Science and Technology, Universiti Kebangsaan Malaysia, 43600 UKM Bangi, Selangor, Malaysia.

saiful-z@ukm.edu.my

CHAPTER 8 WLAN POSITIONING SYSTEM

8.1 Mohd Amiruddin Abd Rahman and Zulkifly Abbas

Department of Physics, Faculty of Science, Universiti Putra Malaysia, 43400 UPM Serdang, Selangor, Malaysia.

mohdamir@upm.edu.my

CHAPTER 1

INTRODUCTION

This book covers multidisciplinary areas in Physics encompassing theoretical physics, materials science and technology in the field of magnetic materials, superconductors, varistors, carbon nanomaterials and sensor applications. It also includes the synthesis and fabrication of materials and their properties. The aim is to provide a combination of different fields of scientific researches. It is hoped that it will meet the needs of a wider group of researchers comprising the physicist, metallurgist, materials scientists and postgraduates.

Theoretical physics features the quantum field theory (QFT), a theoretical framework used to construct quantum mechanical models of subatomic particles in particle physics and condensed matter physics. This involves mathematical tools that combine quantum mechanics. The interactive quantum harmonic oscillator using C++ is commonly used to solve the quantum harmonic oscillator (QHO) problem in atoms and molecules in solid solutions. The properties of mean first passage time (MFPT) on a growing geometrical network (GGN) constructed using hyperbolic tessellation is also a problem solving technique used in QFT.

A number of researches investigating the magnetic phenomena in a broad range of magnetic materials and magnetic structures are becoming important nowadays. The research involve efforts to gain fundamental understanding of technologically-important phenomena in solids, nanocomposites and technique development to devise new experimental tools for probing and characterizing magnetic behaviours. The synthesis of new magnetic materials and structures include multilayer nanocomposite, colossal magnetoresistance (CMR), and micro/nanostructured materials.

Recently, superconductivity has an attractive application in power system, engineering, medicine, electronics and transport. The most prominent application of superconductivity is superconducting magnets. Many magnets such as NMR magnets, MRI magnets and accelerators have applications in low temperature superconductors.

Carbon nanomaterials research attracted significant attention due to their unique properties for chemical, electronic, thermal, optical, mechanical, etc. This provides researchers opportunities to significant advances in fundamental and applied science technologies and applications. Carbon nanotubes (CNTs), and recently graphene, have become more versatile platforms for designing new materials research and device architectures. Carbon nanomaterials are important for chemical sensors, microwave high-frequency devices and alternative energy.

To date, research on novel coating materials and design has actively explored for composites, metastable materials, multilayers, micro/nano structures, vacuum and plasma-based deposition, thin film and process characterization, simulation, and modelling. The research and development on innovative deposition technique for hard and protective coatings are more important in industrial applications.

Raba'ah Syahidah Azis

CHAPTER 2

THEORETICAL QUANTUM PHYSICS

2.1 Interactive quantum harmonic oscillator with C++

Nurisya Mohd Shah and Siti Rahimah Sarnua

Abstract

In the study of atoms, molecules and solids, the basic task of quantum theory would be to solve the time-independent Schrodinger equation for which the solution consist of the energy eigenvalues and also the corresponding eigenfunctions of a given quantum mechanical system. The aim is to solve the quantum harmonic oscillator (QHO) problem. In this work, the problem of QHO using the C++ computer programming language was constructed. To be specific, the Dev C++ IDE software as the C++ development tools was used. As results, a more interactive quantum harmonic oscillator which will be very useful to improve the understanding of the QHO was developed.

Keywords: quantum harmonic oscillator, C++ programming, energy eigenvalues, eigenfunctions

Introduction

Quantum harmonic oscillator (QHO) is one of the important physical model in quantum mechanical system and works related to QHO, is up to this date is still a very active research area. Physical systems that could be benefited from the study of QHO model is varied from thermodynamics with master equation technique, Prado et.al (2017) and Barranco (2016), optics for example Carreno and Laussy (2016), molecular and nuclear vibrations, Tannoudji et.al (1977) and many others. The essential features of problem involving QHO is finding its solution. The QHO model generates the so-called exactly solvable potential, Griffith (2014). The potential is exactly solvable, namely one could construct the energy values and its associated states (wavefunction) of the oscillator up to n discrete values of both energy and states, Tannoudji et.al (1977). Since the result is well-known, computational work which consist of numerical and analytical type of results could be carried out.

Computer simulation per se have long known to provide influential results to increase the understanding towards particular realization of any physical systems, Daneshjo (2011). Computational method for general solution to Schrodinger equation with different type of potentials can be found in Zettili, (2009) and Konstantinos (2016). In this project, a computer simulation of the one-dimensional QHO is developed using the language of C++. The program is designed such that, user will experience on how the exactly solvable potential of QHO is obtained by choosing specific n states of QHO. In every quantum mechanics text books, topics on the solution to QHO mostly deals with analytical solutions which involved well-known polynomials representing the QHO states. With the current program, users could not only visualized the states as being harmonic but also could obtained the numerical values from the graph plotted.

In section two, preliminary method on quantum harmonic potential and essential notations

is given. This part emphasizes the main features of QHO that will be obtained and used in developing the C++ program. Methods of the programming part is also listed out. Section three discuss on the outcome of the program and finally follow by the conclusion.

Materials and Methods

Let a particle is represented by a wavefunction $\phi(x)$ (or the state) in one-dimensional space satisfy the time-independent Schrodinger equation

$$\frac{\hbar^2}{2m} \frac{d^2\phi}{dx^2} + \frac{1}{2}m\omega^2x^2\phi = E\phi, \quad (1)$$

where \hbar is the reduced Planck constant, ω is the angular frequency and E is the energy. Eq. (1) is the equation to solve the so-called quantum harmonic oscillator which physically analogous to the classical harmonic oscillator discussing Hooke's Law, Griffith (2014). Generally, harmonic oscillator is the simplest potential that produce a periodic motion, which can be described in both classical and quantum mechanics. Schott (2010) stated that the harmonic oscillator is the simplest oscillation that characterised by sine or cosine time functions and could be described by second order linear differential equation with constant coefficient namely Eq. (1).

In quantum mechanics, harmonic oscillator is concerned with the behavior of matter and energy. Those properties are under extreme conditions either very large or very small scale with the discrete, rather than continuous spectrum, which is the case of the classical harmonic oscillator. But, there are certain values that give the limitation of the energy of the oscillator.

Eq. (1) is also known as the energy eigenvalue equation. Solving it means to find $\phi(x)$ which is called the stationary states such that Eq. (1) is satisfy. These states i.e. the wavefunction is represented by a family of Hermite polynomials, Tannoudji et.al (1977). In this case, it is one-dimensional QHOS. Instead of finding solution mathematically, visualizing is another effective way to clearly understand QHOS. Thus, using C++ to simulate the system is really helpful. One can determine the graph of the energy eigenvalues, E_n and wavefunction, ϕ_n that will be generated by implementing them in the C++ programming language depending on the number of state, n entered by users. The simulation program initialize the equation of energy eigenvalues,

$$E_n = \left(\frac{1}{2} + n\right) \hbar\omega, \quad n = 0,1,2, \dots \quad (2)$$

and the wave function is given by,

$$\phi_n(x) = \left(\frac{\sqrt{\alpha}}{2^n n! \sqrt{\pi}}\right)^{\frac{1}{2}} H_n(\sqrt{\alpha}x) e^{-\frac{\alpha x^2}{2}}, \quad (3)$$

for which the natural units due to the physical constant such as, angular frequency ω and reduced Planck constant \hbar are parametrized by α . The term $H_n(\sqrt{\alpha}x)$ is the Hermite polynomials in one-variable parametrized by α .

In the framework of the program, the probability density of the solution to the time-independent Schrodinger equation which associated to the oscillator i.e. the normalized wavefunction is evaluated and the energy eigenvalues is given by an equally space energy values, $E_n = \left(\frac{1}{2} + n\right) \hbar\omega$, where $n = 0,1,2, \dots$

For the computational tools, C++ language have become a powerful programming language used in solving problems in area of physical science and engineering, Prinz & Prinz (2004). In this work, Dev C++ IDE software as the C++ development tools (download free from Orwell website) is used. The system (C++) requirement to obtain and display the exact solution is given by the following lists

- Dev C++ IDE - A free, well-designed and full-featured Integrated Development Environment (IDE) for C and C++ programming language, which is a File version: 5.11.0.0 by Bloodshed Software Company. It comes complete with compiler for creating software in C++.
- Graphics in Dev C++.rar - A 45.63 MB compressed archives files containing a few element that important to improve Dev C++. The significant files are graphics.h, 6-ConsoleAppGraphics.template, ConsoleApp_cpp_graph.txt, libbgi.a and winbgim.h.
- Graphics.h and winbgim.h file - The C header file from WinBGIm library. Both files are the compulsory files that must be include into compiler directory, C:\Program Files (x86)\Dev-Cpp\MinGW64\x86_64-w64-mingw32\include in order to compile and run the WinBGIm graphics library.
- libbgi.a - It need to be added into C:\Program Files (x86)\Dev-Cpp\MinGW64\x86_64-w64-mingw32\lib in order to use WinBGIm subdirectory of the Dev C++ directory.
- 6-ConsoleAppGraphics.template and ConsoleApp_cpp_graph.txt - Both files need to be added into directory template C:\Program Files (x86)\Dev-Cpp\Templates. ConsoleAppGraphics.template is the necessary thing to create a console application in Dev C++. Console Apps are usually designed without a graphical user interface (GUI) and compile into an individual executable file.
- Linkers - The linkers need to write in the Linker area on the Parameters tab whenever want to use #include<graphics.h> in a program, which are -lbgi, -lgdi32, -luser32, -lcomdlg32 -luuid, -loleaut32 and -lole32. The linkers are necessary in order to instruct the linker to link in definite libraries.

Results and Discussion

The current QHO program is designed by giving the freedom to the user to compute the desired number of states from the QHO. The console application which executes the task is shown below showing two options to produce the results. The first option is showing the number of desired up to 14, n states (Fig. 1) while the second option is showing the collective results of desired up to 5, n states (Fig. 4). Note that this can be increased to infinitely n terms.

From the simulation system, the visualization of the energy eigenvalues, E_n and wave function, ψ_n are produced according to the number of state entered by user. A console application is display below for the user to enter the number of state with option 1. Note that at the ground state, $n = 0$, the energy is not zero (see Fig. 2 (left)) as expected from Eq. (2). The other excited states are given as in Fig. 2 (right) and 3.

```

C:\Users\User\Desktop\FSC2017\QHOS.exe
Quantum harmonic oscillator (QHO) which is analogous to the
classical harmonic oscillator is well-known to have an exact
analytical solution from the time-independent Schrodinger equation
 $(\hbar^2/8m\pi^2)D^2\phi + \frac{1}{2}m\omega^2x^2\phi = E\phi$ 
where  $\omega$ = angular frequency and  $(\hbar^2/8m\pi^2)$ = reduced planck constant/2m.
The exact solution or so-called states are represented by the
well-known type of orthogonal polynomials called Hermite polynomials
and give rise to quantized energy levels with equally space values.
This program display the states and also the energy associated
to each states.
1. QHOS for specific number of state
2. Probability Density of QHOS
Choose the option: 1
The Number of State of QHO (0-14): 0
-----
Process exited after 24.06 seconds with return value 0
Press any key to continue . . .

```

Fig. 1 Console application to execute the task with option 1. User will need to choose the n number of state to get the expected E_n, ψ_n and $|\psi|^2$ for separate n states.

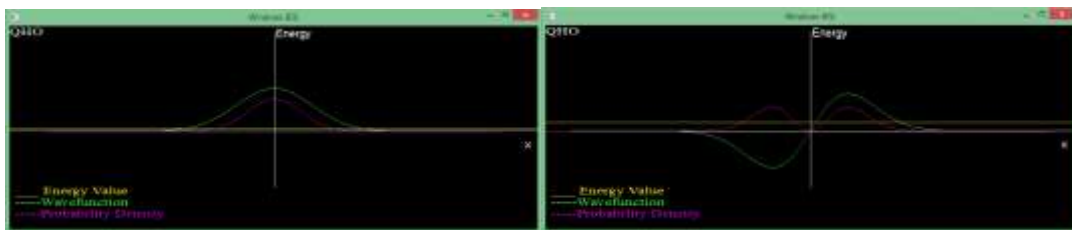


Fig. 2 Graph of the ground state i.e. $n = 0$ (left) and the first excited state $n = 1$ (right).

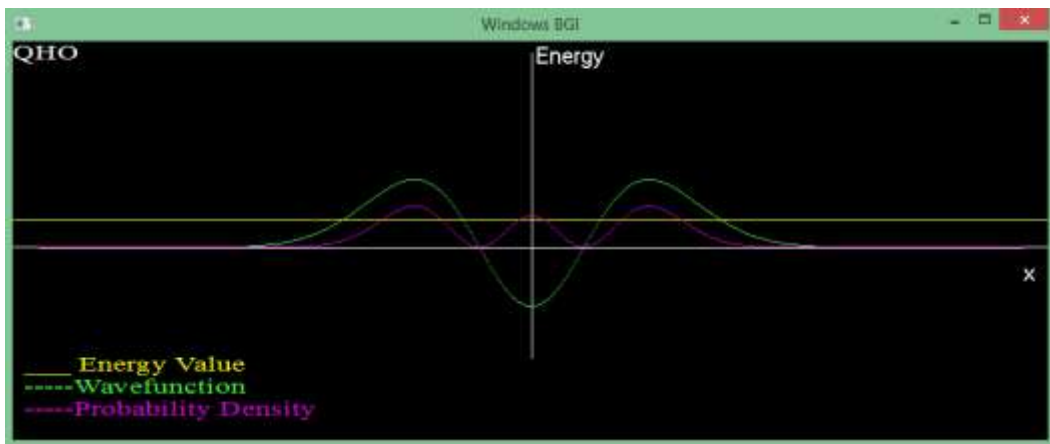


Fig. 3 Graph of the second excited state i.e. $n = 2$.

Note that, for the odd number of states (i.e. for $n = 1,3,5, \dots$) like the first excited state is an odd parity with first order polynomials multiplying Gaussian distribution given by the factor $e^{-\frac{\alpha x^2}{2}}$. Similarly one obtains even parity for states $n = 0,2,4, \dots$. The probability density of the particular states is given in Fig. 5 showing the simple harmonic motion but now the case is

discrete.

```
C:\Users\User\Desktop\FSC2017\QHOS.exe
Quantum harmonic oscillator (QHO) which is analogous to the
classical harmonic oscillator is well-known to have an exact
analytical solution from the time-independent Schrodinger equation

 $(\hbar^2/8m\pi^2)D^2\phi + \frac{1}{2}m\omega^2x^2\phi = E\phi$ 

where  $\omega$ = angular frequency and  $(\hbar^2/8m\pi^2)$ = reduced planck constant/2m.

The exact solution or so-called states are represented by the
well-known type of orthogonal polynomials called Hermite polynomials
and give rise to quantized energy levels with equally space values.
This program display the states and also the energy associated
to each states.

1. QHOS for specific number of state
2. Probability Density of QHOS

Choose the option: 2
The Number of State of QHO (0-5): 5

-----
Process exited after 80.54 seconds with return value 0
Press any key to continue . . .
```

Fig. 4 Console application to execute the task with option 2. User will need to choose the n number of state to get the expected $|\phi|^2$ for n states.

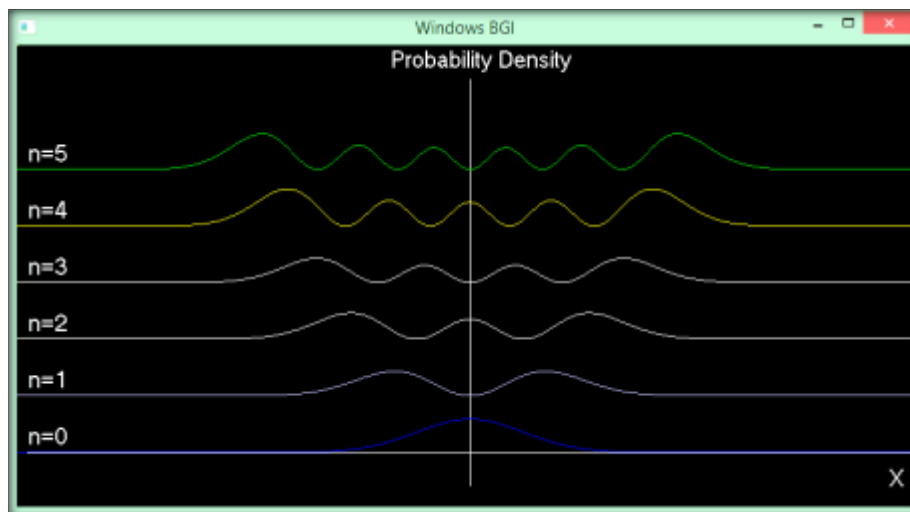


Fig. 5 Graph of the probability density up to $n = 5$ states.

Conclusion

With various computational methods available to study quantum mechanical systems, Dev C++ IDE software as the C++ development tools also provide useful features to clearly display the expected outcome from solving quantum harmonic oscillator. In standard quantum mechanics courses, dealing with QHO will involve the students to find exactly the energy eigenvalues E_n and the associated states, ϕ_n . From the program designed, it is shown that one could obtains from the associated number of n wavefunctions, its energy spectra and the probability density that is to find a particle represented by the wavefunction in some range.

Acknowledgement

Nurisya MS acknowledge support from Universiti Putra Malaysia, UPM, Putra Grant (GP-IPM/2016/ 9473100), Malaysia.

References

Barranco, A.V. (2016). Evolution of a quantum harmonic oscillator coupled to a minimal thermal environment, *Physica A* 459, 78.

Carreno, J.C.L and Laussy, F.P. (2016). Exciting with quantum light. I. Exciting and harmonic oscillator, *Phys. Rev. A* 94, 063825.

Daneshjo, N. (2011). Computer Modelling and Simulation, (OPTIROB 2011).

Griffiths, D.J. (2014). *Introduction to Quantum mechanics* (second edi). United State of America: Pearson Education Limited. pg. 41

Konstantinos N. A., (2016). Computational Physics: A Practical Introduction to Computational Physics and Scientific Computing (using C++), Creative Commons Attribution.

Kirch-Prinz, U., & Prinz, P. (2004). *A Complete Guide to Programming in C++*, 2nd Edi. Jones & Bartlett Pub.

Orwell DEV-C++ IDE (n.d.), <https://osdn.net/projects>. Retrieved Oct 2016.

Prado, M.A., Lopez Vazquez, P.C. and Gorin, T. (2017). Quantum kicked harmonic oscillator in contact with a heat bath, *Phys. Rev. A*. 95: 022118.

Schott, D. (2010). Modelling of oscillators : general framework and simulation projects, *12*(1), 17–23.

Tannoudji, C.C., Diu, B. and Laloe, F. (1977). *Quantum Mechanics*, Vol. 1, John Wiley and Sons. Pg 492

Zettili, N. (2009). *Quantum Mechanics and Applications*, John Wiley & Sons, Ltd.

2.2 First Passage Time Problem on Growing Geometrical Network

Nurul Nasha Amalina Shamsul Kamal, Chan Kar Tim, Nurisya Mohd Shah and Hishamuddin Zainuddin

Abstract

Networks are present in almost every aspect of our life. Hence, many complex network models have been proposed and constructed to explore the underlying structure of these real-world networks. Studying dynamical process on a network provides a good platform to characterize the network in terms of transport and search mechanism. The dynamical process can be described as random walks on the network since they have been used in the dynamics of many natural and artificial systems. In this paper, we investigate the properties of random walk such as mean first passage time (MFPT) on a growing geometrical network (GGN) constructed using hyperbolic tessellation of modular group. MFPT is an important characteristic of random walk as it serves as an important indicator measuring node importance and efficiency in trapping process. We derive an exact expression for the MFPT between two nodes using master equation of the system. We also report here the matrix formulation for the MFPT which are used for computing the values.

Keywords: Network, Random walk, Mean first passage time, Growing geometrical network

Introduction

Network is an important and powerful approach that can be used to study real world complex system such as biological (Zhou, Menche et al. 2014), social (Sinatra, Deville et al. 2015), etc. These networks are made up of nodes connected to each other via edges which may be directed or undirected. Studies on these network have reveal some common structural features such as power law degree distribution, small average path length and high clustering coefficient (Zhang, Rong et al. 2006). Two most studied classes of complex networks that focus on these properties are the scale free network and small world network (Zhang, Rong et al. 2006).

Networks that describe real-world systems are usually very large and complex. Hence, many new network models are proposed by researchers to mimic the real complex systems in order to gain a better understanding on the topology and dynamics of the networks. A way to understand the propagation of dynamical quantities in network is to use random walk (RW) as a fundamental dynamic process (Wijesundera, Halgamuge et al.). RW is suitable in this context because many natural and artificial systems such as natural disasters (Wijesundera, Halgamuge et al.), stochastic behavior of molecules, stock prices, routing in information packets in Internet and so on, are well described as random walks on a network (Perkins, Foxall et al. 2014). One main quantity of RW that has been studied extensively is the mean first passage time (MFPT) (Wijesundera, Halgamuge et al. , Hughes 1995, Redner 2001). It is the expected time for a walker to hit a specified target for the first time starting from a source point. This property of RW has been widely studied in different networks for example fractals (Lin, Wu et al. 2010), lattices (Condamin, Bénichou et al. 2007) and scale free networks (Gallos 2004, Noh and Rieger 2004, Zhang, Julaiti et al. 2011).

The aim of this paper is to derive a general solution for MFPT on a particular growing geometrical network (GGN) constructed from tessellation using the modular group. We

follow closely the method based on generating function or Laplace transform that has been described by Hughes (1995) and Noh and Rieger (2004). Using the same property, we determine the characteristic relaxation time and also a random walk measure (Noh and Rieger 2004) that serves as an important indicator for node importance and efficiency in trapping process. We also report here the matrix formulation for the MFPT which are used for computing the values.

Growing Geometrical Network (GGN)

Growing geometrical network is constructed using hyperbolic tessellation of modular group where the details of the construction can be found in Taha et. al. (2016). This network, $G(N, E)$, is an undirected network with truncated power law degree distribution with N nodes and E edges, depending on the level of growth of the network. The level of growth is controlled by the number of generators produced based on the recursive nature of the programme. The topology of G can be represented by its adjacency matrix \mathbf{A} whose elements $A_{ij} = 1(0)$ if node i and j are (not) connected by an edge. Since the network is undirected, elements $A_{ij} = A_{ji}$. As for the degree of node i , it is given by $K_i = \sum_j A_{ij}$.

Random Walks on Network

Random walk in network is a Markov process because each step is basically independent of all previous steps (Wijesundera, Halgamuge et al.). Since the walker cannot stay at the same node, it will jump from one node to another at each time step with equal probability, $1/K_i$. The occupation probability for a walker at node v at time step t is denoted as $P(v, t)$. When $t=0$, the initial condition is given as $P(v, 0) = \delta_{v_0} \delta_{t,0}$ where v_0 is the initial location of the walker. This stochastic process in discrete time can be described by a master equation (Noh and Rieger 2004) with the help of transition probability for the walker defined as $W_{ij} = A_{ij} / K_i$. Considering the walker starts at node i at $t=0$ and reaches node j at time t ; the master equation can be expressed as

$$P_{ij}(t+1) = \sum_k \frac{A_{kj}}{K_k} P_{ik}(t). \quad (1)$$

Since GGN has a reflecting boundary condition, the random walker can move in any direction but cannot leave the system (Lau and Szeto 2010). This situation is similar to the diffusion process except that all walkers must follow the master equation at every time step. To find the walker probability at j from i at t time steps, we consider the asymptotic behavior of the transition probability. Taking the infinite time limit, $t \rightarrow \infty$, based on the principle of detailed balance, the system reaches an equilibrium state where there is no net flow of random walkers in any direction. Hence, $K_i P_j^\infty = K_j P_i^\infty$ where $P_j^\infty = \lim_{t \rightarrow \infty} P_{ij}(t)$. At this point, the equilibrium state probability can be described as

$$P_j^\infty = \frac{K_j}{2L}, \quad (2)$$

where L is the number of edges (Noh and Rieger 2004, Noh 2007). Eq.(2) shows that at

equilibrium, the walker has a higher tendency to move to nodes with more edges. However, if the net flow is not zero (e.g. t is not large enough), the system consists of equilibrium state probability as well as fluctuation around it. We should take note that the total walker probability is a conserved quantity, $\sum_{v \in V} P(v, t) = 1$.

First Passage Time Problem

The dynamical aspect of the random walker is studied using the first passage time (FPT) feature. The FPT is defined as the time required for a random walker to first reach a predefined target state or set of states (Wijesundera, Halgamuge et al.) and is measured as a distribution rather than for a particular path. For a given source node i to a target node j , the FPT distribution is given as $F_{ij}(t)$ while the total FPT probability is $\sum_t F_{ij}(t) = 1$. When $t = 0$, $F_{ij}(t = 0) = 0$. Using the FPT distribution, mean first passage time is given as $\langle T_{ij} \rangle = \sum_t t F_{ij}(t)$. According to Lau and Szeto (2010), this method can be used to compute the MFPT but it is more difficult than using the already available walker probability distribution.

To find the MFPT using the walker probability distribution, we first need to find a relation between $F_{ij}(t)$ and $P_{ij}(t)$. This relation is basically shown in Figure 1 where a walker moves from node i and reaches j at time t . The walker might reach the destination earlier at time t' , but since the time step is set as t , the walker continues to move and then returns to j after $t - t'$ additional steps. It is known that for infinite lattice random walk, for dimension $d \leq 2$, a random walk is recurrent means the walker will return to the destination point but it might take an infinitely long time (Redner 2001).

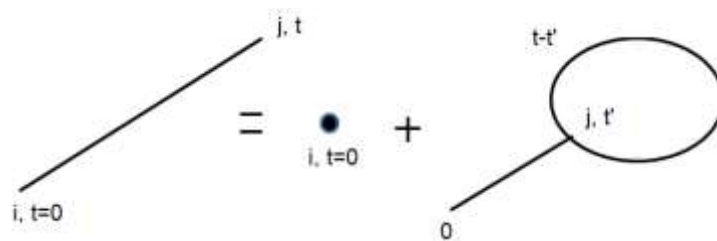


Figure 1: Relation between the occupation probability of a random walk moving from i to j in t -steps. The first passage probability is represented by the straight line while the circle represents the recurrence probability (Redner 2001).

From Figure 1, we form a convolution equation given as

$$P_{ij}(t) = \delta_{ij} \delta_{t0} + \sum_{t'=0}^t F_{ij}(t') P_{jj}(t-t'), \quad (3)$$

where $\delta_{ij} \delta_{t0}$ represents the initial condition of the walker probability. According to Redner (2001) and Hughes (1995), this convolution equation can be decoupled by using Laplace transform and the result is

$$P_{ij}(s) = \delta_{ij} + F_{ij}(s) P_{jj}(s), \quad (4)$$

where the fundamental connection is

$$F_{ij}(s) = \begin{cases} \frac{P_{ij}(s)}{P_{ij}(s)}, & i \neq j \\ 1 - \frac{1}{P_{ij}(s)}, & i = j \end{cases}. \quad (5)$$

Expressing the terms in Eq. (4) with Laplace transform, we have

$$F_{ij}(s) = \sum_{t=0}^{\infty} e^{-st} F_{ij}(t); \quad (6)$$

$$P_{ij}(s) = \sum_{t=0}^{\infty} e^{-st} P_{ij}(t). \quad (7)$$

MFPT can be obtained by differentiating Eq. (5) with respect to s and then set $s = 0$:

$$\langle T_{ij}^r \rangle = (-1)^r \left. \frac{d^r}{ds^r} F_{ij}(s) \right|_{s=0}. \quad (8)$$

Since in equilibrium state of the system is not just the system staying at the maximum values, but it includes the fluctuation around the mean. Hence, the Laplace transform for Eq. (7) can be written as

$$P_{ij}(s) = \sum_{t=0}^{\infty} e^{(-st)} P_j^{\infty} + \sum_{t=0}^{\infty} e^{(-st)} [P_{ij}(t) - P_j^{\infty}]. \quad (9)$$

This equation represents the occupation probability with the effect of fluctuation during the transition. To solve Eq. (9), we simplify the first term as $\sum_{t=0}^{\infty} e^{(-st)} = 1/(1 - e^{(-s)})$, and use the

Taylor series expansion $e^{(-st)} = \sum_{n=0}^{\infty} (-1)^n t^n \frac{s^n}{n!}$ for the second term. We define

$R_{ij}^{(n)} \equiv \sum_{t=0}^{\infty} t^n [P_{ij}(t) - P_j^{\infty}]$ and set $P_j^{\infty} = K_j / 2L$, thus Eq. (9) can be rewritten as

$$P_{ij}(s) = \frac{K_j}{2L(1 - e^{(-s)})} + \sum_{n=0}^{\infty} (-1)^n \frac{s^n}{n!} R_{ij}^{(n)}. \quad (10)$$

If the walker returns to the origin $i = j$, then Eq. (10) is written as

$$P_{jj}(s) = \frac{K_j}{2L(1 - e^{(-s)})} + \sum_{n=0}^{\infty} (-1)^n \frac{s^n}{n!} R_{jj}^{(n)}. \quad (11)$$

The summation converges because all moment $R_{ij}^{(n)}$ is finite due to exponential decay of

$P_{ij}(t) - P_j^\infty$ (Noh and Rieger 2004, Lau and Szeto 2010). Substituting Eq. (10) and (11) in Eq. (5) with $i \neq j$ yields

$$F_{ij}(s) = \frac{\frac{K_j}{2L(1-e^{-s})} + R_{ij}^{(0)}}{\frac{K_j}{2L(1-e^{-s})} + R_{jj}^{(0)}} ; \quad (12)$$

$$= \frac{K_j + R_{ij}^{(0)} 2L(1-e^{-s})}{K_j + R_{jj}^{(0)} 2L(1-e^{-s})}$$

while for $i = j$, it becomes

$$F_{jj}(s) = 1 - \frac{1}{\frac{K_j}{2L(1-e^{-s})} + R_{jj}^{(0)}} . \quad (13)$$

$$= \frac{K_j + R_{jj}^{(0)} 2L(1-e^{-s}) - (2L(1-e^{-s}))}{K_j + R_{jj}^{(0)} 2L(1-e^{-s})}$$

Using Eq. (8), MFPT for Eq. (12) is

$$\langle T_{ij} \rangle = - \frac{d}{ds} F_{ij}(s) \Big|_{s=0}$$

$$= \frac{R_{jj}^{(0)} 2Le^{-0} (R_{ij}^{(0)} 2L - R_{ij}^{(0)} 2Le^{-0} + K_j)}{(R_{jj}^{(0)} 2L - R_{jj}^{(0)} 2Le^{-0} + K_j)^2} - \frac{R_{ij}^{(0)} 2Le^{-0}}{(R_{jj}^{(0)} 2L - R_{jj}^{(0)} 2Le^{-0} + K_j)} , \quad (14)$$

$$= \frac{R_{jj}^{(0)} 2L}{K_j} - \frac{R_{ij}^{(0)} 2L}{K_j} = \frac{2L}{K_j} [R_{jj}^{(0)} - R_{ij}^{(0)}]$$

and for Eq. (13) is

$$\langle T_{jj} \rangle = - \frac{d}{ds} F_{jj}(s) \Big|_{s=0}$$

$$= \frac{R_{jj}^{(0)} 2Le^{-0} (K_j + R_{jj}^{(0)} 2L - 2L - R_{jj}^{(0)} 2L - 2Le^{-0})}{(R_{jj}^{(0)} 2L - R_{jj}^{(0)} 2L + K_j)^2} + \frac{2L - R_{jj}^{(0)} 2L}{(R_{jj}^{(0)} 2L - R_{jj}^{(0)} 2L + K_j)} . \quad (15)$$

$$= \frac{R_{jj}^{(0)} 2L}{K_j} - \frac{R_{jj}^{(0)} 2L}{K_j} + \frac{2L}{K_j} = \frac{2L}{K_j}$$

Besides the mean first passage time, another transport property of random walk can be identified here, which is the characteristic relaxation time given as

$$\tau_j = R_{jj}^{(n)} \equiv \sum_{t=0}^{\infty} [P_{jj}(t) - P_j^{\infty}]. \quad (16)$$

The relaxation time is basically the asymptotic time of convergence to the equilibrium or stationary distribution. It is also related to the second largest eigenvalue of the time evolution operator (Lau and Szeto 2010).

When $i \neq j$, the random walk motions are asymmetric. The difference between $\langle T_{ij} \rangle$ and $\langle T_{ji} \rangle$ is given as

$$\begin{aligned} \langle T_{ij} \rangle - \langle T_{ji} \rangle &= \frac{2L}{K_j} [R_{jj}^{(0)} - R_{ij}^{(0)}] - \frac{2L}{K_i} [R_{jj}^{(0)} - R_{ji}^{(0)}] \\ &= 2L \left[\frac{R_{jj}^{(0)}}{K_j} - \frac{R_{ii}^{(0)}}{K_i} \right] - 2L \left[\frac{R_{ij}^{(0)}}{K_j} - \frac{R_{ji}^{(0)}}{K_i} \right]. \end{aligned} \quad (17)$$

The last term vanishes because of the equilibrium state while the first term can be written in terms of its characteristic relaxation time and equilibrium probability given as

$$\langle T_{ij} \rangle - \langle T_{ji} \rangle = \frac{1}{C_j} + \frac{1}{C_i} \quad (18)$$

This new measurement $C_j \equiv \frac{P_j^{\infty}}{\tau_j}$ is called the random walk centrality (RWC) (Noh and Rieger 2004). It measures how fast a random walker can travel from a node to another node. When a node has larger RWC value, this means that the walker will visit it earlier. In terms of communication, a node with larger RWC will receive signal emitted by its partner earlier (Noh and Rieger 2004).

Matrix Formulation For MFPT

In order to compute the value for MFPT, we need to form the matrix formulation for equation $R_{ij}^{(n)} \equiv \sum_{t=0}^{\infty} [P_{ij}(t) - P_j^{\infty}]$. Setting $\mathbf{R}^{(0)}$ as the matrix with element $R_{ij}^{(0)}$, the equation can be rewritten as

$$\mathbf{R}^{(0)} = \sum_{t=0}^{\infty} (\mathbf{W}^t - \mathbf{Q}). \quad (19)$$

Matrix \mathbf{W} represents the transition matrix while $\mathbf{Q} \equiv \mathbf{P}^{\infty} \mathbf{1}$ represent the equilibrium probability matrix. $\mathbf{P}^{\infty} = (P_1^{\infty}, P_2^{\infty}, \dots, P_N^{\infty})$ is a column vector while $\mathbf{1} = (1, \dots, 1)$ is a row vector. Since matrix \mathbf{Q} is the projection of \mathbf{W} onto the subspace with eigenvalue 1, this yield the relations $\mathbf{Q}^n = \mathbf{Q}$ for $n > 0$ and $\mathbf{WQ} = \mathbf{QW} = \mathbf{Q}$ (Noh 2007). From these relations, $\mathbf{W}^n - \mathbf{Q}$ is equal to $(\mathbf{W} - \mathbf{Q})^n$ for $n > 0$ and $(\mathbf{I} - \mathbf{Q})$ for $n = 0$ (Noh 2007). Using all these relations,

Eq.(19) can be redefined as

$$\begin{aligned}
\mathbf{R}^{(0)} &= (\mathbf{W}^0 - \mathbf{Q}) + \sum_{t=1}^{\infty} (\mathbf{W}^t - \mathbf{Q}) \\
&= (\mathbf{I} - \mathbf{Q}) + \frac{-\mathbf{Q} + \mathbf{W}}{\mathbf{I} + \mathbf{Q} - \mathbf{W}} \\
&= \frac{1}{\mathbf{I} + \mathbf{Q} - \mathbf{W}} - \mathbf{Q}
\end{aligned} \tag{20}$$

Conclusion

We have derived an expression for the mean first passage time of a random walk process on a growing geometrical network by using Laplace transform on the convolution relation between the first passage time and the occupation probability. Besides MFPT, we also managed to determine the characteristic relaxation time of the system as well as a random walk measure for node importance and efficiency in the network. Future work on this research will be concentrated on computing the MFPT, RWC and relaxation time for various geometrical networks with different levels of growth.

Acknowledgement

The authors wish to acknowledge the financial support provided through the Fundamental Research Grant Scheme (FRGS), Project No. 01-01-16-1865FR by Ministry of Higher Education.

References

- Condamin, S., et al. (2007). "Random walks and Brownian motion: A method of computation for first-passage times and related quantities in confined geometries." Physical Review E **75**(2): 021111.
- Gallos, L. K. (2004). "Random walk and trapping processes on scale-free networks." Physical Review E **70**(4): 046116.
- Hughes, B. D. (1995). Random Walks and Random Environments: Random walks, Clarendon Press.
- Lau, H. W. and K. Y. Szeto (2010). "Asymptotic analysis of first passage time in complex networks." EPL (Europhysics Letters) **90**(4): 40005.
- Lin, Y., et al. (2010). "Determining mean first-passage time on a class of treelike regular fractals." Physical Review E **82**(3): 031140.
- Noh, J. D. (2007). "Interacting particle systems in complex networks." arXiv:cond-mat/0701401.

Noh, J. D. and H. Rieger (2004). "Random Walks on Complex Networks." Physical Review Letters **92**(11): 118701.

Perkins, T. J., et al. (2014). "A scaling law for random walks on networks." **5**: 5121.

Redner, S. (2001). A Guide to First-Passage Processes. Cambridge, Cambridge University Press.

Sinatra, R., et al. (2015). "A century of physics." Nat Phys **11**(10): 791-796.

Taha, M. H. M., et al. (2016). "Construction of Network Based on Modular Group." J. Solid St. Sci. Tech. Lett. **17**: 93.

Wijesundera, I., et al. Natural Disasters, When Will They Reach Me? Springer Natural Hazards,: 1 online resource (XVIII, 128 p. 146 illus., 137 illus. in color.).

Zhang, Z., et al. (2011). "Mean first-passage time for random walks on undirected networks." The European Physical Journal B **84**(4): 691-697.

Zhang, Z., et al. (2006). "Evolving Apollonian networks with small-world scale-free topologies." Physical Review E **74**(4): 046105.

Zhou, X., et al. (2014). "Human symptoms–disease network." **5**: 4212.

CHAPTER 3

MAGNETIC MATERIALS AND APPLICATIONS

3.1 Structure, Magnetic and Magneto-transport Properties of La-Sr-Mn-O/NiO Composite

Lim Kean Pah, Abdul Halim Shaari, Jumiah Hassan, Chen Soo Kien, Mohd Mustafa Arwang Kechik, Ng Siau Wei and Tan Chew Ling

Abstract

Colossal Magnetoresistance (CMR) is widely used in sensor industry and the enhancement of MR value at low field is very important. Many works have been done in order to improve Low Field Magnetoresistance (LFMR). One of the methods is introduce artificial layer by adding oxide. So in this work, NiO was added to form composite compound to study the extrinsic magnetoresistance effects. Polycrystalline nano-size La-Sr-Mn-O powder was prepared via sol-gel method. The structure, magnetic and magnetotransport properties of La-Sr-Mn-O/NiO composite has been investigated by using X-Ray Diffraction (XRD) method, Vibrating Sample Magnetometer (VSM), and Hall Measurement System. There are three phases in the composite, which is LSMO perovskite phase, NiO cubic phase, and NiO₂ hexagonal phase. The XRD results shows that there is no reaction is observed between LSMO, NiO, and NiO₂ and the metal oxide added do not change the structure of LSMO. Addition of NiO/NiO₂ as the secondary phase weakened the ferromagnetic behaviour, shifted the metal-insulator transition (T_{MI}) from 264K to 192K, and enhanced the Low Field Magnetoresistance (LFMR) effect.

Keywords : Magnetoresistance, composite, structure, manganites

Introduction

Since the discovery of colossal magnetoresistance (CMR) in doped perovskite manganites, much effort has been expended to find the significant low field magnetoresistance (LFMR) due to its applicable in magnetic devices [1-3]. There are two type of CMR, firstly, the intrinsic MR effects originates from the double exchange (DE) mechanism proposed by Zener in 1951, which to explain the CMR phenomena observed near the Curie temperature (T_C) [4]. Secondly, the extrinsic MR, which is highly sensitive to a low applied external magnetic field so called low field magnetoresistance (LFMR) [5]. LFMR effect is largely dependent on the grain boundary properties and is generally ascribed to the spin polarized intergrain tunneling of conduction electrons. The tunnelling process takes place across the grain boundary (due to the magnetic disorder or the dilution of manganites with secondary phase), hence the magnetic homogeneity near the grain boundary area will alter the barrier layer and affect the spin tunnelling process [6]. In recent year, much efforts has been done to improved the LFMR effect by forming composites manganites with various type of secondary oxide phases such as magnetic material [7], polymer material [8], oxide [9], insulator [10] and other manganite [11]. The efficiency of insulator barriers in these composite manganites system is very important for the enhancement of LFMR. Therefore, efforts to control the parameter and the scale of insulator barrier would be worth considering to enhance the LFMR. Nasri et al. reported that by increasing CuO content, the value of CMR increases as compared to that of the pure La_{0.6}Ca_{0.4}MnO₃ sample and the intrinsic MR (related to grain) gets enhanced from 16 % for pure LCMO to 30 % for the 18 % CuO added sample [12]. Kim

and Yoo reported that maximum LFMR value of 2.22% at 300 K in 500 Oe could be achieved from the composite sample with addition of 10 mol% La_2O_3 in $\text{La}_{0.7}\text{Sr}_{0.3}\text{MnO}_3$ [13].

Composites manganites prepared under high temperature leads to a problem on the interfacial phase. The atomic inter-diffusion and chemical reaction near grain boundary modifies the local magnetic structure that affects the spin dependent scattering across the grain boundaries or intergrain spin polarized tunnelling of the conduction electron, which is believed to be important for extrinsic LFMR. However, this undesirable effects and high temperature synthesis could be avoided by using nano-size secondary phases. In fact, the nano-structure insulator material would enhance the efficiency of insulator barriers at the grain boundary region than usual micron sized secondary phases [14-15]. Therefore, in the present study we report the structure, electrical and magneto-transport properties of $\text{La}_{0.7}\text{Sr}_{0.3}\text{MnO}_3$:nano-NiO composites.

Materials and Methods

Polycrystalline samples of $\text{La}_{0.67}\text{Sr}_{0.33}\text{MnO}_3$ (LSMO) were synthesized via sol-gel method. The high purity starting powder of $\text{La}(\text{NO}_3)_3 \cdot 6\text{H}_2\text{O}$, $\text{Sr}(\text{NO}_3)_2$ and $\text{Mn}(\text{NO}_3)_2 \cdot 4\text{H}_2\text{O}$ were diluted with distilled water and mixed together. Next, citric acid was dissolved in distilled water and adds to the nitrates solution by titration method. Then, ethylene glycol was added and the solution was continuously stirred at 60 °C in order to achieve evaporation of excess water and accelerate the polyesterification reaction until yellowish viscous gels were form. To eliminate the organic elements, the gel was further heated and dried at 130 °C for 24 hours to complete the polyesterification reaction to obtain dark brown porous foam. The homogeneous powder was ground and calcined at 500 °C for 5 hours and then reground before pre-sintered at 800 °C for 6 hours. The obtained powder of LSMO was well mixed with 5 % of NiO powder (20 - 50 nm) in ratio of $0.95(\text{La}_{0.67}\text{Sr}_{0.33}\text{MnO}_3) / 0.05(\text{NiO})$ and pressed into 13 mm pellet and then sinter at 800 °C for 2 hours. The structural of the samples were characterized by X-ray diffraction (XRD, Phillips PW 3040/60 Xpert Pro) using a $\text{CuK}\alpha$ radiation at room temperature. The temperature dependence of the resistivity using 4 point probe method as a function of temperature (80 – 300 K) were carried out by Lake Shore 7604 Hall Effect measurement system with applying the magnetic fields (0 – 1 Tesla).

Results and Discussion

Figure 1 shows the XRD spectrum for pure LSMO and 5% added LSMO sample. All the XRD raw data were matched with the ICSD standard, then analysed and refined by using Rietveld method in X'pert Highscore Plus software. As shown in Figure 1, three phases were observed in the composite, which is LSMO phase (hexagonal), NiO phase (cubic), and NiO_2 phase (hexagonal) as 5 % of NiO was added to LSMO. From the XRD results, the peaks correspond to LSMO phase do not shift indicated that there is no reaction between LSMO and NiO. NiO and NiO_2 were formed as second and third phase in the composite and mainly segregate at the boundaries and/or the surfaces of the LSMO grain. The refinement results were tabulated in Table 1. LSMO (ICSD collection code: 50717) is hexagonal structure with the space group of $R\bar{3}c$ (167), while for NiO (ICSD collection code: 9866) is cubic structure with the space group of $Fm\bar{3}m$ (225), and for NiO_2 (ICSD collection code: 78698) is hexagonal structure with the space group of $R\bar{3}m$ (166) respectively. The refinement results also show that the Mn-O-Mn bond angle and the Mn-O bond length are almost the same. This further proved that the NiO and NiO_2 did not react with LSMO or diffuse inside LSMO structure and stay as the composite state.

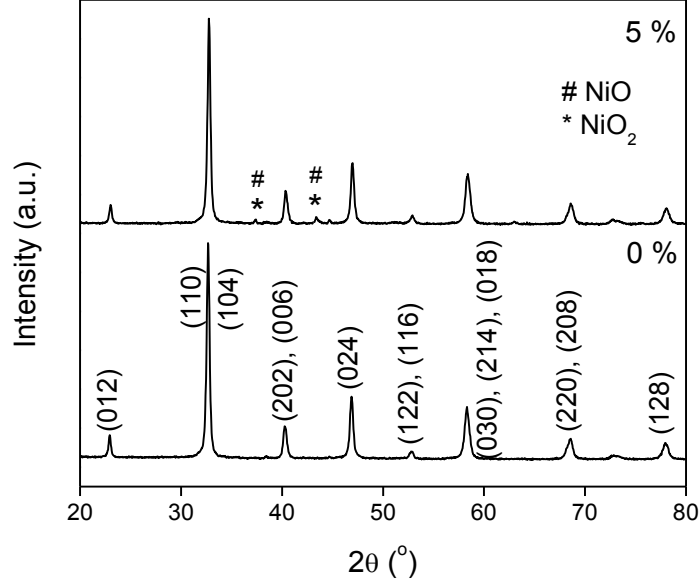


Figure 1: XRD pattern for $(1-x)(\text{La}_{0.67}\text{Sr}_{0.33}\text{MnO}_3)/x(\text{NiO})$ where “#” refer as the reflection peaks of NiO and “*” refer as NiO_2 .

Table 1: Refinement results of $\text{La}_{0.67}\text{Sr}_{0.33}\text{MnO}_3/\text{NiO}$ composite

Sample code	LSMO	
Structure type	Hexagonal	
Space group	R-3c (167)	
Composition NiO	0 %	5 %
$a/\text{Å}$	5.487520	5.48858
$b/\text{Å}$	5.487520	5.48858
$c/\text{Å}$	13.379370	13.382
Volume/ Å^3	348.914	349.118
$\angle \text{Mn-O-Mn}$ ($^\circ$)	166.494	166.494
Mn-O(Å)	1.951	1.951
Crystallite size (nm)	34.4	33.3
R_P (%)	4.1437	4.21897
R_{WP} (%)	5.31852	5.65249
R_{EXP} (%)	3.9357	3.7711
Goodness of fit	1.82615	2.24669

Figure 2 shows the graph of magnetization versus applied magnetic fields for both samples. In early studied, the Curie temperature (T_c) of LSMO is around 364 K, which is above room temperature [13]. Hence, LSMO sample was expected to behave in soft ferromagnetic state at room temperature. The hysteresis M-H graph shows a typical sigmoid curve with a very small coercivity value indicates that LSMO is a typical soft ferromagnetic material. The magnetization of LSMO/NiO increased rapidly at low fields and appeared saturated at higher field. The magnetization of the samples is decreased from 41.924 emu/g for pure LSMO to 35.037 emu/g as 5 % of composite nickel oxide was added. LSMO is known as ferromagnetic

material in the room temperature, however, NiO was observed as an antiferromagnetic [16]. Hence, the magnetization of composite sample is decreased due to the antiferromagnetic behaviour of NiO in room temperature.

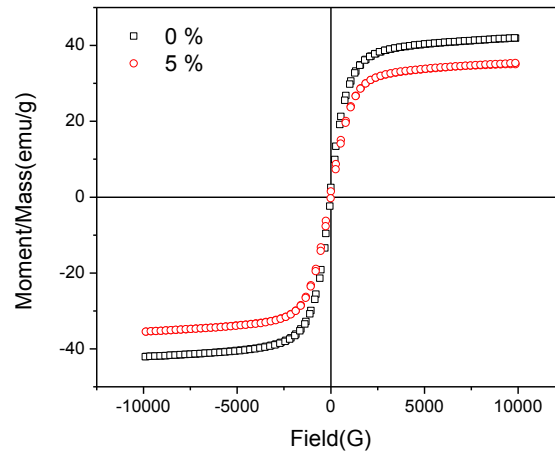


Figure 2: Moment/mass versus magnetic field for $\text{La}_{0.67}\text{Sr}_{0.33}\text{MnO}_3/\text{NiO}$ composite

Figure 3 present the temperature dependence of resistivity measured in the temperature range of 80 – 300 K for both samples. It can be found that as the temperature increased from 80 K to 300 K, the resistivity increased to a maximum point and dropped again. The maximum point of resistivity, T_{MI} is known as the metal-insulator transition temperature. When the NiO concentration increased from 0 % to 5 %, the metal-insulator transition shifted to the lower temperature which is from 264 K to 192 K. For below the T_{MI} , the electrical transport is mainly due to the double exchange (DE) mechanism. From the M-H results (Figure 2), the ferromagnetic property of LSMO was weakened due to addition of NiO. Hence, DE had been suppressed and shifted the T_{MI} to lower value. Secondly, when the temperature decreased, the phonon effect is weak, and leads to the enhancement of double exchange mechanism, and hence the resistivity decreased. For above the T_{MI} , the electrical transport is mainly caused by the Jahn-Teller (JT) effect. As the temperature increased, the phonon effect increased. This enhanced the JT effect and hence the resistivity decreased.

Figure 4 showed the resistivity versus temperature for $\text{La}_{0.67}\text{Sr}_{0.33}\text{MnO}_3/\text{NiO}$ composite of 0 % and 5 % NiO at 0 T, 0.5 T and 1.0 T. Figure 4 showed that when the 0.5 tesla and 1.0 tesla magnetic field were applied, the resistivity dropped. In the presence of the magnetic field, the alignment of localised t_{2g} spin in the 3d (Mn) orbital is more aligned, and thus the double exchange mechanism is enhanced. The resistivity dropped in the presence of 0.5 T magnetic field is more significant than in 1.0 T magnetic field prove that the enhancement in magnetoresistance (MR) is observed at low field which is known as low field magnetoresistance (LFMR). The small field enable to align both t_{2g} spin at the 3d (Mn) orbital and spin alignment of antiferromagnetic NiO layer, so the electron easy to hop and tunnelling through. This enhancement of LFMR is due to the grain boundary effect where small field is enough to fully align the grain boundary layer. (NiO and NiO_2). Therefore, at high field, no significant extrinsic effect will be contributed, only intrinsic effect is contribute to the MR value. Therefore, small increment of MR value is observed.

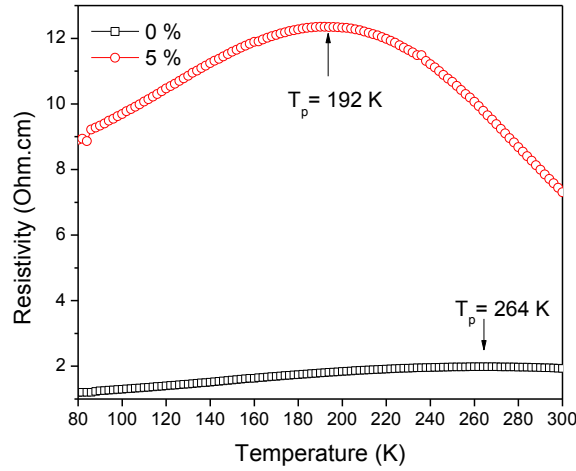


Figure 3: Resistivity versus temperature for $\text{La}_{0.67}\text{Sr}_{0.33}\text{MnO}_3/\text{NiO}$ composite at 0 T

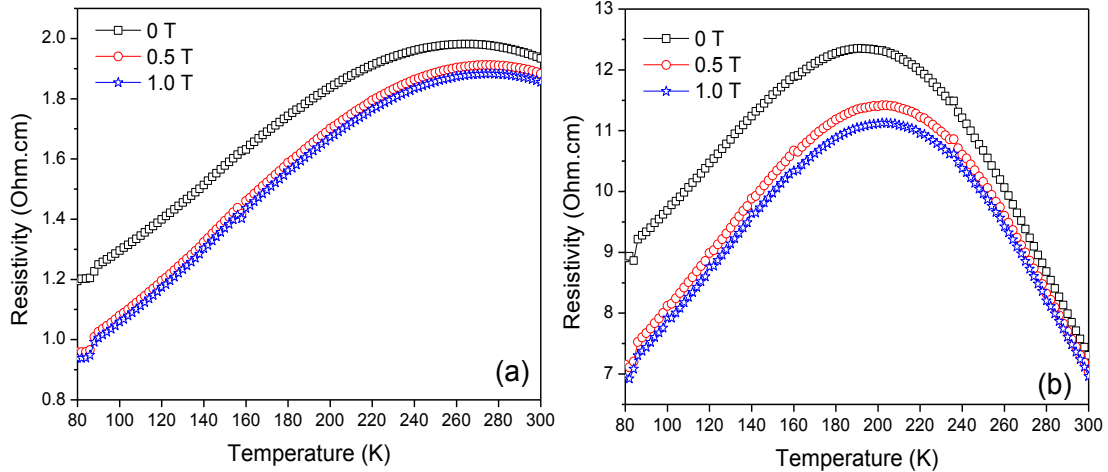


Figure 4: Resistivity versus temperature for $\text{La}_{0.67}\text{Sr}_{0.33}\text{MnO}_3/\text{NiO}$ composite of (a) 0 % and (b) 5 % of NiO at 0 T, 0.5 T and 1.0 T

Figure 6 show the magnetoresistance versus applied magnetic field for $\text{La}_{0.67}\text{Sr}_{0.33}\text{MnO}_3/\text{NiO}$ composite. A sharp increment in MR was observed at low fields (0 T – 0.1 T) and followed by a slow increment in the higher field (0.2 T – 1.0 T). This is the typical behavior of extrinsic MR. When the magnetic field is applied, the t_{2g} spin at 3d (Mn) orbital and also the antiferromagnetically align NiO/NiO₂ layer is more aligned, so the MR value increased. The alignment of spin in the parallel configuration leads to the decrease of resistivity and enhancement in low field magnetoresistance (LFMR). The enhanced MR effect at low temperature is due to the formation of composites which is the additional grain boundary effects introduced by the NiO. For the slow changes of MR at high field is mainly due to the intrinsic effect, which mainly caused by the bulk properties of LSMO phase, is known as high field magnetoresistance (HFMR). The graphs also show that the MR of the composite had not yet reach saturation when 1.0 T magnetic field was applied. Hence, higher magnetic field is required to fully align the 3d spin of (Mn) orbital.

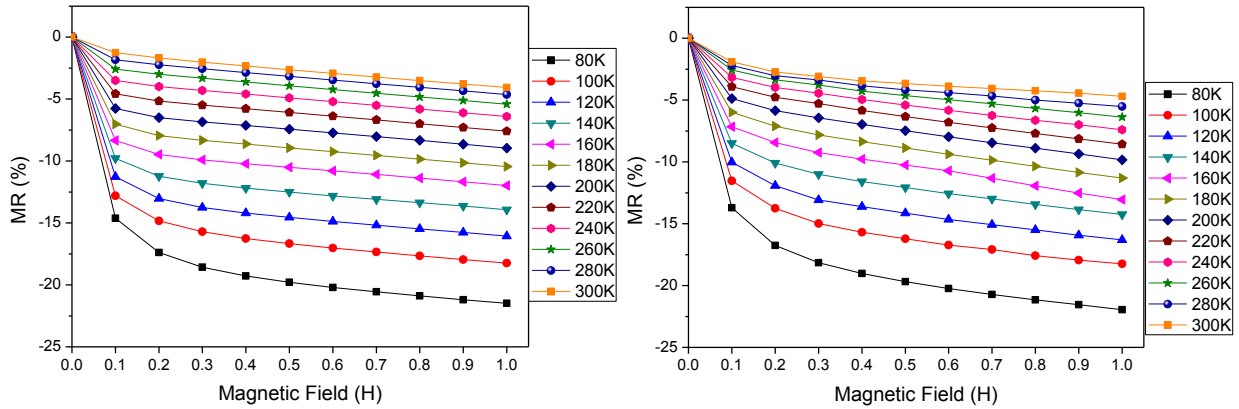


Figure 6: % MR versus magnetic field for $\text{La}_{0.67}\text{Sr}_{0.33}\text{MnO}_3/\text{NiO}$ composite of (a) 0 % NiO & (b) 5 % NiO

Figure 8 shows the magnetoresistance versus temperature for $\text{La}_{0.67}\text{Sr}_{0.33}\text{MnO}_3/\text{NiO}$ composite at 1.0 Tesla for both samples. Typical behavior of extrinsic magnetoresistance effect was observed due to the grain boundary effect. When the temperature decreased, phonon effect is less. All spin (e_g and t_{2g} spin of Mn) is easy to hop. As magnetic field is applied, localize t_{2g} spin is easy to align and hence DE is enhanced. This give rise to higher MR value at low temperature.

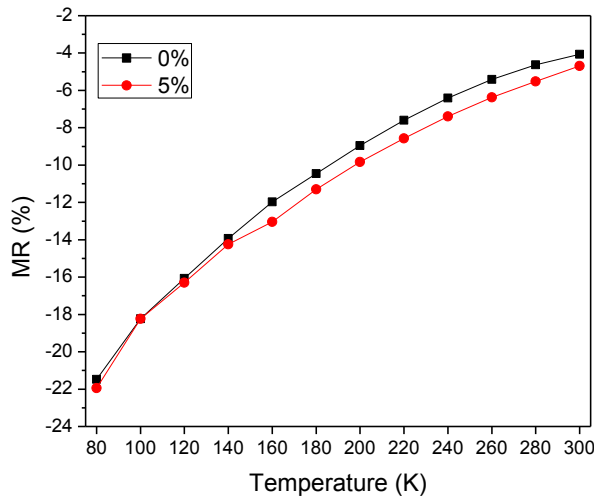


Figure 8: % MR versus temperature for $\text{La}_{0.67}\text{Sr}_{0.33}\text{MnO}_3/\text{NiO}$ composite at 1.0 T

Conclusion

As conclusion, homogeneous and fine La-Sr-Mn-O sample were prepared by using sol-gel method. Five different compositions of Nickel Oxide (NiO) nanoparticle, which is 0 %, 5 %, 10 %, 15 %, and 20 % were added into five LSMO samples respectively. The XRD spectrum shows that there are three phases in the composite, which is LSMO phase (hexagonal), NiO phase (cubic), and NiO_2 phase (hexagonal). No reaction is observed between LSMO, NiO, and NiO_2 which can be proved by the unchanged angle of Mn-O-Mn and the Mn-O bond distance.

The density of composite compound increased when the NiO concentration increased from 0 % to 10 %, and the density decreased for 15 % and 20 % of NiO concentration. The graph magnetization versus applied magnetic fields indicates that the increase of NiO concentration leads to the increase of magnetic disorder, and hence weaken the ferromagnetic order. However, NiO and NiO₂ did not strongly affect the magnetic property of the LSMO. For electrical properties, when the NiO concentration increased, the metal-insulator transition (T_{MI}) shifted from 264 K to 192 K. The introduction of NiO and NiO₂ acts as the additional grain boundary effects cause the enhanced MR effect at low temperature which also known as Low Field Magnetoresistance (LFMR). This effect is due to the spin polarized tunneling of electron at the grain boundaries.

Acknowledgement

The authors gratefully acknowledge the support from the Ministry of Education (MOE) for the grant under the Fundamental Research Grant Scheme (FRGS) vote: 02-01-14-1469FR: Enhancement of Magnetoresistance Effect in La-(Sr, Ca)-Mn-O/Sb₂O₃, CeO₂, Al₂O₃ Composites for Low-Field Magnetic Sensor.

References

1. E. Dagotto, T. Hotta, A. Moreo, (2001). Colossal magnetoresistance material: the key role of phase separation, *Physics Reports* **344**: 1-153.
2. J. B. Goodenough, Theory of the role of covalence in the perovskite-type manganites [La,M(II)]MnO₃, *Physical Review* **100**: 564-573.
3. R. von Helmolt, J. Wecker, B. Holzapfel, L. Schultz, K. Samwer (1993). Giant Negative Magnetoresistance in Perovskite like La_{2/3}Ba_{1/3}MnO Ferromagnetic Films, *Physical Review Letters* **71**: 2331
4. Zener C., (1951). Interaction between the d-Shells in the transition Metals. II. ferromagnetic compounds of manganese with perovskite structure, *Physical Review* **82**: 403.
5. Hwang H. Y., Cheong S. W., Ong N. P., Batlogg B., (1996). Spin-polarized intergrain tunnelling in La_{2/3}Sr_{1/3}MnO₃, *Physical Review Letters* **77**: 2041-2044.
6. Chand U., Yadav K., Gaur A., and Varma G. D., (2011). Magnetic and Magnetotransport Properties of (Pr_{0.7}Sr_{0.3}MnO₃)_{1-x} / NiO_x Composites, *AIP Conference Proceedings* **1349**: 1263.
7. Nasri M., Triki M., Dhahri E., Hlil E. K., Lachkar P., (2013). Electrical transport and magnetoresistance properties of (1-x)La_{0.6}Sr_{0.4}MnO₃/x(Sb₂O₃) composites, *Journal of Alloys and Compounds* **576**: 404-408.
8. Romero M., Faccio R., Pardo H., Tumelero M. A., Cid C. C. P., Pasa A. A., Mombrú A. W., (2016). Microstructure, interparticle interactions and magnetotransport of manganite-polyaniline nanocomposites, *Materials Chemistry and Physics* **171**: 178-184.
9. Phong P. T., Khiem N. V., Dai N. V., Manh D. H., Hong L.V., Phuc N. X., (2009). Low-field magnetoresistance of (1-x)La_{0.7}Ca_{0.3}MnO₃ + xAg composites, *Journal of Alloys and*

10. Dar M. A., Varshney D., (2015). Microstructural properties, electrical behavior and low field magnetoresistance of $(1-x)\text{La}_{0.67}\text{Sr}_{0.33}\text{MnO}_3$ (LSMO) + $(x)\text{Ni}_{0.5}\text{Zn}_{0.5}\text{Fe}_2\text{O}_4$ (NZFO) composites, *Solid State Communications* **224**: 24–33.
11. Gharsallah H., Bejar M., Dhahri E., Hlil E.K., Sajieddine M., (2016). Effect of the annealing temperature on the structural and magnetic behaviors of $0.875\text{La}_{0.6}\text{Ca}_{0.4}\text{MnO}_3/0.125\text{La}_{0.6}\text{Sr}_{0.4}\text{MnO}_3$ composition, *Journal of Magnetism and Magnetic Materials* **401**: 56–62.
12. Nasri M., Khelifi J., Triki M., Dhahri E., Hlil E.K., (2016). Impact of CuO phase on magnetocaloric and magnetotransport properties of $\text{La}_{0.6}\text{Ca}_{0.4}\text{MnO}_3$ ceramic composites, *Journal of Alloys and Compounds* **678**: 427–433.
13. Kim H., Yoo S., Enhanced low field magnetoresistance in $\text{La}_{0.7}\text{Sr}_{0.3}\text{MnO}_3\text{--La}_2\text{O}_3$ composites, (2012). *Journal of Alloys and Compounds* **52**: 30–34.
14. Siwach P. K., Srivastava P., Singh J., Singh H. K., Srivastava O. N., (2009). Broad temperature range low field magnetoresistance in $\text{La}_{0.7}\text{Ca}_{0.3}\text{MnO}_3\text{:nano-ZnO}$ composites, *Journal of Alloys and Compounds* **481**: 17–21.
15. Sheng Z., Sun Y., Zhu X., Song W., Yan P., (2007). Enhanced low-field magnetization and magnetoresistance in nano-MgO added $\text{La}_{2/3}\text{Ca}_{1/3}\text{MnO}_3$ composites, *Journal of Physics D: Applied Physics* **40**: 3300–3305.
16. Gaur A., Varma G. D. (2006). Magnetoresistance behaviour of $\text{La}_{0.7}\text{Sr}_{0.3}\text{MnO}_3$ /NiO composites. *Solid State Communications*, **139(6)**: 310–314.

3.2 Structural properties of yttrium aluminum iron garnet (YAIG) nanoferrite prepared via auto-combustion sol-gel synthesis

Makiyyu Abdullahi Musa, Raba'ah Syahidah Azis, Nurul Huda Osman and Jumiah Hassan

Abstract

This research investigated the structural properties of yttrium aluminum iron garnet ($Y_3Al_xFe_{5-x}O_{12}$, YAIG) ($x = 0.8, 1.6$ and 2.4). The samples were prepared via auto combustion sol-gel technique, using citric acid as chelating agent and fuel for the combustion process, and the obtained powder was heated at 950 °C. X-ray diffraction was employed to confirm the garnet phase formation of the powder samples. Their Lattice constant was found to decrease from 12.4190 Å to 12.3018 Å, while crystallite size increases from 20.2112 to 28.6213 as Al increase from $x = 0.8$ to 2.4 . The measured density decreases from 4.9578 to 4.7716 with increasing Al concentration.

Introduction

The ferrite material, Yttrium Iron Garnet (YIG, $Y_3Al_xFe_{5-x}O_{12}$), has excellent magnetic and magneto-electric properties suitable for various applications in optical and microwave communication devices (Dolgova *et al.*, 2004; Akhtar *et al.*, 2014). YIG is an extremely low loss material at high frequency, due to its narrowest ferromagnetic line width (Rodziah *et al.*, 2012), making it the best magnetic material for various applications (Pardavi-Horvath, 2000). YIG has a cubic crystal structure, with general formula $A_3B_5O_{12}$. Because the crystal sites are occupied only by trivalent ions (Y^{3+} and Fe^{3+}), YIG is exceptionally suitable for magnetic studies (Motlagh *et al.*, 2009; Öztürk *et al.*, 2013). Magnetic properties of YIG and its substituted compounds depend strongly on the sample homogeneity, microstructure and stoichiometry, which makes their preparation technique an important factor (Vajargah *et al.*, 2007; Motlagh *et al.*, 2009; Sadhana *et al.*, 2015; Sharma *et al.*, 2016). Heat treatment is reported to control the magnetic properties of YIG by improving the samples crystallinity and weakening their grain demagnetizing force at higher sintering temperature (Rodziah *et al.*, 2012).

Some new phenomena can be achieved by substituting the magnetic iron (Fe) ions in YIG with nonmagnetic aluminum (Al) ions, which can lead to some interesting applications potentials (Kim *et al.*, 2003; Aldbea *et al.*, 2014; Musa *et al.*, 2017). Yttrium aluminum iron garnet, YAIG ($Y_3Al_xFe_{5-x}O_{12}$) samples were produced in this work, by substituting different concentrations of the iron ions in YIG with aluminum ions, via auto combustion sol-gel technique. The effects of the Al ions substitution on microstructural, electrical and dielectric properties of the YIG powders were studied.

Materials and Methods

Synthesis

The YAIG ($Y_3Fe_{5-x}Al_xO_{12}$: $x = 0.4, 0.8, 1.2, 1.6$ and 2.0) samples were prepared using citrate-nitrate auto combustion sol-gel technique. The starting materials, manufactured by Alfa Aesar with 99.99 % purity, were weighed and mixed according to the equation (1):



The materials were then dissolved in 50 ml of isopropanol according and heated on magnetic hot plate at 50 °C, to form a clear solution. Citric acid ($C_6H_8O_7$) was then added, with constant

stirring at 70 °C for 15 minutes until a brownish gel was formed. With continues heating at 200 – 250 °C for about one hour, the gel completely dried, swells and burnt spontaneously to a dark greenish powder. The formed powder was then ground and crushed in a mortar and then heated at 950 °C for three hours.

Characterization

The structural composition of the powder samples was investigated at room temperature by X-ray diffraction (XRD), using Irel Structure APD 2000 X-ray diffractometer, with Cu K α radiation. Diffraction angle (2θ) range of 10° to 80° was used, with an increment of 0.1°. The data analyzed using X'pert HighScore Plus software, which was compared to the electronic PDF δ library.

Results and discussion

Fig. 1 shows the X-ray patterns of the YAIG ($Y_3Al_xFe_{5-x}O_{12}$; $x = 0.8, 1.6$ and 2.4) powder samples sintered at 950°C. The relevant peaks for garnet structure (400), (420) and (422) are sharply reflected, as matched by ICSD reference code 980021229, 980064818 and 980064820, each possessing a cubic crystal structure and belonging to space group $Ia-3d$.

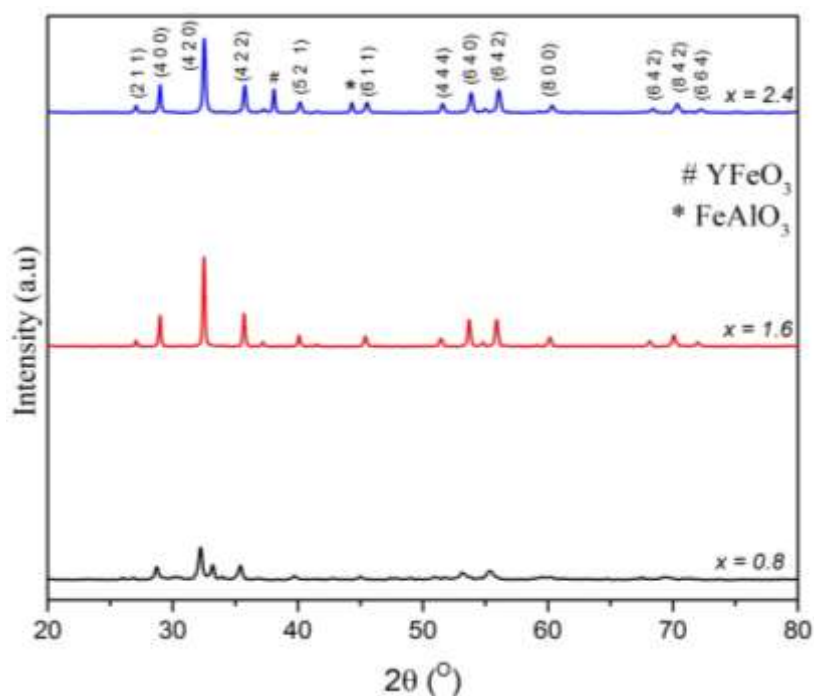


Figure 1: XRD pattern for YAIG powder samples ($x = 0.8, 1.6$ and 2.4)

It was also observed that the XRD peaks move to higher diffraction angles with increasing Al concentration, as shown in Figure 2. This confirmed that the Al^{3+} ions have been incorporated into the (Aldbea *et al.*, 2014). The main peak (4 2 0) was found to move from $2\theta = 32.2084^\circ$ at $x = 0.8$ to 32.5238° at $x = 2.4$, as shown in Fig. 2. Kim *et al.* (2003) and Motlagh *et al.* (2009) reported similar findings for YIAG ($Y_3Fe_{5-x}Al_xO_{12}$) samples with $x = 0$ to 1.0 and 0 to 2.0 respectively.

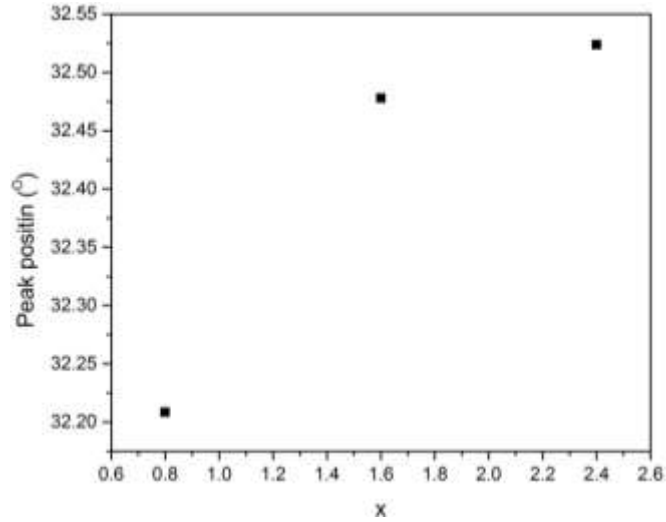


Figure 2: Variation of main peak (4 2 0) position with Al concentration for YAIG powder samples

The lattice constant, a was calculated from the relation

$$a = d\sqrt{h^2 + k^2 + l^2} \quad (1)$$

Where d is the d -spacing and $(h k l)$ are the miller indices.

The lattice constant decreases from 12.4190 Å to 12.3018 Å, due to the decreasing d -spacing as Al concentration increases from $x = 0.8$ to $x = 2.4$, as shown in Figure 3. This is arises from the shorter ionic radius (0.5 Å) of the substituting Al^{3+} ions than that of the substituted Fe^{3+} ions (0.61 Å) (Motlagh *et al.*, 2009).

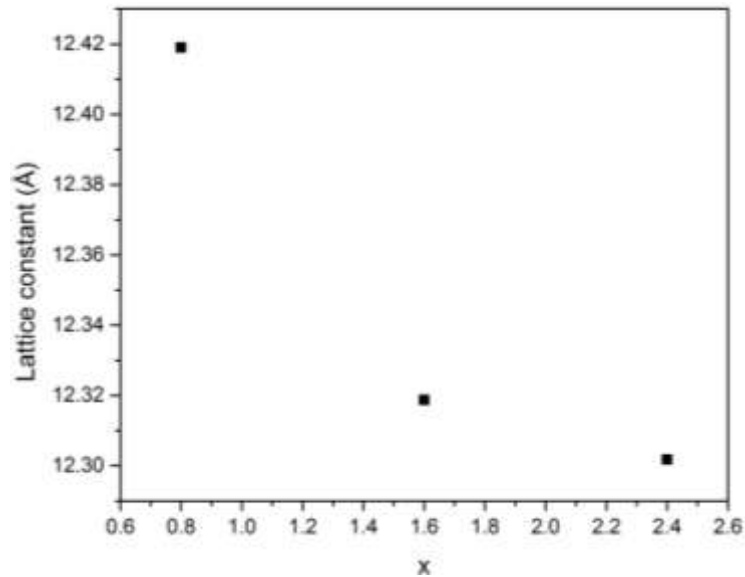


Figure 3: Variation of lattice parameter with Al concentration for YAIG samples

Table 1: X-ray diffraction parameters of the main peak (4 2 0) for $Y_3Fe_{5-x}Al_xO_{12}$ ($x = 0.8$ to 2.4)

Samples (x)	Peak ($h k l$)	Position (2θ ($^\circ$))	d - spacing	Lattice constant (\AA)	Measured Density (g/cm^3)
0.8	(4 2 0)	32.2084	2.7770	12.4190	4.9578
1.6	(4 2 0)	32.4780	2.7546	12.3187	4.9160
2.4	(4 2 0)	32.5238	2.7508	12.3018	4.7716

Theoretical density of the samples is calculated from the relation

$$d_{x\text{-ray}} = \frac{3M}{Na^3} \quad (2)$$

where $d_{x\text{-ray}}$ is the x-ray density, M is the molecular mass, N is Avogadro number and a is the lattice parameter.

The density was observed to decrease from 4.9578 g/cm^3 at $x = 0.8$ to 4.7716 g/cm^3 at $x = 2.4$ (Table 1). This is because Al ions has lower molecular mass (26.9815 u) compared to Fe ions (55.8450 u).

Conclusion

The YAIG powder samples have been successfully prepared via citrate-nitrate auto-combustion sol-gel technique. Their garnet phase formation was achieved, as observed by XRD. Incorporation of the substituted Al into the garnet structure was observed to shift the diffraction peaks to higher angles. The smaller ionic radius of the substituted Al^{3+} , compared to Fe^{3+} , was found to decrease the samples lattice parameter, a . The reduced molecular mas of Al decreased density of the samples.

Acknowledgement

The authors would like to thanks to Research University Grant, Universiti Putra Malaysia (UPM) for the financial support (Vot. No. 9542700 and 9539100).

References

- Akhtar, M. N., Khan, M. A., Ahmad, M., Murtaza, G., Raza, R., Shaukat, S. F., and Raza, M. R. (2014). $Y_3Fe_5O_{12}$ nanoparticulate garnet ferrites: comprehensive study on the synthesis and characterization fabricated by various routes. *Journal of Magnetism and Magnetic Materials*, 368, 393-400.
- Aldbea, F. W., Ibrahim, N. B., and Yahya, M. (2014). Effect of adding aluminum ion on the structural, optical, electrical and magnetic properties of terbium doped yttrium iron garnet nanoparticles films prepared by sol-gel method. *Applied Surface Science*, 321, 150-157.
- Dolgova, T., Fedyanin, A., Aktsipetrov, O., Nishimura, K., Uchida, H., and Inoue, M. (2004). Nonlinear magneto-optical Kerr effect in garnet magnetophotonic crystals. *Journal of applied physics*, 95(11), 7330-7332.

- Kim, C. S., Min, B. K., Kim, S. J., Yoon, S. R., and Uhm, Y. R. (2003). Crystallographic and magnetic properties of $Y_3Fe_{5-x}Al_xO_{12}$. *Journal of Magnetism and Magnetic Materials*, 254, 553-555.
- Motlagh, Z., Mozaffari, M., and Amighian, J. (2009). Preparation of nano-sized Al-substituted yttrium iron garnets by the mechanochemical method and investigation of their magnetic properties. *Journal of Magnetism and Magnetic Materials*, 321(13), 1980-1984.
- Musa, M. A., Osman, N. H., Hassan, J., and Zangina, T. (2017). Structural and magnetic properties of yttrium iron garnet (YIG) and yttrium aluminum iron garnet (YAlG) nanoferrite via sol-gel synthesis. *Results in Physics*, 7 (2017), 1135-1142.
- Öztürk, Y., Erol, M., Çelik, E., Mermer, O., Kahraman, G., and Avgýn, I. (2013). Structural And Magnetic Properties Of Cerium-Doped Yttrium-Iron Garnet Thin Films Prepared On Different Substrates Using The Sol-Gel Process. *Original scientific article/Izvirni znanstveni ~lanek*, 47(1)(59), 59-63.
- Pardavi-Horvath, M. (2000). Microwave applications of soft ferrites. *Journal of Magnetism and Magnetic Materials*, 215, 171-183.
- Rodziah, N., Hashim, M., Idza, I. R., Ismayadi, I., Hapishah, A. N., and Khamirul, M. A. (2012). Dependence of developing magnetic hysteresis characteristics on stages of evolving microstructure in polycrystalline yttrium iron garnet. *Applied Surface Science*, 258(7), 2679-2685.
- Sadhana, K., Ramana Murthy, S., and Praveena, K. (2015). Structural and magnetic properties of Dy^{3+} doped $Y_3Fe_5O_{12}$ for microwave devices. *Materials Science in Semiconductor Processing*, 34, 305-311.
- Sharma, P., Thakur, P., Mattei, J. L., Queffelec, P., and Thakur, A. (2016). Synthesis, structural, optical, electrical and Mössbauer spectroscopic studies of Co substituted $Li_{0.5}Fe_{2.5}O_4$. *Journal of Magnetism and Magnetic Materials*, 407, 17-23.
- Vajargah, S. H., Madaah Hosseini, H. R., and Nemati, Z. A. (2007). Preparation and characterization of yttrium iron garnet (YIG) nanocrystalline powders by auto-combustion of nitrate-citrate gel. *Journal of Alloys and Compounds*, 430(1-2), 339-343.

3.3 Microwave-absorbing properties of $\text{Sr}_4\text{Me}_2\text{Fe}_{36}\text{O}_{60}$ Me= (Mg-Zn, Mn-Zn) composite in X-band and Ku-band frequencies

Muhammad Misbah Muhammad Zulkimi, Raba'ah syahidah Azis, Ismayadi Ismail, Khamirul Amin Matori, Zulkifly Abbas, Fadzidah Mohd Idris, Farah Nabilah Binti Shafiee

Abstract

In this work, the microwave absorption properties of U-type strontium hexaferrite ($\text{Sr}_4\text{Me}_2\text{Fe}_{36}\text{O}_{60}$) with different substituted were investigated. U-type strontium hexaferrite ($\text{Sr}_4\text{Me}_2\text{Fe}_{36}\text{O}_{60}$ Me= (Mg-Zn, Mn-Zn)) have been fabricated by high energy ball mill process and sintered at 1100 °C. The composite of preparation ferrite powder with epoxy resin as polymer was prepared. The composite were prepared with 2 mm thickness. The microstructures, microwave properties of U-type strontium hexaferrite composites have been measured using FESEM, and the composite was measure with Vector Network Analyzer in the frequency range of 8-18 GHz. The average particles of the sample were in the range 150-200 nm. The reflection loss (RL) of U-type strontium hexaferrite composites backed with a conducting plate indicate that the composite possess good microwave-absorbing properties. The results show that U-type strontium hexaferrite ($\text{Sr}_4\text{Me}_2\text{Fe}_{36}\text{O}_{60}$) with Me = Mn-Zn have high minimum RL value for all thickness compare to the ($\text{Sr}_4\text{Me}_2\text{Fe}_{36}\text{O}_{60}$) with Me = Mg-Zn.

Keywords: U-type Strontium Hexaferrite ($\text{Sr}_4\text{Me}_2\text{Fe}_{36}\text{O}_{60}$ Me = (Mg-Zn, Mn-Zn) composite), Reflection Loss (RL).

Introduction

Recent growth of research in the field of microwave (MW) absorbing materials working in higher frequency range is driven by the ever-increasing requirement of exploiting electromagnetic (EM) waves for wireless telecommunication systems and reduction of radar signatures, [1,2]. Wave absorbing materials are required to have a large electric and magnetic loss in the frequency range of interest. The usual method for designing wave-absorbing materials is to find a zero reflection condition. Conditions are required to be satisfied by lossy materials. The first is “matched characteristics impedance”, in which the intrinsic impedance of the material is made equal to the intrinsic impedance of free space. This entails making the dielectric constant and magnetic permeability of the material equal to each other. Second, the incident electromagnetic wave must be entered and attenuated rapidly through the material layer, thus reducing the emerging wave to acceptably low magnitude [3]. Among the materials used in MW applications, ferrites exhibits an interesting behavior, absorbing energy from EM, and present the best relation between the absorber’s performance and its final thickness.

The spinel ferrites can be used only up to 3 GHz frequency range, but the hexaferrites can be used in the whole GHz region, due to their intrinsic uni-axial anisotropic property. The hexaferrites are ferrites with complex crystal structure of $\text{AO-Fe}_2\text{O}_3\text{-MeO}$ (known as magneto-plumbite structure), where A=Ba, Sr, Ca, or La and Me = a bivalent transition metal. The different stable phases of hexaferrite in the increasing order of complexity are M, Y, W, Z, X and U [4-6]. Among these stable phases, U-type hexaferrite phase that has the most complex crystal structure and largest unit cell size has been least studied. Few reports regarding the procedure for preparation of single phase of U-type hexaferrite, its thermal stability range, crystal structure and observation of ferromagnetic resonance with cobalt as metallic ion had been reported [7-13]. Only few work has been done for determination of its

MW absorbing properties [4,14,15]. The MW absorption and EM properties in these materials can be controlled by choosing the proper combination of metallic ions as well as the base oxide ion (AO) in one way and by varying the microstructure, processing parameters and porosity in another way [16].

This paper discuss the microwave absorption characteristic of Strontium hexaferrite ($\text{Sr}_4\text{Me}_2\text{Fe}_{36}\text{O}_{60}$ Me= $\text{Mn}_{2-x}\text{Zn}_x$, $\text{Mg}_{2-x}\text{Zn}_x$; $x = 1.0, 0.5$ and 0.7) -composite of a single layer absorber. The microwave absorbing properties were studied as function of frequency and Me^{2+} content.

Experiment

Materials

The starting materials for preparation of Strontium hexaferrite ($\text{Sr}_4\text{Me}_2\text{Fe}_{36}\text{O}_{60}$ Me= $\text{Mn}_{2-x}\text{Zn}_x$, $\text{Mg}_{2-x}\text{Zn}_x$) were strontium Carbonate (SrCO_3), Manganese oxide (MnO) 99%, Magnesium Oxide (MgO), Zinc Oxide (ZnO) and iron oxide (Fe_2O_3) 99.5% from Alfa Aesar. Epoxy resin was used to prepared magnetic nanocomposite.

Preparation of hexaferrite and hexaferrite-nanocomposite

The starting powder were weighed according to targeted proportions and mixed using ball milling for homogeneity. The powder mixtures was further milled using a SPEX8000D mill in a hardened steel vial together with 10 grinding balls having a diameter 12 mm each to get nanometersized particles. The milling time and ball to powder weight ratio (BPR) were 6 h and 10:1, respectively, and were used to obtain nanoparticles as the starting powder. It was then sintered at 1100 °C for 10 h using a heating rate of 4 °C/min.

The composite specimens for measurement of the microwave absorber properties were prepared by mixing sintered Strontium nickel hexaferrite and epoxy resin with concentration of 60:40 by weight. The mixing liquid was pouring into the sample holder and dry in the room temperature for 24 h. The composite were prepared with thickness 2 mm.

Measurement properties

To investigate ferrite phase formation, X-ray diffraction (XRD) spectra of sintered sample powders were recorded. The particle size after high energy ball mill and sintered was measured using an FEI NOVA NanoSEM230 machine. The magnetic properties including intrinsic coercivity, saturation magnetization of hexaferrite samples were measured at a room temperature using a vibrating sample magnetometer. The evaluation of the microwave absorption properties was studied by using vector network analyser system. Variation of the reflection loss in (dB) versus frequency in the range of 8-18 GHz has been investigated.

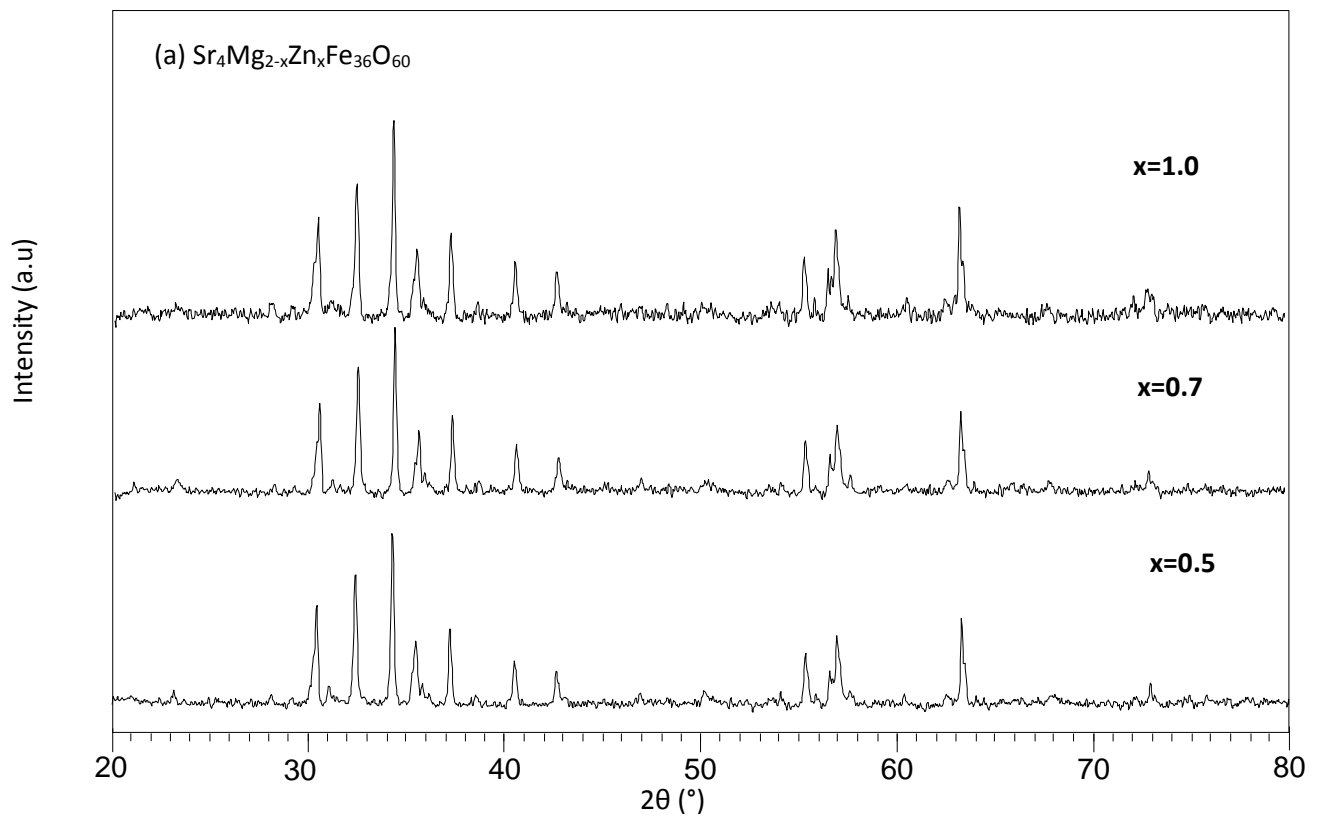
Results and discussion

Phase and Microstructure Analysis

Figure 1 showed the XRD spectra for sintered sample hexaferrite powder. The signature of U-type hexaferrite has been representing at peaks around 30-38°, 40-43°, 55-58° and 64°. U-type hexaferrite originates from the combination of 2M-type and 1Y-type structure

[16,17]. If the sintering or calcinations temperature is too high, Z-type will be formed instead of M-type or Y-type and there will be lesser reaction between M and Y types to form U-type, resulting in a multiphase hexaferrite structure. Therefore, temperature must be optimized to prevent the formation of Z-type hexaferrites and possible low sintering temperature to improve the phase purity of the sample by reducing both unwanted phase of Fe and Z-type hexaferrite [18]. In this project, the sintering was optimizing using 1100 °C for 10 hours holding time because of the formation of Fe phases and Z-type hexaferrite when sintering temperature above 1275 °C. XRD spectra reveals that U-type hexagonal phase for both series does not change with composition.

Microstructure plays an important role in achieving the desired magnetic and microwave properties of hexaferrite for microwave applications. Field Emission Electron Microscopy (FESEM) images for both series sintered samples, for $x=0.5$, 0.7 and 1.0 are shown in Figure 2a (I-III) and 2b (I-III). Based on figure the platelets that nearly hexagonal can be seen for both series. Barium and strontium hexaferrite nanoparticles with hexagonal pyramidal and hexagonal plate-like morphology are potential materials for the radar absorption applications [19-21]. It may be argued that in addition to the substantial effects related to electrical and magnetic behaviour, the substituted samples indicate remarkable contribution to the morphology of the materials. Hence, morphology of the sample can be easily tuned according to the research interest by different amount of composition [22]. The average particle sizes in the range of 100 nm to 150 nm depending on the value of x . Average particle size was obtained quite small compare to other researcher has been done [18].



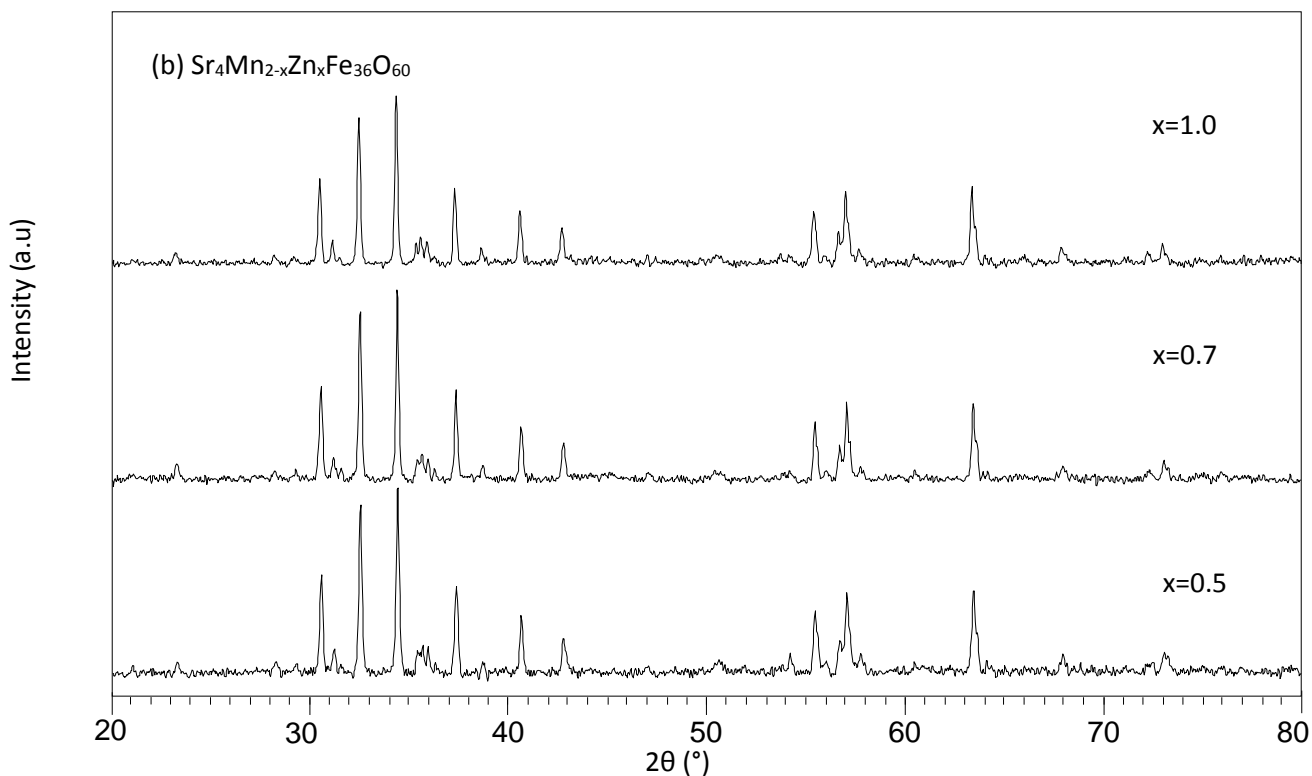


Figure 1: XRD spectra for (a) $\text{Sr}_4\text{Mg}_{2-x}\text{Zn}_x\text{Fe}_{36}\text{O}_{60}$ and (b) $\text{Sr}_4\text{Mn}_{2-x}\text{Zn}_x\text{Fe}_{36}\text{O}_{60}$ powder ($x=0.5, 0.7$ and 1.0)

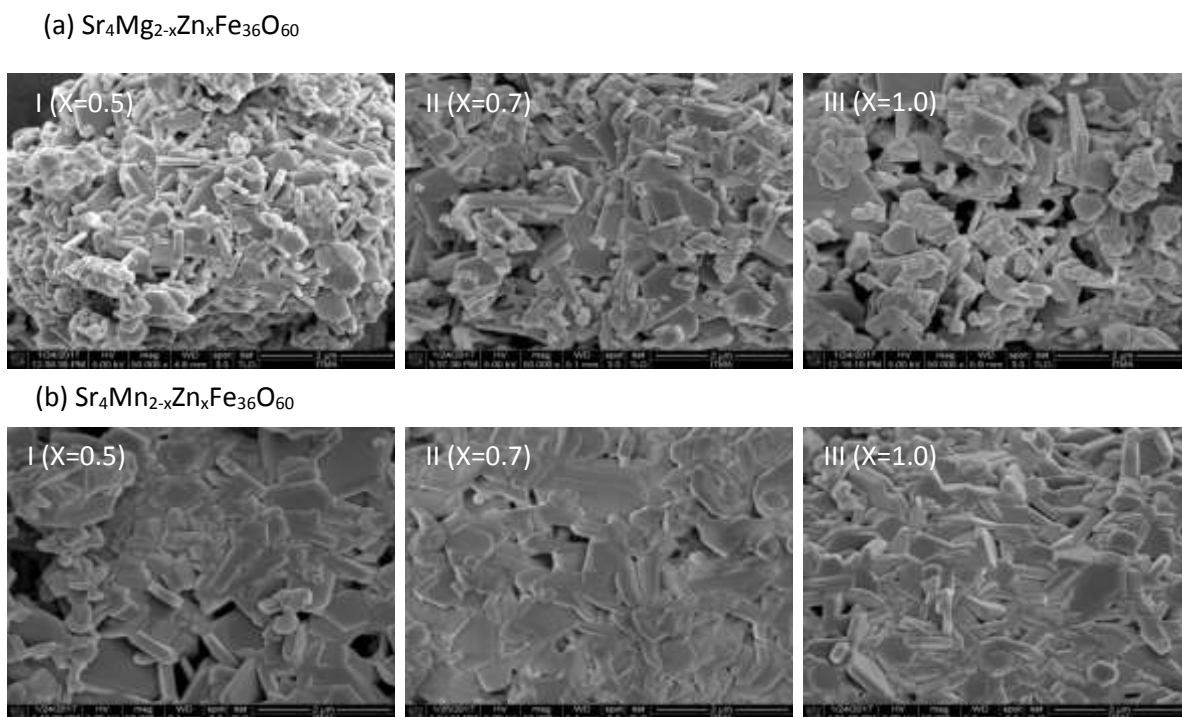


Figure 2: FESEM images for (a) $\text{Sr}_4\text{Mg}_{2-x}\text{Zn}_x\text{Fe}_{36}\text{O}_{60}$ and (b) $\text{Sr}_4\text{Mn}_{2-x}\text{Zn}_x\text{Fe}_{36}\text{O}_{60}$ powder ($x=0.5, 0.7$ and 1.0)

Magnetic Properties

Figure 3 (a) and (b) showed the magnetic hysteresis curves of the strontium U-type hexaferrite with different substitution and varies of compositions ($x=0.5, 0.7$ and 1.0). The details of magnetization (M_s), retentivity (M_r) and coercivity were listed in table 1. For sample $\text{Sr}_4\text{Mg}_{2-x}\text{Zn}_x\text{Fe}_{36}\text{O}_{60}$ showed, with increasing x up to 0.7 , the saturation magnetization, remanence magnetization and coercivity decreased and increased for $x=1.0$. Meanwhile, for $\text{Sr}_4\text{Mn}_{2-x}\text{Zn}_x\text{Fe}_{36}\text{O}_{60}$, with increasing x up to 0.7 , the saturation magnetization, remanence magnetization and coercivity increase and decreased for $x=1.0$. This decrease may be ascribed to the hard reversible displacement in the direction of applied field. Harder the displacement, the smaller will be the value of M_s . This decrease may be due to break of co-linearity and spin canting [23]. The increase in value of M_s for the other samples can be ascribed to the occupancy of down spin substitution tetrahedral site by nonmagnetic zinc ion. This results in increase in number of unpaired electrons with downward spin, causing M_s to increase [24].

Coercivity H_c is one most important parameter in the hysteresis loop. It is well known that the coercivity is highly dependent on major parameters such as the particle size and anisotropy constant. With increasing on particle size, the coercivity will be decreased. According to Figure 2 on FESEM images and average particle size (Table1), with increasing substitution content x for $\text{Sr}_4\text{Mg}_{2-x}\text{Zn}_x\text{Fe}_{36}\text{O}_{60}$ sample the particle size increased and the coercivity decreased. For $\text{Sr}_4\text{Mn}_{2-x}\text{Zn}_x\text{Fe}_{36}\text{O}_{60}$ sample, when increasing of substitution content x up to 0.7 , the average particle size increased, the coercivity value decreased and when content $x=1.0$, the coercivity increased when average particle size increased.

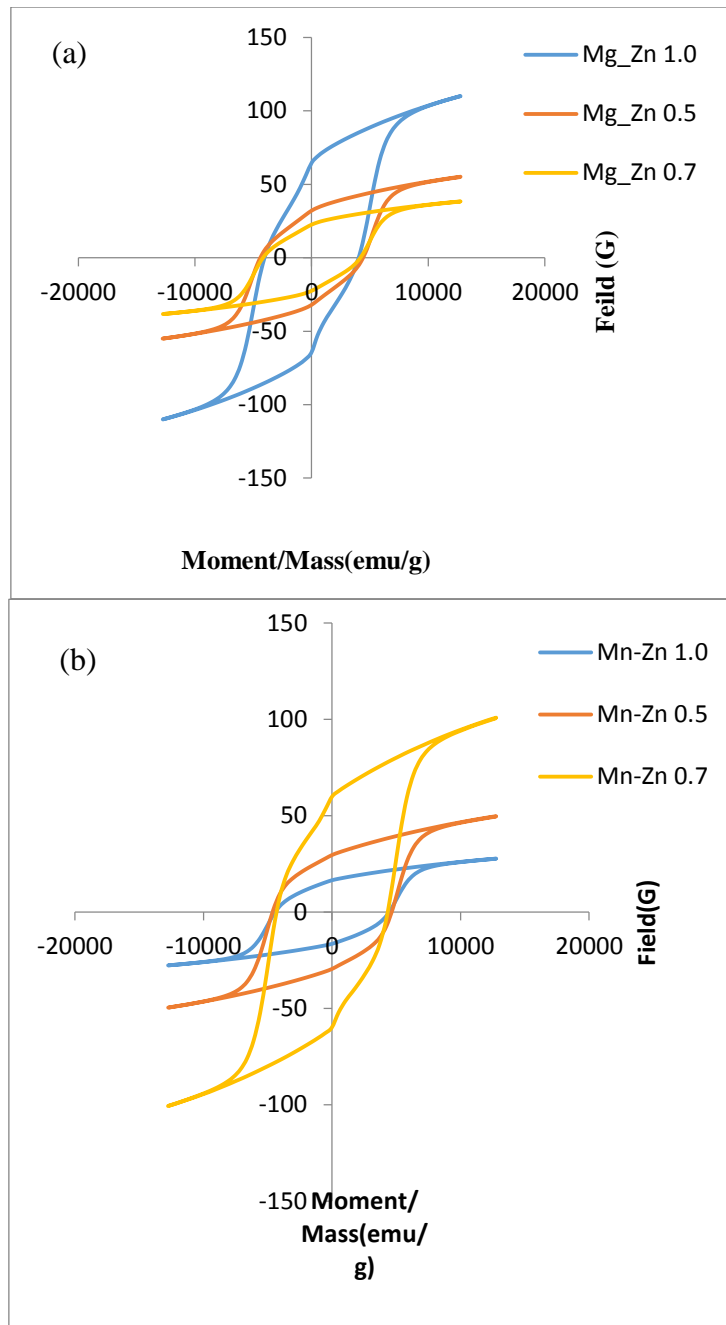


Figure 3: The hysteresis loop for (a) $\text{Sr}_4\text{Mg}_{2-x}\text{Zn}_x\text{Fe}_{36}\text{O}_{60}$ and (b) $\text{Sr}_4\text{Mn}_{2-x}\text{Zn}_x\text{Fe}_{36}\text{O}_{60}$ powder ($x=0.5, 0.7$ and 1.0)

Table 1: Details of Magnetization (Ms), Retentivity (Mr), Coercivity (Hc) and Average particle size for $\text{Sr}_4\text{Mg}_{2-x}\text{Zn}_x\text{Fe}_{36}\text{O}_{60}$ and $\text{Sr}_4\text{Mn}_{2-x}\text{Zn}_x\text{Fe}_{36}\text{O}_{60}$ powder ($x= 0.5,0.7$ and 1.0)

List of materials	Composition (X)	Magnetization (Ms) (emu/g)	Retentivity (Mr) (emu/g)	Coercivity (Hc) (G)	Average particle size (nm)
$\text{Sr}_4\text{Mg}_{2-x}\text{Zn}_x\text{Fe}_{36}\text{O}_{60}$	0.5	55.13	32.08	4384.00	126.04
	0.7	38.35	22.53	4160.30	135.32
	1.0	110.07	64.31	4017.30	134.70
$\text{Sr}_4\text{Mn}_{2-x}\text{Zn}_x\text{Fe}_{36}\text{O}_{60}$	0.5	49.69	29.57	4623.40	122.20
	0.7	100.82	59.78	4306.60	124.49
	1.0	27.71	16.51	4413.30	116.68

Microwave properties of hexaferrite composites

The frequency dependence of reflection loss was measured using vector network analyser in the X-band (8-12 GHz) and Ku-band (12-18 GHz). The variation of the reflection loss versus frequency in different of x for composites hexaferrite with thickness 2 mm is shown in Figure 4. Considering the results, by comparing with Mg-substitution, Mn-substitution showed the optimum reflection loss. The Mn-substitution of Strontium U-type hexaferrite reached a minimum reflection loss of -32.89 dB at 11.50 GHz and a bandwidth of at least 0.7 GHz for $x= 0.5$. For $x= 0.7$ showed minimum reflection loss of -19.48 dB at 17.7 GHz and bandwidth of 0.3 GHz. For $x=1.0$, the minimum reflection loss of -14.05 dB at 17.50 GHz and bandwidth of 0.3 GHz. The reflection loss of Mg-substitution has been listed in Table 2.

It is well known that the intrinsic magnetic properties of ferrites depend on their chemical composition. Structurally, all hexaferrite phases are made of by stacking a combination of R, S and T blocks directly or with inverted by 180° . The skeleton of these blocks basically consists of different layers of oxygen in which some oxygen atom has been replaced by A (Ba, Sr, Ca, or La) atom. The metal and ferric ions occupy the interstitial (tetrahedral, octahedral and rhombohedral) sites in this frame [16].

It well known that Zn^{2+} and Mn^{2+} ions showed a greater preference for tetrahedral sites and Mg^{2+} ions are to have a greater preference for octahedral sites. In ferrites, Mn, Mg and Cu can present distributions in both crystallographic sites and Mn can assume different valences ($\text{Mn}^{2+}/\text{Mn}^{3+}$) to maintain the electronic equilibrium in each of the sites [25]. The introduction of Mn^{2+} ions into the tetrahedral site can force the transfer of the same quantity of Fe^{2+} ions from the tetrahedral site to the octahedral site. The presence of Fe^{2+} and Fe^{3+} in the same crystallographic site favors the electron-hopping mechanism, influenced by the presence of Mn^{2+} and Mn^{3+} , contributing to increase the electromagnetic losses [26]. The increased of electromagnetic losses due to the decreasing electrical resistivity in ferrite. The

decreasing in electrical resistivity because of the existence of ions with more than one valence in the same crystallographic site may favor the transfer of electrons between them. In the cases of Mg-substitution, the electromagnetic losses did not increased because of the existence the stable oxidation state (+2) should not favor the reduction of electric resistivity.

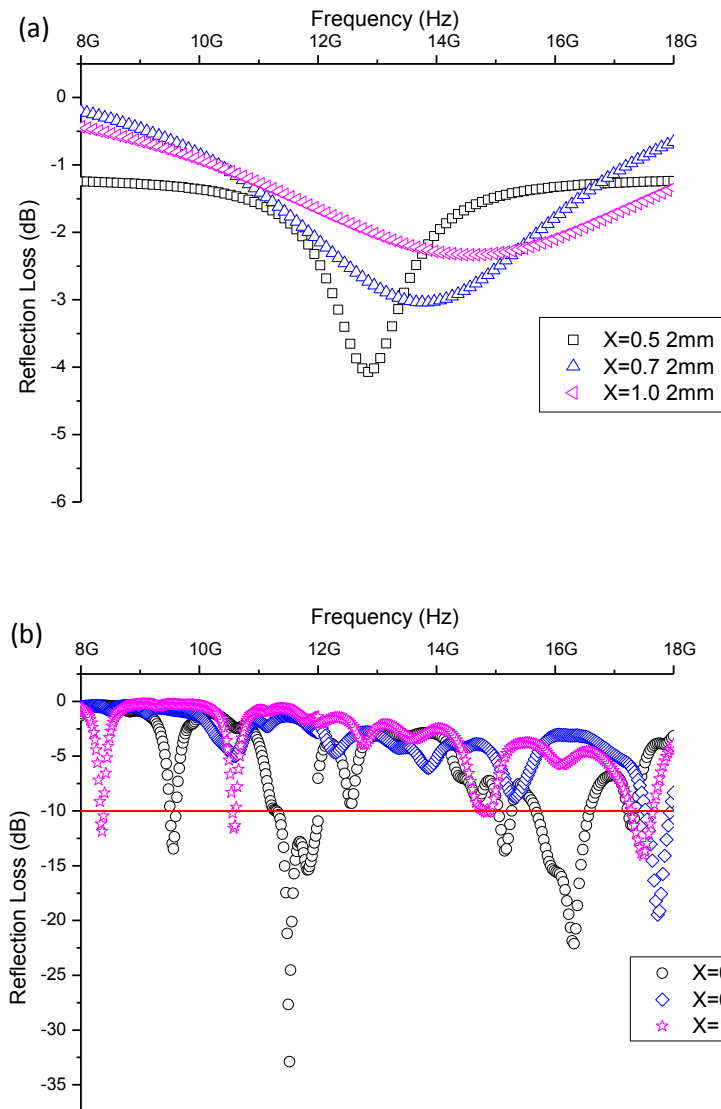


Figure 4: Variation of reflection loss in Strontium hexaferrite as a function of composition in the X-band and Ku-band frequency range: (a) $\text{Sr}_4\text{Mg}_{2-x}\text{Zn}_x\text{Fe}_{36}\text{O}_{60}$ and (b) $\text{Sr}_4\text{Mn}_{2-x}\text{Zn}_x\text{Fe}_{36}\text{O}_{60}$ powder ($x= 0.5,0.7$ and 1.0).

Table 2: The details of Strontium hexaferrite ($\text{Sr}_4\text{Me}_2\text{Fe}_{36}\text{O}_{60}$ Me= $\text{Mn}_{2-x}\text{Zn}_x$, $\text{Mg}_{2-x}\text{Zn}_x$) composite and their absorber properties

List of composite materials	(x)	Reflection Loss (dB) (GHz) Thickness (2mm)	Bandwidth (RL<-10 dB) (GHz)
$\text{Sr}_4\text{Mg}_{2-x}\text{Zn}_x\text{Fe}_{36}\text{O}_{60}$	0.5	-4.30 (12.80)	-
	0.7	-3.00 (13.90)	-
	1.0	-2.40 (14.50)	-
$\text{Sr}_4\text{Mn}_{2-x}\text{Zn}_x\text{Fe}_{36}\text{O}_{60}$	0.5	-32.89 (11.50)	0.7
	0.7	-19.48 (17.70)	0.3
	1.0	14.05 (17.50)	0.3

Conclusion

Single layer microwave absorber of strontium U-type hexaferrite ($\text{Sr}_4\text{Me}_2\text{Fe}_{36}\text{O}_{60}$) with Mn and Mg substitution for different composition x have been prepared by using the composites based on epoxy and sintered strontium U-type hexaferrite. Electromagnetic properties and microwave absorption properties of these samples were investigated in detail. Mg substitution in this sample was found the absorption below 90 % throughout the frequency range (8-12 GHz). A fact can be explained by electromagnetic loss. The microwave absorption is obtained to be maximum with the Mn substitution, the absorption is 90 % and above throughout of the frequency range (8-12 GHz) with a thickness of composites 2 mm. Based on requirement, the thickness must be small for absorbing material, this composite sample can be applied for absorption of MW radiation such as reducing EMI (electromagnetic interference) and other.

Acknowledgement

The researchers wish to thank the Universiti Putra Malaysia, Malaysia, for provided under work under the Universiti Putra Malaysia grants GP-IPS 9533300 and FRGS 5524942 the graduate Research Fellowship and NanoMag (Nanostructured Polycrystals and Magnetism Group) for support of this project.

References

1. Devender, S.R. Ramasamy, Int. Conf. Electromagnetic Interference and Compatibility (INCEMIC-97), New Jersey, 7B-7, 1997, pp. 459-466.
2. R.A. Stonier, SAMPE J. 27 (4) (1991) 9-17.
3. Mohammad Hossein Shams, Seyed Mohammad Ali Salehi , Ali Ghasemi , Materials Letters 62 (2008) 1731-1733.
4. S.M. Abbas, Preparation and characterization of microwave absorbing materials, Doctor Thesis, Indian Institute of Technology Delhi India, 2007, pp. 19-32.
5. J. Smit, H.P.J. Wijn, in: Ferrite, Philips Technical library, Netherland, 1959, pp. 176-210.

6. W.H.V. Aulock, in: Hand book of Microwave Ferrite Materials, Academic Press, London, 1965, pp. 451–511.
7. D. Lisjak, V.B. Bregar, A. Znidarsic, M. Drofenik, *J. Optoelectron. Adv. Mater.* 8 (2006) 60–65.
8. D. Lisjak, M. Drofenik, *J. Magn. Magn. Mater.* 272 (2004) e1817–e1819.
9. D. Lisjak, M. Drofenik, *J. Appl. Phys.* 93 (2003) 8011–8013.
10. C. Sudakar, G.N. Subbanna, T.R.N. Kutty, *J. Magn. Magn. Mater.* 263 (2003) 253–268.
11. D. Lisjak, Paul Macguiness, M. Drofenik, *J. Mater. Res.* 21 (2006) 420–427.
12. D. Lisjak, Darko Makovec, Miha Drofenik, Formation of U-type hexaferrites, *J. Mater. Res.* 19 (2004) 2462–2470.
13. Zhang Haijun Liu Zhichao Yao Xi Zhang Liangying, Wu Mingzhong, *J. Mater. Sci. Eng. B* 97 (2003) 160–166.
14. Mukesh C. Dimri, S.C. Kashyap, Dinesh C. Dube, *IEEE Trans. Magn.* 42 (2006) 3635–3640.
15. Darja Lisjak Vladimir, B. Bregar, Miha Drofenik, *J. Magn. Magn. Mater.* 310 (2007) 2558–2560.
16. R.S. Meena, S. Bhattachrya, R. Chatterjee, , *J. Magn. Magn. Mater.* 322 (2010) 1923.
17. R.S. Meena, S. Bhattachrya, R. Chatterjee, *Mater. Sci. Eng. B* 171 (2010) 133.
18. S.R. Shannigrahi , W.Q. Au, V. Suresh Kumar , L. Liu c, Z.H. Yang , C. Cheng , C.K.I. Tan a, R.V. Ramanujan, *J. Magn. Magn. Mater.* 325 (2013) 63–68.
19. M.M. Hessian, M.M. Rashad, K. El-Barawy, *J. Magn. Magn. Mater.* 320 (2008) 336–343.
20. X. Huang, J. Chen, L. Wang, Q. Zhang, , *Rare Met.* 30 (2011) 44–48.
21. J. Xu, H. Zou, H. Li, G. Li, S. Gan, G. Hong, , *J. Alloys Compd.* 490 (2010) 552–556.
22. Gholam Reza Gordani, Marzieh Mohseni, Ali Ghasemi, Sayed Rahman Hosseini, *Mater Res Bull* 76 (2016) 187–194.
23. I. Bsoul and S.H. Mahmood: *J. Alloys Compd.* 489(1), 110(2010).
24. A. Sharbati, G.R. Amiri, and R. Mousarezaei. *J. Electron. Mater.* 44(2), 715 (2015).
25. Alexandre R. Bueno, Maria L. Gregori, Maria C.S. No´ brega, , *J. Magn. Magn. Mater.* 320 (2008) 864–870.
26. B. Li, J. Zhou, Z. Yue, Z. Gui, L. Li, *Mater. Sci. Eng. B* 99 (2003) 252

3.4 Role of Magnetite Nanoparticles for Metal Absorbents in Waste Water Treatment

Nur Asyikin Ahmad Nazri, Raba'ah Syahidah Azis, Abdul Halim Shaari, Norlaily Mohd Saiden, Ismayadi Ismail, Jumiah Hassan and Hafsalina Che Man

Abstract

Increase industrial waste constitutes various kinds of metal pollution in natural water. There are at least 20 metals which cannot be degraded and destroyed. There are numerous methods currently employed to remove and recover the metals from our environment and many physico-chemical methods have been proposed for their removal from wastewater. Adsorption is one of the alternatives for such cases and is an effective purification and separation technique used in industry especially in water and wastewater treatments. There is increasing research interest in using alternative low-cost adsorbents. The use of the process steel waste product as the low-cost adsorbents was investigated as a replacement for current costly methods of removing heavy metal ions from aqueous solutions. Magnetite nanoparticle is used in wastewater treatment because of its specific large surface area, high reactivity in adsorption and recoverable from treated water via magnetic separation technology. This review paper will discuss the progress from the previous research done to find the solution so that more clean water can be treated using magnetite nanoparticle as the metal absorbents.

Keywords: magnetite nanoparticles, magnetic adsorbents, metals removal, wastewater treatment

Introduction

Over the past few years, the scientific research has witnessed a dramatic increase in the number papers published on implications and applications of magnetite (Fe_3O_4) nanoparticles (MNPs). Magnetite is a common iron oxide that exhibits outstanding physico-chemical properties due to the presence of both Fe(II) and Fe(III) in its structure. It behaves as superparamagnetic as the particle size reduced to nanometers. MNPs have been used for biomedical applications [14], electrical applications, communication applications and recently environmental applications. A thorough synthesis of recent literature is needed with regard to environmental implications and applications of MNPs in order to understand the current status of research and to explore future opportunities. Besides different synthesis method will yield different use of the MNPs. The MNPs itself have limited efforts on the literature review of environmental aspects [2]. Even though hybrid of MNPs with others composition or surfactants give wider applications. Functionalized MNPs known as hybrid magnetite nanocomposites. In order to functionalise the MNPs researchers have come with many methods. The synthesis methods of MNPs will effects the functionalise method. The synthesis methods were divided into three categories which are physical, chemical and biological. The cost effective method of physical methods is mechanical alloying. This method was adopted since it can yield large scale amount of MNPs. The magnetite nanocomposite shows higher solubility in water media compared to MNPs solely. Therefore numerous methods currently employ to functionalise the MNPs. Besides magnetite can be easily self assemble with the surfactants or polymers. The new surface morphology after functionalise automatically increase the affinity of the magnetite to remove the heavy metal ions application. Magnetite nanocomposites widely used in biomedical to remove heavy metal ions in blood. Recently, published research prove that magnetite nanocomposites able to increase the heavy metals ions in polluted water. Current conventional methods that give higher attentions of more researchers are using activated carbon adsorptions. The adsorption of activated carbon is almost 99% heavy metal ions can be removed. The weakness of this current method is the cost to produce activated carbon is higher and it cannot be regenerate. Another

consequence of using this method is the maintenance of the filtration system which involve of higher cost. Therefore researchers have started to study on using magnetic nanoparticles in removing the heavy metal ions. One of biggest contribution for this method that easily separate of the sorbent and adsorbents from the clean water by using external magnetic field. Industrial waste water contains higher concentrations of heavy metal ions. Unfortunately some of the rivers also were reported contaminated with heavy metal ions which higher toxicity to human life. There are more than 20 types of metals ions in the contaminated industrial waste water. One of known higher toxicity and radiated heavy metal ions is Arsenic followed by lead, Cadmium, Chromium hexavalent, mercury and nickel. The effect of the existence of these heavy metal ions were described in Table 1.

Table 1: The hazardous source and the toxicity effect [1].

Metal	Source	Toxicity Effect
Arsenic	Pesticides, fungicides, metal smelters	Irritation of respiratory system, Liver and Kidney damage, Loss of appetite, nausea and vomiting
Cadmium	Welding, electroplating, pesticide fertilizer, Cd-Ni batteries	Lung, liver and kidney damage; Irritation of respiratory system
Chromium	Paints, electro plating and metallurgy	Lung damage and Irritation or respiratory system
Mercury	Pesticides, batteries, paper industry	Irritation of respiratory system; lung, liver kidney damage, and loss of hearing and muscle coordination
Lead	Paint, pesticide, smoking, automobile emission,mining,	Lung and liver damage; loss of appetite, nausea
Nickel	Electrochemical industries	Lung, liver and kidney damage

This review will discuss more on the role of magnetite, magnetite nanocomposite to increase the efficiency on removal heavy metal ions from waste water.

Magnetite nanoparticles synthesis method

Magnetite nanoparticles shows higher effectiveness in removing heavy metal ions. The smaller particle size of the MNPs will cause the particle size to have higher surface area. Higher surface area of the adsorbents will increase the heavy metal ions adsorbed to the surface. Therefore more heavy metal ions will be removed from the heavy metal ions. The synthesis method of magnetite yield different morphology of MNPs and different affinity to heavy metal ions. The synthesis method from the previous research have been summarise in Table 2 with the advantages and the disadvantages of the method been used. Basically there are three categories of magnetite synthesis method. The large number studied by researchers is wet chemical method. This method was believed to produce large scale of magnetite with tedious chemical rout. Higher numbers of researches were done on co-precipitation, sol-gel and hydrothermal method. The drawback is that difficult to get nanosize without further with sol-gel and hydrothermal method. Sol-gel and hydrothermal method involved higher cost since the raw materials is expensive. The advantages of the two methods that it can produce fine powders of MNPs. Low cost physical synthesis method is mechanical alloying. Micron

size of magnetite crushed to nanosize using higher energy ball milling. This method produced large scale of higher magnetic properties of magnetite [14]. the last method is biological method. Biological methods extract the Fe_3O_4 from seaweed [11], and leaves. The advantage of this method is green synthesis which free chemical consume. Thus, low magnetic response by the magnetite produced.

Table 2: Synthesis of nanoscale magnetite.

Method	Approach	Advantages	Disadvantages
Physical	Ball milling	Large scale production, simple procedure and higher magnetic response	Uncontrollable size, agglomeration
Wet chemical	Co-precipitation, sol gel and hydrothermal	Facile and controllable size	Amorphous nanoparticles, complex procedure, higher cost production
Biological	Biosynthesis	Green chemistry, serves both reducing and capping agent.	Low magnetic response

The production of the different synthesis methods will affect the morphology and the removal efficiency of MNPs. For environmental purposed, the magnetic should have higher surface area, low toxicity, large scale production, higher magnetic response and have ability to functionalise by surfactants or polymers. More attention will be given to the magnetite that having higher affinity. To enhance the affinity of magnetite it needs to be functionalized. So that the surface gives higher electro negativity since the hazardous ions is positive ions.

Hybrid magnetite nanocomposites

Surface of magnetite can be modified by functionalised with suitable surfactants and polymers. the modifications will depends on the applications of the magnetite. Hybrid magnetite nanocomposites is the best word to describe functionalised magnetite nanoparticles. MNPs that synthesis by wet chemical method gives surface hydroxyl around the magnetite surface. Surface hydroxyl groups protonate or deprotonate to generate surface charge $FeOH_2^+$ or FeO^- functions at pH value below or above the pH zero point charge respectively. Magnetite zero point charge is the pH value at which the surface concentrations of $FeOH_2^+$ and FeO^- groups are equal. At lower pH acidic range where magnetite's surface has a net positive charge from $Fe-OH_2^+$ surface groups. Increasing pH leads to increase $Fe-O^-$ groups which enhance deprotonation. Therefore functionalized helps to maintain the surface of the MNPs and remove the heavy metal with pH independent After functionalized with polymers, the surface had more hydroxyl groups which ready to deprotonate with heavy metal ions. there are many methods to functionalized the MNPs such as polymergrafting, self assemble with polyligands, and salinations. Self assemble polyligands usually used for solid or stable Fe_3O_4 . In Figure 1 shows that solid or stable Fe_3O_4 will be charged negative. EDTA or CTAB will give hydroxyl surface to the MNPs to increase the negativity. Hybrid magnetite nanocomposites allow the adsorption to occur at any pH even at pH 7 [12]. Recently polymers functionalized MNPs are receiving much more attention, owing to the advantages of polymers coating will increase repulsive forces to balance the magnetic and the van der Waals attractive forces acting on the NPs. In addition, polymers coating on the surface of iron oxide NPs offer a high potential in

the application of several fields. Moreover, polymer functionalized iron oxide NPs have been extensively investigated due to interest in their unique physical or chemical. The saturation magnetization value of iron oxide NPs will decrease after polymers functionalization.

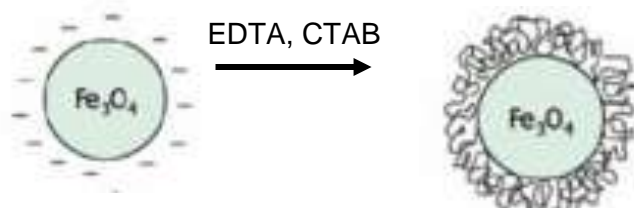


Figure 1: Self assemble or natural process with some polymers [2].

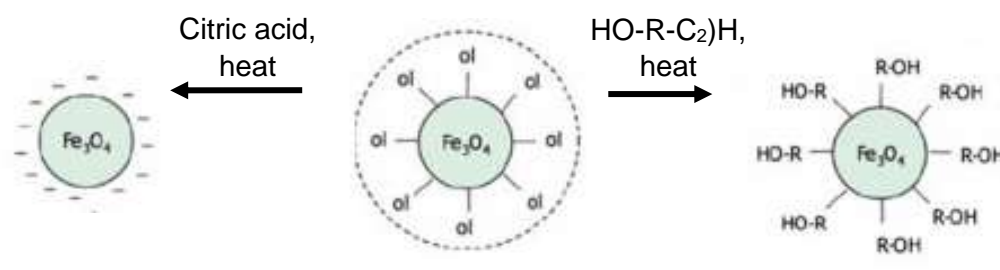


Figure 2: Ligand exchange with higher temperature [2].

One of the aims to functionalise MNPs is to increase the solubility in water solution and ligand exchange reaction is the major approach to realize this aim. Ligand exchange is a well-known method for tuning the surface properties of NPs. It involves adding an excess of ligand to the nanoparticle solution, which results in the displacement of the original ligand on the NPs' surface. Especially, ligand-exchange reactions on noble metal NPs, via the self-assembly of thiols, have been used for many years already [2]. However, more recently, several groups have reported the use of ligand exchange to alter the surface properties of MNPs. Subsequently, as illustrated in Fig. 2, Lattuada and Hatton (2007) [12] reported that the oleic groups initially present on the above nanoparticle surfaces were replaced via ligand-exchange reaction with various capping agents bearing reactive hydroxyl moieties. silane agent is often considered as a candidate for modifying on the surface of iron oxide NPs directly, for the advantages of the biocompatibility as well as high density of surface functional end groups, and allowing for connecting to other metal, polymer or biomolecules [2]. Result reveals that the surface functionalized magnetic particles have a slight dimensional increase in average diameter while retain almost original saturation magnetization; In addition, silanes were found to render the MNPs highly stable and water-dispersible, and it was also found to form a protective layer against mild acid and alkaline environments. Moreover, silane ligand-exchange reaction can make the hydrophobic iron oxide NPs into water dispersible [2].

Hybrid with inorganic compound was studied by Behbhani (2015) using silica. Silica is the most common compound for preparing the functionalized iron oxide NPs, silica-coated MNPs have several advantages as follows: (a) this coating provides not only the stability to MNPs in solution, but also avoids the interparticle interactions and prevent agglomeration generating, (b) this composite MNPs possess a good biocompatibility, hydrophilicity and stability In addition, silica-coating helps in binding the various biological or the other ligands at the MNPs surface for various applications.

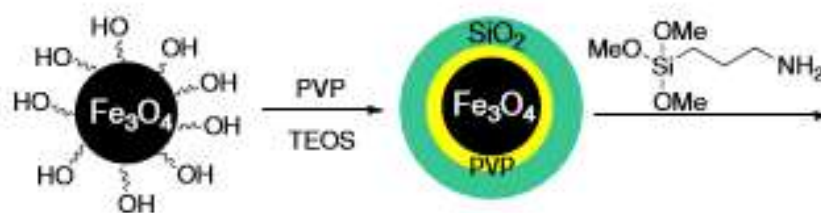


Figure 3: hybrid magnetite with silica compound consists of grafting from as organic inorganic hybrid [3].

Table 1: Summary of functionalized MNPs method.

Hybrid compound	Method	References
Polymers	Natural self assemble, polymergrafting	[2]
Inorganic compound	Silanations	[3]

Conclusion

This review paper was successful discuss on the role of MNPs in environmental application especially waste water treatment. We also discussed method to enhance the removal efficiency which is by functionalised with polymers and inorganic compound. Those methods were studied with different perspectives and considerations of heavy metal ions removal and the cost. From the above discussion, hybrid MNPs nanocomposites with polymers by natural self assemble might be the best and low cost method. This preferable if physical method to synthesis the MNPs was chosen. Therefore hybrid MNPs have high potential to be commercial in waste water treatment for heavy metal ions removal.

Acknowledgement

The authors would like to thanks to Research University Grant (Impact Grants and IPS Grants), Universiti Putra Malaysia (UPM) for the financial support (Vot. No. 9541600 and 9580600). Also thanks to Department of Physics and ITMA for the facilities.

References

1. Barakat, M. A. (2011). New trends in removing heavy metals from industrial wastewater. *Arabian Journal of Chemistry*, 4(4), 361-377.
2. Wu, W., He, Q., & Jiang, C. (2008). Magnetic iron oxide nanoparticles: synthesis and surface functionalization strategies. *Nanoscale research letters*, 3(11), 397.
3. Behbahani, M., Bide, Y., Bagheri, S., Salarian, M., Omidi, F., & Nabid, M. R. (2016). A pH responsive nanogel composed of magnetite, silica and poly (4-vinylpyridine) for extraction of Cd (II), Cu (II), Ni (II) and Pb (II). *Microchimica Acta*, 183(1), 111-121.

4. Badruddoza, A. Z. M., Shawon, Z. B. Z., Tay, W. J. D., Hidajat, K., & Uddin, M. S. (2013). Fe₃O₄/cyclodextrin polymer nanocomposites for selective heavy metals removal from industrial wastewater. *Carbohydrate polymers*, 91(1), 322-332.
5. Rajput, S., Pittman, C. U., & Mohan, D. (2016). Magnetic magnetite (Fe₃O₄) nanoparticle synthesis and applications for lead (Pb²⁺) and chromium (Cr⁶⁺) removal from water. *Journal of colloid and interface science*, 468, 334-346.
6. Tang, S. C., & Lo, I. M. (2013). Magnetic nanoparticles: essential factors for sustainable environmental applications. *Water research*, 47(8), 2613-2632.
7. Dakiky, M., Khamis, M., Manassra, A., & Mer'eb, M. (2002). Selective adsorption of chromium (VI) in industrial wastewater using low-cost abundantly available adsorbents. *Advances in environmental research*, 6(4), 533-540.
8. Lofrano, G., Carotenuto, M., Libralato, G., Domingos, R. F., Markus, A., Dini, L. & Chattopadhyaya, M. C. (2016). Polymer functionalized nanocomposites for metals removal from water and wastewater: an overview. *Water research*, 92, 22-37.
9. Lee, J., Lee, Y., Youn, J. K., Na, H. B., Yu, T., Kim, H. & Chang, H. N. (2008). Simple synthesis of functionalized superparamagnetic magnetite/silica core/shell nanoparticles and their application as magnetically separable high-performance biocatalysts. *Small*, 4(1), 143-152.
10. El-Kassas, H. Y., Aly-Eldeen, M. A., & Gharib, S. M. (2016). Green synthesis of iron oxide (Fe₃O₄) nanoparticles using two selected brown seaweeds: characterization and application for lead bioremediation. *Acta Oceanologica Sinica*, 35(8), 89-98.
11. Lattuada, M., & Hatton, T. A. (2007). Functionalization of monodisperse magnetic nanoparticles. *Langmuir*, 23(4), 2158-2168.
12. Ghasemi, E., Heydari, A., & Sillanpää, M. (2017). Superparamagnetic Fe₃O₄@EDTA nanoparticles as an efficient adsorbent for simultaneous removal of Ag (I), Hg (II), Mn (II), Zn (II), Pb (II) and Cd (II) from water and soil environmental samples. *Microchemical Journal*, 131, 51-56.
13. Azdiya Suhada, Ismayadi,(2017) Magnetite Nanoparticles in Wastewater Treatment Pertanika *Journal of Scholarly Research Reviews PJSRR* 2(3): 108-122.
14. Ravichandran, M., Velumani, S., & Ramirez, J. T. (2017). Water-dispersible magnetite nanoparticles as T₂ MR imaging contrast agent. *Biomedical Physics & Engineering Express*, 3(1), 015011.

3.5 Structural and magnetic behavior of Yttrium Iron Garnet ($Y_3Fe_5O_{12}$) nanoparticles

Raba'ah Syahidah Azis, Nuraine Mohd Shahrani, Jumiah Hassan and Zulkifly Abbas

Abstract

The structural and magnetic properties of nanostructured yttrium iron garnet ($Y_3Fe_5O_{12}$, YIG) were presented in this paper. The starting powder of α - Fe_2O_3 and Y_2O_3 were synthesized by employing the high-energy ball milling (HEBM) technique for 9 hours using a SPEX8000D mill. The samples were sintered from 700, 800 and 900 °C. Structural, phase analysis and particle size were carried out by using X-ray Diffractometer (XRD) and transmission electron microscopy (TEM). Magnetic permeability was characterized using an impedance analyzer. Magnetization hysteresis curve parameters were observed from a vibrating sample magnetometer (VSM). At low sintering temperature < 900°C, the XRD show the confirmation of the development of YIG phase along with secondary phase yttrium iron perovskite ($YFeO_3$, YIP). As increase the sintering temperature, the XRD peak much sharper as an improvement of the crystallinity. The saturation magnetization M_s increased as temperature increase. The coercivity H_c appeared to be influenced by the microstructure which developed from single-domain to multi-domain. The M_s showed the decrement value for samples sintering at 700°C to 800°C. These results can be associated with the formation of weak ferromagnetic behavior of α - Fe_2O_3 and $YFeO_3$ phases. H_c showed the critical size of single-domain to multi-domain at 800 °C. The maximum values of H_c and M_s are 71 Gs (700 °C) and 126 emu/g (900 °C) respectively.

Keywords: $Y_3Fe_5O_{12}$ (YIG), XRD, FTIR, VSM, FESEM

Introduction

Ferrites gas much attention nowadays due to its application in microwave applications, switches, circulator, antenna and their potential use as one of the electromagnetic wave absorber. The penetration of electromagnetic (EM) waves is possible in ferrites because of their non-conducting nature [1]. The study of yttrium iron garnet (YIG) is becoming more important because of properties that can be extensively used in optical communication, magneto-optical devices and in microwave [2]. The recent progress in synthesis techniques of highly crystalline yttrium iron garnet (YIG), $Y_3Fe_5O_{12}$ are the study on the structure-properties evolution in YIG.

Yttrium iron garnet (YIG) with the chemical of $3Y_2O_3 \cdot 5Fe_2O_3$ ($Y_3Fe_5O_{12}$) has a garnet system. YIG is formed by heating a combination of a mixture of Y_2O_3 and Fe_2O_3 giving Fe and Y to the ratio of 5:3 (Fe:Y) [3]. The ferrimagnetic behavior possessed by YIG garnet ferrite is used for many applications in magnetic and magneto-optical devices. The magnetic garnet, the metal ions (Fe^{3+} and Y^{3+}) are all trivalent. There are 24 dodecahedral site, 16 octahedral site, and 24 tetrahedral sites in a unit cell containing 8 formula units. Garnets structure system provide superior performance in microwave devices because they produce narrow resonance line width, that is one of the most important parameters for microwave application, besides wide range of magnetization and very low dielectric loss [4].

Nowadays, there are there are much attention to researchers to report the synthesis and characterization on YIG nanoparticles. There is less study on the YIG nanoparticles sintered at relatively lower temperatures (below 900 °C) are reported. Therefore, in this work, the

structural-magnetic properties relationship at low sintering temperatures (<900°C) on the YIG nanoparticles properties will be investigate.

Methodology

The raw materials used in this study were yttrium oxide (Y_2O_3) powder (99.9 %, Alfa Aesar) and Fe_2O_3 powder. The raw powder were weighed and mixed using an agate mortar for about one hour. The agate mixing powder then was milled high energy ball mill (HEBM) with the ratio of powder to ball is 10:1 for 9 hours. High energy ball milling was carried out at room temperature equipped with hardened steel vials and steel balls. The size ball mill was used with ball media of sizes 10 mm and 20 mm, respectively. The milling process is important as to ensure the solid state reaction occurred at an optimum level. After milling, 1 weight % polyvinyl alcohol (PVA) with was added in the powder as a binder and then 0.3 weight % of zinc stearate lubricated were added. The mixture is dried, granulated and ground in a mortar and pressed at 300 MPa to obtain 0.35 g of pellet and 2.5 g of toroid shape samples. The compact samples were then sintered at 700,800 and 900°C. The sintered samples then characterize its structural, particle size and magnetic properties by using XRD, TEM, Impedance analyzer and VSM respectively.

Results and Discussion

Figure 1 shows the XRD spectra of the YIG nanoparticles prepared by HEBM method. At sintering temperature at 700°C and 800°C, the XRD spectra shows a trace of diffraction peaks of formation of YIG, along with the impurities of yttrium iron perovskite structure ($YFeO_3$, YIP) as matched to ICDD 98-004-86, wuth orthoferrite), along with impurity raw material Fe_2O_3 and Y_2O_3 phases, as indexed to ICDD reference code of 98-000-6274 and 98-000-8030 respectively. This suggests that the minimum temperature needed to obtain single phase is not reached for pure YIG [4]. For the powder heated at 900 °C, it can be observed that Fe_2O_3 and Y_2O_3 disappear; however garnet phase becomes the major phase and less orthoferrite phase still remains. The XRD pattern at the powder sintered at 1000°C shows clear peaks matched with the cubic YIG phases (ICDD 98-003-5954). The presence of the complete YIG phase can be indexed to (321), (420), (422), (521), (611), (444), (640), (642), (741), (840), (842), and (664) planes of a cubic unit cell. This indicated that the sintering temperature at < 900°C can assist in obtaining YIG phase prepared by mechanical alloying method. The YIG phase is appeared at low temperature as 700°C. HEBM method is useful to promote the the formation of nanostructure ferrite by mechanical activation of oxide compound. The particle size of mechanically alloyed sample shows the average of particle size around 57 nm. The particle size distribution is varying in homogenously from 45 nm, and showed the most tabulated particle size around 50 nm (TEM) (Figure 2).

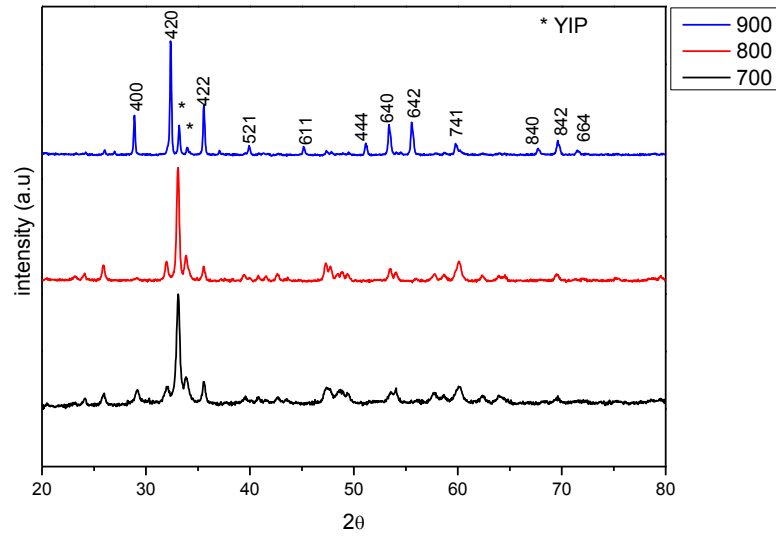


Figure 1: X-ray diffraction spectra of YIG sintered at varied temperatures.

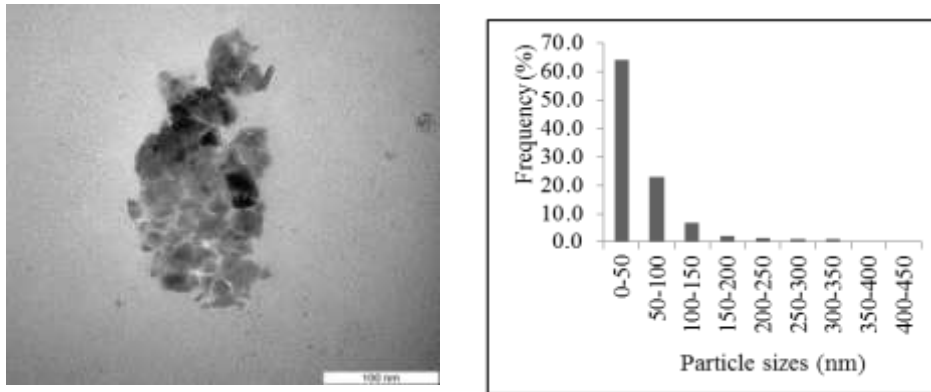


Figure 2: (left) TEM micrograph and (right) particle size distribution graph.

The hysteresis loop of magnetization (M) and applied external magnetic field (H) is shown in Figure 3. The saturation magnetization reached 0.26 emu/g and 0.069 emu/g at 700°C and 800°C respectively. These values could be related to the presence of weak ferromagnetic behavior of α -Fe₂O₃ and YFeO₃ and a significant amount of amorphous phase. Moreover, such trend also can be associates with the mixture of disordered and ordered magnetism. The samples sintered from 700 to 800°C contained only weak magnetic phase as the magnetization at this range temperature are almost zero. In addition, the smaller value of saturation magnetization in smaller grain size at this region temperature is attributed to the fine greater fraction of surface spins in the particles that tends to be in a canted with a smaller net moment. The samples sintered at 700°C to 800°C show a decreasing value of magnetization. This is due to the formation of a large volume fraction of the weak ferromagnetic magnetic oxides and the surface effects. At 700°C and 800°C, orthoferrites and hematite shows the weak ferromagnetic behavior. The weak ferromagnetism arises from the low symmetry of the magnetic unit cell, producing a spin-canted structure of Fe sub lattices. The weak ferromagnetic behavior of α -Fe₂O₃ is due to a slight disorder of the spin axis from exact anti parallelism. The H_c values were observed decreasing as the temperatures. The magnetically ordered spectrum of YIP reflect the octahedral environment of high-spin Fe(III) in the

perovskite structure, while two nonequivalent octahedral and tetrahedral Fe(III) positions were identified in the YIG garnet spectrum [4].

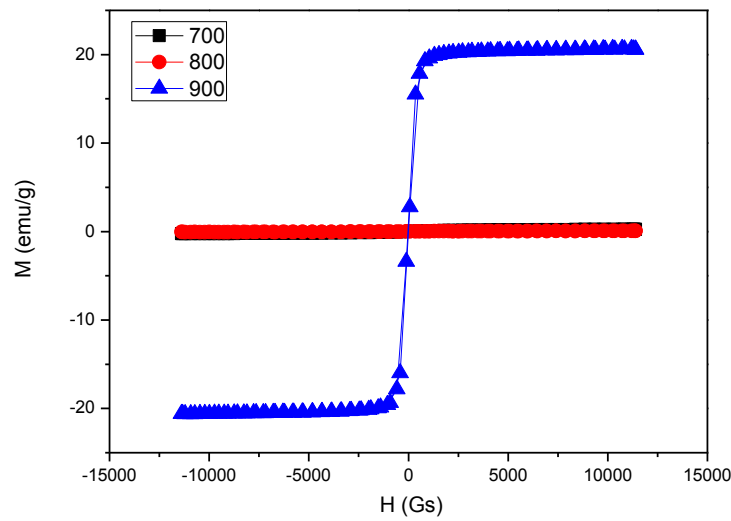


Figure 2: M - H hysteresis loop of YIG samples at various sintering temperatures.

The real permeability of samples increased with the increase of temperature (Figure 3), that attributed to the increase in particle sizes. The increased of μ' value with increasing of sintering temperature is attributed to the increase of grain sizes, where larger grains diminish the number of grain boundaries [3]. The real permeability is small at temperature 700°C and 800°C, due to the interfering of small grains with wall motion. The larger the particle size, increase the number of domain wall and increase the permeability of the YIG nanostructure. Permeability spectra decreases with increasing the frequency and its values are larger at low frequencies. On the other hand the permeability of sample remains steady up to 1 MHz. Also there are different frequency dependences of the imaginary parts of permeability and loss factor, respectively. The HEBM of the amorphous YIG positively influences on the AC magnetic properties at higher frequencies (above 100 Hz) of bulk sample.

For sintered YIG, a peaks corresponding to the domain wall and the gyromagnetic spin resonance were observed in the imaginary part μ_r'' under zero magnetic field; the real part of complex permeability μ_r' shows a small negative value in a certain frequency range. The Lorentz type magnetic resonance with the negative permeability dispersion was observed under dc magnetic field. Permeability spectra were evaluated by the numerical fitting of actual measurement data to a resonance formula using six parameters (resonance frequencies, static susceptibilities, and damping factors of the domain wall motion and the gyromagnetic spin rotation). The dc magnetic field suppresses the domain wall contribution and the spin component becomes dominant. In the YIG granular composite material, the permeability dispersion frequency shifts to higher frequency region due to demagnetizing field; the spin component becomes dominant. Negative permeability spectra were also observed in the high content YIG composites under the dc field. The negative permeability spectra of YIG composite materials can also be applied to the left-handed material as well as the sintered YIG.

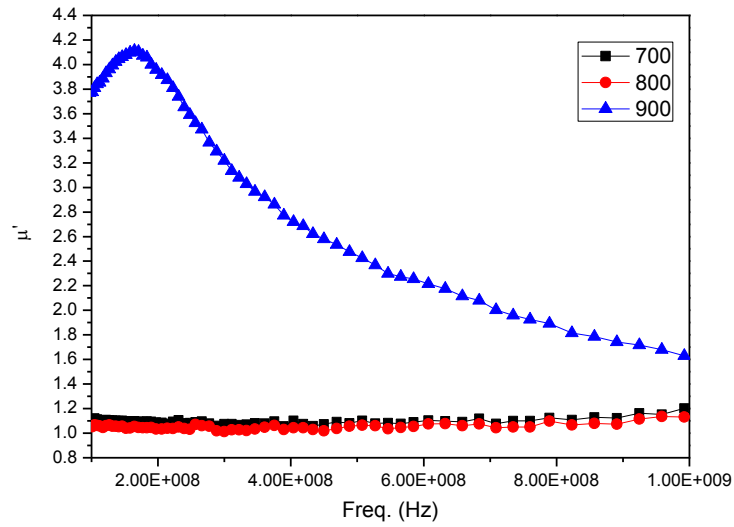


Figure 3: Real permeability of YIG samples at various sintering temperatures.

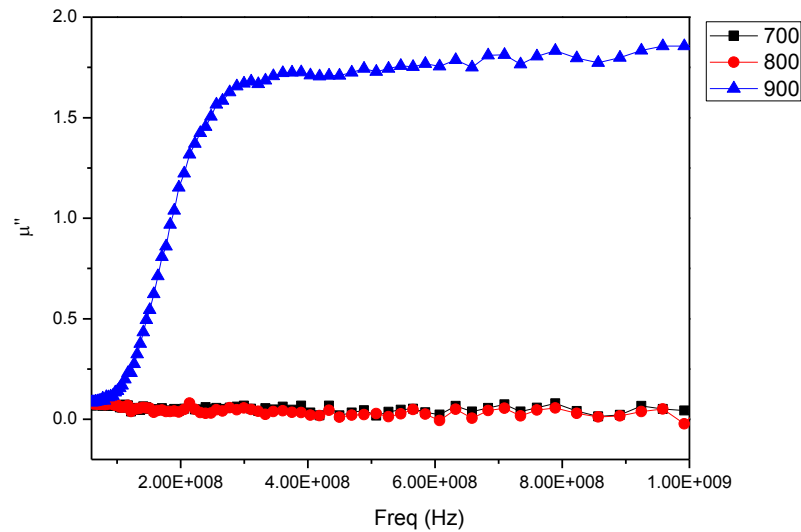


Figure 4: Imaginary permeability of YIG samples at various sintering temperatures.

Conclusion

The YIG nanostructure was successfully synthesized and optimized. The effect of sintering temperature and the formation of YIG nanostructure on the structural, particle size and magnetic properties were studied. The single-phase of crystallized samples and the well-defined structure of YIG nanoparticles were confirmed by XRD spectra excluding the presence of any other phases in the reaction products. YIG ferrite is special, is a material that resonates at microwave frequencies when immersed in a DC magnetic field. The YIG nanostructure is useful for miniature magnetic sensor, electromagnetic interference suppression (EMI), EM wave absorbers, and sensors applications.

Acknowledgement

The authors would like to thanks to Research University Grant, Universiti Putra Malaysia (UPM) for the financial support (Vot. No. 9539100 and 9542700).

References

1. Vinay Sharma, Jitendra Saha, Satyabrata Patnaik, and Bijoy K. Kuanr, "Synthesis and characterization of yttrium iron garnet (YIG) nanoparticles - Microwave material", *AIP Advances* 7, 056405 (2017), pp 1-6.
2. Makiyyu Abdullahi Musa, Raba'ah Syahidah Azis, Nurul Huda Osman, Jumiah Hassan and Mustafa Mousa Dihom, "Structural and magnetic properties of yttrium aluminum iron garnet (YAlG) nanoferrite prepared via auto-combustion sol-gel synthesis", *Journal of Australian Ceramic Society* (2017), pp 1-9.
3. Nuraine Mariana Mohd Shahrana, Raba'ah Syahidah Azis, Mansor Hashim, Jumiah Hassan, Azmi Zakaria and Noruzaman Daud, "Effect of Variation Sintering Temperature on Magnetic Permeability and Grain Sizes of $Y_3Fe_5O_{12}$ via Mechanical Alloying Technique", *Materials Science Forum* (2015), 846, pp 395-402
4. Soleimani, H., Abbas, Z., Yahya, N., Shameli, K., Soleimani, H., & Shabanzadeh, P. (2012). Reflection and transmission coefficient of Yttrium iron garnet filled polyvinylidene fluoride composite using rectangular waveguide at microwave frequencies. *International Journal of Molecular Sciences*, 13(7), pp 8540–8548.
5. Makiyyu Abdullahi Musa, Raba'ah Syahidah Azis, Nurul Huda Osman, Jumiah Hassana and Tasiu Zangina, "Structural and magnetic properties of yttrium iron garnet (YIG) and yttrium aluminum iron garnet (YAlG) nanoferrite via sol-gel synthesis", *Results in Physics* (2017), pp 1135-1142.
6. Jiri Pinkas, Vendula Reichlova, Aneta Serafimidisova, Zdenek Moravec, Radek Zboril, Dalibor Jancik and Petr Bezdicka, "Sonochemical Synthesis of Amorphous Yttrium Iron Oxides Embedded in Acetate Matrix and their Controlled Thermal Crystallization toward Garnet ($Y_3Fe_5O_{12}$) and Perovskite ($YFeO_3$) Nanostructures", *J. Phys. Chem. C* (2010), 114 (32), pp 13557–13564.

CHAPTER 4

SUPERCONDUCTORS AND APPLICATIONS

4.1 Development of Bi-2212 via Thermal Treatment Method Using PVP as Capping Agent

Safia Izzati Abd Sukor, Mohd Mustafa Awang Kechik, Abdul Halim Shaari, Chen Soo Kien, Hussein Baqiah

Abstract

This work shows the progress of synthesizing $\text{Bi}_2\text{Sr}_2\text{CaCu}_2\text{O}_\delta$ via thermal treatment method. Nitric acid, deionized water, PVP and metal nitrate (Bi, Sr, Ca and Cu) were used as starting materials. Various volume of nitric acid was added to ensure the bismuth nitrate is dissolved in the deionized water as one of the properties of bismuth is not dissolved in water. PVP is used to ensure the stabilization of particles and to prevent agglomeration. The samples were characterized using X-ray Diffraction (XRD), Scanning Electron Microscope (SEM) and the Four Point Probe. The optimum volume of nitric acid was found to be 15 ml. The crystal structure of all sample are orthorhombic where $a \neq b \neq c$. Changes in the crystal structure were discussed.

Keywords: Bismuth-Strontium-Calcium-Copper-Oxide, BSCCO, Thermal treatment, Nitric acid, Critical temperature (T_c)

Introduction

Since the discovery of superconductivity in Bi-Sr-Ca-Cu-O (BSCCO) compounds by Raveau's [1] and Maeda et al.'s work [2], extensive studied were focused toward development of synthetic procedures which leads to single phase ceramics and well defined superconducting transition temperature (T_c). BSCCO still obtain a high T_c values even though it is in absence of rare earth metal. BSCCO with chemical formula of $\text{Bi}_2\text{Sr}_2\text{Ca}_{n-1}\text{Cu}_n\text{O}_{2n+4+\delta}$ have three phases which are when $n=1$ (Bi-2201), $n=2$ (Bi-2212) and $n=3$ (Bi-2223) with T_c values of 10K, 90K and 110K respectively.

Various synthesizing method of BSCCO has been reported, such as solid state [3], polymer method [4], sol gel [5], attrition milling [6] and etc aiming to improve the superconducting properties. In recent study, superconductor was prepared from an aqueous solution containing metal nitrates, deionized water and polymer as capping agent [7-9]. This method is advantageous because it is low cost, simple and can be used to achieved fine powder [10-13].

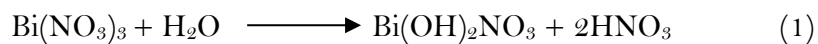
In this work we are discussing a development of synthesizing Bi-2212 using a thermal treatment method on the structural and the superconducting properties. The differences in volume of nitric acid were studied.

Materials and method

Bi-2212 powders were prepared by using thermal treatment method. Bismuth nitrate $\text{Bi}(\text{NO}_3)_3$, strontium nitrate $\text{Sr}(\text{NO}_3)_2$, calcium nitrate tetrahydrate $\text{Ca}(\text{NO}_3)_2 \cdot 4\text{H}_2\text{O}$, and copper nitrate hemi pentahydrate $\text{Cu}(\text{NO}_3)_2 \cdot 2.5\text{H}_2\text{O}$ and polyvinyl pyrrolidone (PVP) were used as the starting materials. All metal nitrates were weighted according to their stoichiometric amount and later were mix and dissolved in 300 ml deionized water with continuous stirring at 80 °C except for the bismuth nitrate. Bismuth nitrate was first diluted with nitric acid (0 ml, 10 ml, 15 ml and 30 ml) before was added to the precursor solution. The precursor solution was kept stirring for 2 hours as the PVP was added to the solution. PVP acted as capping agent. The precursor then was dried out in oven at 90 °C for 24 hours to evaporate the water. Light green flaky solid was crushed using mortar and pestle until fine powder was obtain and then pre-calcined at 600°C for 4 hours. The powder was calcined at 800 °C for 24 hours and pressed into pellet with intermediate ground. The sintering of the pellet was conducted at 840 °C for 24 hours. The crystal structure and the phase formation of Bi-2212 were characterized by using X-ray Diffraction (XRD) (Xpert Pro Panalytical Philips DY 1861) in scanning range of $2\theta=20^\circ$ - 80° . The structural studies and morphological were conducted using the Scanning Electron Microscope (SEM) while the critical temperature was measured using standard four-point probe method.

Results and discussion

During the preparation method the sample with 0 ml and 10 ml of nitric acid was discarded from the experiment due to the white precipitate that was observed during the stirring process where we expected that the white precipitate is bismuth sub-nitrate where can be explain in the chemical reaction stated below



Formation of BSCCO is proposed in Figure 1, where the interaction between Bi, Sr, Ca, Cu ions and PVP happen during the stirring process. The interaction between metallic ions and the amide group in polymer chain were bound by strong ionic bond, causes the metallic ions to immobilized which favors in controlling the nucleation of Bi-2212 particles. During the drying process PVP trap all the metal ions in polymer scaffold as water was removed from the mixture. Later during the calcination the PVP and unwanted ions were removed and the Bi-2212 particles were gradually grown. [7-13]

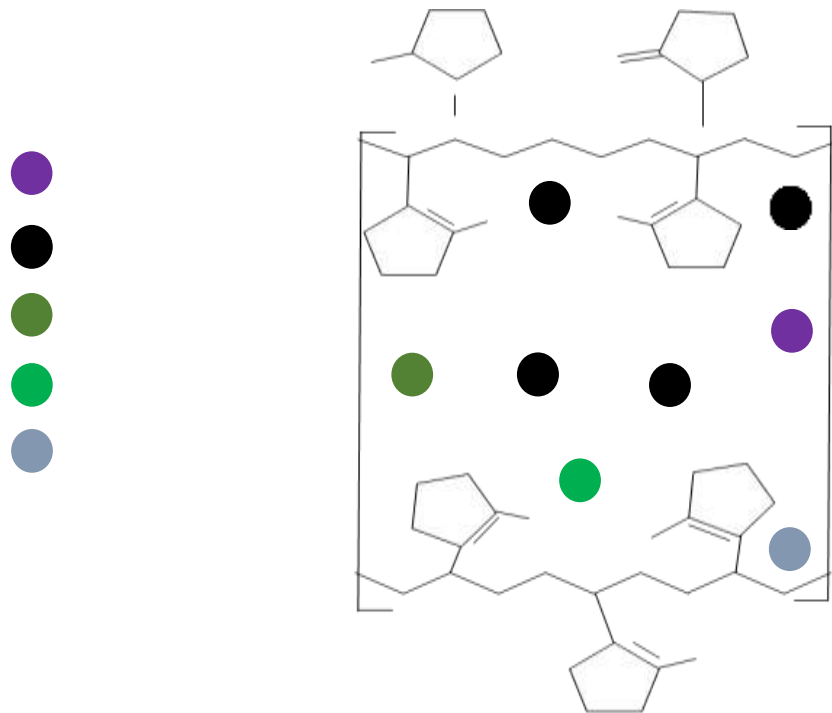


Figure 1 Proposed mechanism of interaction between metal ions and PVP

Figure 2 shows the XRD pattern for Bi-2212 with nitric acid of 15 ml and 30 ml. The pattern shows major phases that we obtain are Bi-2212 and Bi-2201. The volume fraction of the Bi-2212 and Bi-2201 was calculated from the expression shown below

$$\text{Bi} - 2212 (\%) = \frac{\Sigma I_{2212}}{\Sigma I_{2212} + \Sigma I_{2201}} \times 100\%$$

$$\text{Bi} - 2201 (\%) = \frac{\Sigma I_{2201}}{\Sigma I_{2212} + \Sigma I_{2201}} \times 100\%$$

Table 1 shows the volume fraction of Bi-2212 and Bi-2201. The difference in volume of nitric acid does not give a significant difference in the phase fraction. The crystal structure for both BSCCO sample is orthorhombic as $a \neq b \neq c$.

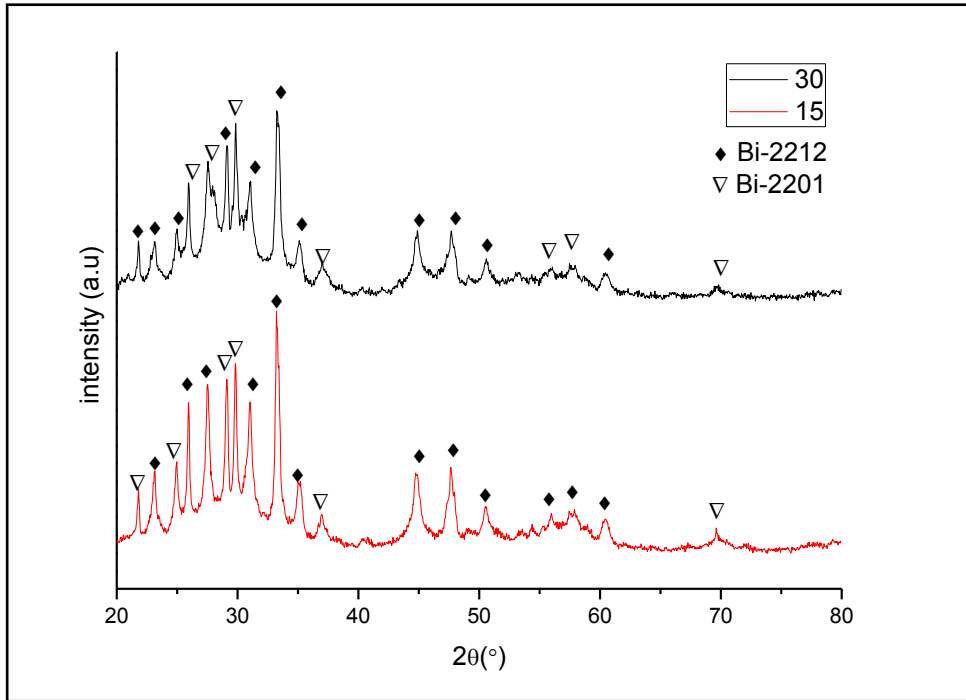


Figure 2 XRD pattern of BSCCO sample with 15 ml and 30 ml nitric acid

Table 1 Relative volume fraction of BSCCO sample

Volume of nitric acid (ml)	Phase fraction	
	Bi-2212	Bi-2201
15	30.5	69.5
30	30.8	69.2

The electrical resistivity was conducted using the standard four point-probe instrument. Figure 3 shows normalized resistance versus temperature measured at temperature 30 K to 300 K. Samples show a metallic behavior at the normal state above the transition temperature. The critical temperatures of the samples are shown in Table 2. Sample with 30 ml exhibit higher T_c compared to the sample with 15ml nitric acid.

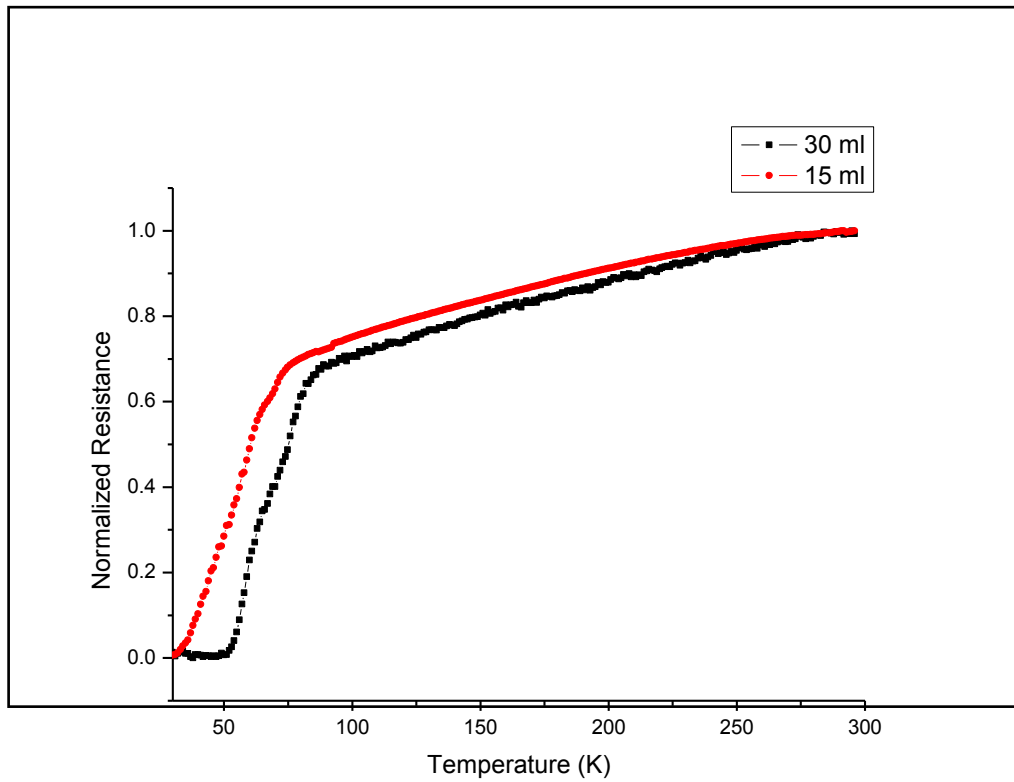


Figure 3 Normalized resistances versus temperature

Table 2 Critical temperature for sample with 15 ml and 30 ml nitric acid

Volume of nitric acid (ml)	Critical temperature (K)		
	$T_{c\ onset}$	$T_{c\ offset}$	ΔT_c
15	65	31	34
30	82	56	26

The surface morphology that we obtain from SEM is shown in Figure 4 (a) 15ml and (b) 30ml. The SEM morphology shows platelet like grain morphology which that is exhibited by BSCCO system. Sample with 30 ml nitric acid shows more random orientated grain that that with 15 ml, while sample with 15 ml shows more pores between the grains than that with sample with 30 ml nitric acid.

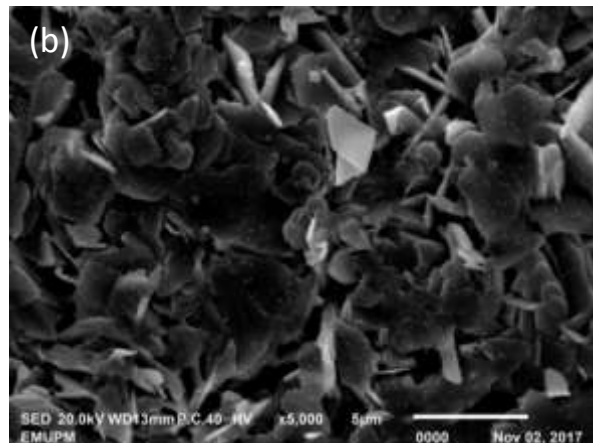
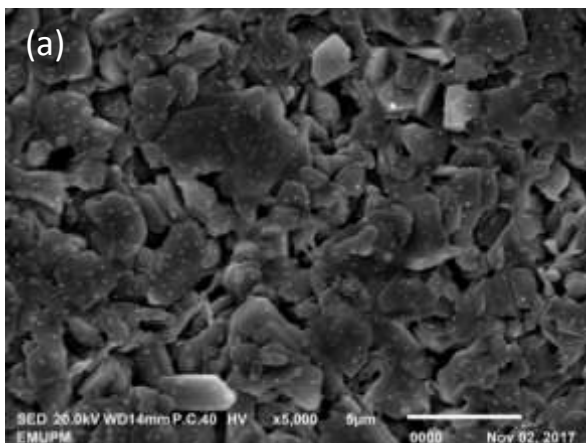


Figure 4 SEM morphology (a) 15 ml (b) 30 ml nitric acid BSCCO sample.

Conclusion

The development of Bi-2212 via thermal treatment method using PVP as capping agent has been studied. Bi-2212 was successfully prepared by using thermal treatment method. The superconducting properties of Bi-2212 with 30 ml nitric acid shows a slightly higher T_c compared to the 15ml which is 56K.

Acknowledgement

This project was supported Ministry of Education Malaysia (MOE) for Fundamental Research Grant Scheme (FRGS 5524921) and Universiti Putra Malaysia

References

1. Michel, C., Hervieu, M., Borel, M. M., Grandin, A., Deslandes, F., Provost, J., & Raveau, B. (1987). Superconductivity in the Bi-Sr-Cu-O system. *Zeitschrift für Physik B Condensed Matter*, 68(4), 421-423.
2. Maeda, H., Tanaka, Y., Fukutomi, M., & Asano, T. (1988). A new high- T_c oxide superconductor without a rare earth element. *Japanese Journal of Applied Physics*, 27(2A), L209.
3. Suazlina, M. A., Yusainee, S. Y. S., Azhan, H., Abd-Shukor, R., & Mustaqim, R. M. (2014). The effects of nanoparticle addition in Bi-2212 superconductors. *Jurnal Teknologi (Sciences and Engineering)*, 69(2), 49-52.
4. Gürsul, M., Ekicibil, A., Özçelik, B., Madre, M. A., & Sotelo, A. (2015). Sintering effects in Na-substituted Bi-(2212) superconductor prepared by a polymer method. *Journal of Superconductivity and Novel Magnetism*, 28(7), 1913-1924.
5. Garnier, V., Caillard, R., Sotelo, A., & Desgardin, G. (1999). Relationship among synthesis, microstructure and properties in sinter-forged Bi-2212 ceramics. *Physica C: Superconductivity*, 319(3), 197-208.
6. Patel, R. H., Nabialek, A., & Niewczas, M. (2005). Characterization of superconducting properties of BSCCO powder prepared by attrition milling. *Superconductor Science and Technology*, 18(3), 317.
7. Dihom, M. M., Shaari, A. H., Baqiah, H., Al-Hada, N. M., Kien, C. S., Azis, R. S., & Abd-Shukor, R. (2017). Microstructure and superconducting properties of Ca substituted Y ($Ba_{1-x}Ca_x$)₂Cu₃O_{7- δ} ceramics prepared by thermal treatment method. *Results in Physics*, 7, 407-412.
8. Zahari, R. M., Shaari, A. H., Abbas, Z., Baqiah, H., Chen, S. K., Lim, K. P., & Kechik, M. A. (2017). Simple preparation and characterization of bismuth ferrites nanoparticles by thermal treatment method. *Journal of Materials Science: Materials in Electronics*, 1-7.
9. Naseri, M. G., Saion, E., & Zadeh, N. K. (2013). The amazing effects and role of PVP on the

crystallinity, phase composition and morphology of nickel ferrite nanoparticles prepared by thermal treatment method. *International Nano Letters*, 3(1), 19.

10. Dihom, M. M., Shaari, A. H., Baqiah, H., Al-Hada, N. M., Talib, Z. A., Kien, C. S., Azis, R.S., Kechik, M.M.A., Pah, L.K., & Abd-Shukor, R. (2017). Structural and superconducting properties of $Y (Ba_{1-x} K_x)_2 Cu_3 O_{7-\delta}$ ceramics. *Ceramics International*.

11. Dihom, M. M., Shaari, A. H., Baqiah, H., Al-Hada, N. M., Chen, S. K., Azis, R. A. S., Azis, R.S., Kechik, M.M.A., Pah, L.K., & Abd-Shukor, R. (2017). Effects of Calcination Temperature on Microstructure and Superconducting Properties of Y123 Ceramic Prepared Using Thermal Treatment Method. In *Solid State Phenomena* (Vol. 268, pp. 325-329). Trans Tech Publications.

12. Naseri, M. G., Saion, E., & Zadeh, N. K. (2013). The amazing effects and role of PVP on the crystallinity, phase composition and morphology of nickel ferrite nanoparticles prepared by thermal treatment method. *International Nano Letters*, 3(1), 19.

13. Naseri, M. G., Saion, E. B., Hashim, M., Shaari, A. H., & Ahangar, H. A. (2011). Synthesis and characterization of zinc ferrite nanoparticles by a thermal treatment method. *Solid State Communications*, 151(14), 1031-1035.

4.2 The comparative studies of YBCO prepared by co-precipitation and thermal treatment Methods

Nur Nabilah Mohd. Yusuf, Mohd Mustafa Arwang Kechik, Abdul Halim Shaari, Chen Soo Kien and Hussein Baqiah

Abstract

YBCO has been long known as one of the promising superconducting material to be applied in the electrical industry due to its ability to withstand high magnetic field at higher temperature without losing its properties. In this study, YBCO bulk superconductor was synthesised via thermal treatment and co-precipitation methods. A SEM images show that thermal treatment method yields larger grain size sample compared to co-precipitation method. The microstructure in thermal treatment is also packed and denser compared to the other. However, there is no significant difference in the percentage of pure Y-123 obtained. The results obtained from four- point probe shows that thermal treatment method has smaller temperature transition with T_c closer to the theoretical 92 K.

Introduction

The properties of cuprate oxide superconductors depend strongly on the techniques and processing conditions used to synthesis the bulk sample. Unlike the conventional solid state method, wet methods are proven to yield better results in terms of homogeneity and better control of stoichiometry since the materials and reactions can be chemically controlled to obtain the desired product (Hamadneh et al., 2006). Co-precipitation method (COP) and thermal treatment method (TT) are two of the wet methods used in this study. The difference in both methods lies in the synthesis of the precursor powder. In general, co-precipitation method is the separation of solid containing a variety of ionic groups which are chemically bounded to each other from a liquid or a solution (Schildermans et al., 1999). The separation of solid is aided by a precipitating agent to allow the precipitation process and then filtered to collect the precipitate. This precipitate when dried and ground became the precursor powder. On the other hand, thermal treatment mixes a specific ratio of starting material with a capping agent in water under certain temperature to bind the ions together (Dihom et al., 2017). It later requires only heat treatment process to obtain the precursor powder through evaporation.

Some of the known routes for co-precipitation method are hydroxide, carbonate and oxalate routes referring to the precipitating agent and starting material source obtained respectively (Shter & Grader, 1993). The one used in this study is the oxalate routes. In an oxalate system, oxalic acid or oxalate salt is used as the precipitating agent. The technique however, varies according to the starting material i.e. metal source, owing to the fact that different materials have different solubility constant, K_{sp} (Skirius et al., 1994). The difference in K_{sp} while mixing the solutions will result in different stoichiometry of end product. This is because materials with higher solubility might end up in the filtrate instead of the precipitate, altering the precursor's stoichiometry obtained (Keiji Kaneko, Hideo Ihara, asayuki Hirabasyi, Norio Terada, 1987). To overcome this problem, pH of the solutions during the whole process is crucial and must be taken into account as it affects strongly on the solubility (Bhargava, Mackinnon, Yamashita, & Page, 1995; Chen et al., 1994). In many studies, ice bath and pH-

adjusting agent were used to control the pH and solubility of these materials (Bhargava et al., 1995; Hamadneh, Agil, Yahya, & Halim, 2007).

Meanwhile, thermal treatment is quite lenient when it comes to the pH of the solution during the synthesis as long as the starting material can be dissolved in water. This is due to the unlikely event at which the composition of the starting materials to change as the evaporation of water took place. During the whole process, thermal treatment is aided by evaporation and combustion process to eliminate the by-product (Dihom et al., 2017; Gene, Saion, Shaari, Kamarudeen, & Al-Hada, 2015). Thereby, the capping agent use is usually polymer based such as PAAc, Poly(vinyl alcohol) (PVA) and Polyvinylpyrrolidone (PVP) due to its ability to act as thickening agents for HTSC precursors solutions, composites or even complexing agents for metal ions to produce shape able HTSC (Dubinsky, Lumelsky, Grader, Shter, & Silverstein, 2005). An added advantage is that its complete elimination is ensured when subjected to heat during calcination process as they are easy to decompose at low temperature. In this study, YBCO bulk superconductor were synthesised via thermal treatment and co-precipitation method. The obtained samples from both methods were comparatively studied using X-rays diffraction (XRD), Field emission scanning electron microscope and four point probe measurement.

Experimental

The $\text{YBa}_2\text{Cu}_3\text{O}_7$ bulk samples had been synthesised using the two methods mentioned. Acetate and nitrate based metal salts of YBCO were weighed to the ratio of 1:2:3 for co-precipitation (COP) and thermal treatment (TT) method respectively.

Co-precipitation

The co-precipitation method was done by following the experimental details in (Hamadneh et al., 2006) (Ramli et al., 2016). Solution A was prepared by dissolving yttrium acetate ($\text{Y}(\text{CH}_3\text{COO})_3 \cdot 4\text{H}_2\text{O}$), barium acetate ($\text{Ba}(\text{CH}_3\text{COO})_2$) and copper(II) acetate ($\text{Cu}(\text{CH}_3\text{COO})_2$) with purity >99%, in acetic acid. Meanwhile, solution B was prepared by mixing 2:3 ratios of deionised water: isopropanol with 0.5mol/L oxalic acid. Both solutions were stirred for 2hrs before continuing the stirring in an ice bath respectively for 15 minutes. Then, solution B is added drop wise in solution A while maintaining the speed of stirring at 300rpm. Slurry blue suspension was formed and let stirred until homogeneous. This blue solution was then filtered using filter paper and butchner funnel. The precipitate obtained was dried overnight and ground to obtain the precursor which was calcined at 900°C for 15hrs twice with intermediate grinding. The powder was then reground, pellet and sintered at 940°C for 24hrs.

Thermal treatment

As for the thermal treatment method, this study followed the synthesis of Y123 in (Dihom et al., 2017). 1:2:3 ratio of $\text{Y}(\text{NO}_3)_3 \cdot 6\text{H}_2\text{O}$, $\text{Ba}(\text{NO}_3)_2$, $\text{Cu}(\text{NO}_3)_2 \cdot 2.5\text{H}_2\text{O}$ and $\text{Ca}(\text{NO}_3)_2 \cdot 4\text{H}_2\text{O}$ were stirred for 2hrs together with 2% aqueous solution of 300 ml of polyvinyl pyrrolidone (PVP) at 80°C. It was then let evaporated at 110°C for 24hrs forming solid like green gel. The gel was ground into fine powder and calcined at 600°C for 4hrs and 910°C for 24hrs with

intermediate grinding. Sintering was done at 980 °C for 24hrs after the powder was reground and pellet.

Results and discussion

Figure 1 and 2 indicates the thermal decomposition of YBCO precursor for both COP and TT method. The TGA and DTG graph shows the mass loss and its derivative mass loss when subjected to a certain temperature. The COP TGA/DTG graph in figure 1 shows five prominent drops in which the first and second drop in between 25 °C to 240 °C are attributed to the dehydration of moisture and water in the oxalate lattice (Ramli, 2016). The most significant drop with the most percentage of mass loss was at 286 °C due to the decomposition of yttrium and copper oxalate into oxides corresponding to the carbonates (Petropoulou et al., 2002). The decomposition of barium oxalate was claimed to start in the fourth drop and completely decomposed at the final drop in between 800 °C to 900 °C (Ramli, 2016).

The peaks showed in thermal treatment precursor powder was not as prominent in COP. While the first drop are always related to the moisture dehydration (Khalid, 2016), the next few drops between 146 °C up to 498 °C are related to the dehydration and denitration of yttrium and copper nitrate (Patta et al., 2009). Barium nitrate was said to decompose at temperature 590 °C which can be related to the sharpest drop (Patnaik, 2003). The last drop could be due to decomposition of BaCO₃ and the formation of BaO (Dubinsky et al., 2005).

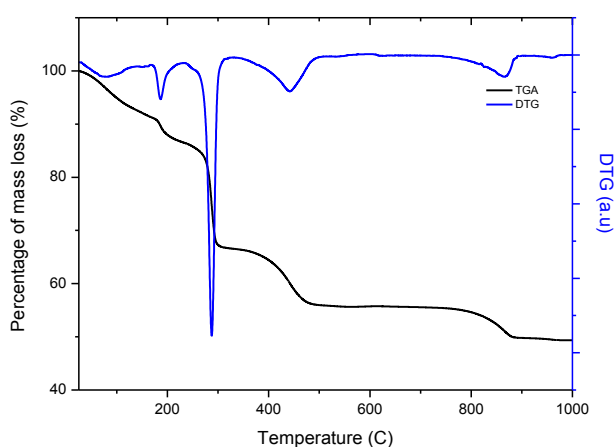


Figure 1: TGA/DTG graph for COP precursor powder.

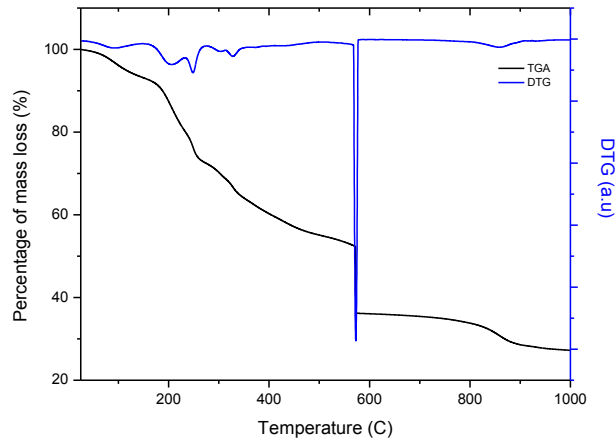


Figure 2: TGA/DTG graph for TT precursor powder.

The resistance versus temperature curve for both pure Y123 samples prepared by COP and TT method is shown in Figure 1. Both R-T curves showed a metallic behaviour during the normal state. COP sample shows $T_{C-onset}$ at 90K and $T_{C-offset}$ at 83 K while TT sample shows $T_{C-onset}$ at 92 K and 87K for $T_{C-offset}$. The difference in both T_C gives the transition temperature, ΔT of 7 K and 5 K in COP and TT respectively. Although the differences are not much, it shows that TT method gives better quality sample as it gives slightly higher T_C with sharper transition temperature, ΔT .

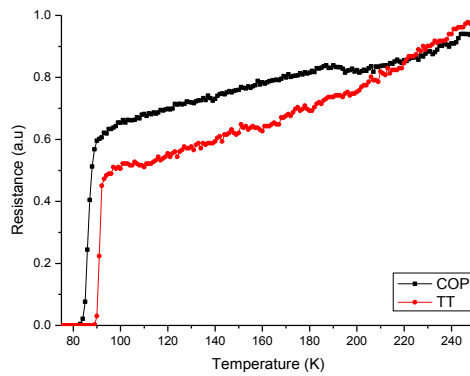


Figure 3: The resistance versus temperature graph for COP and TT samples.

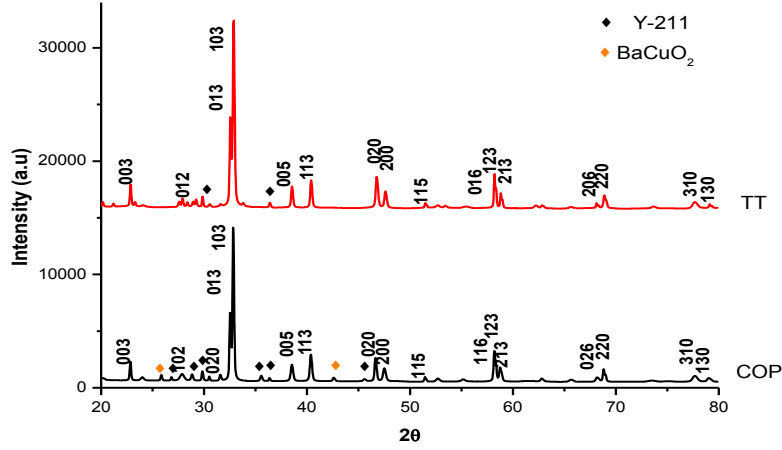


Figure 4: The XRD diffractograms for both pure Y-123 samples.

Figure 4 showed the diffractograms of the pure samples indexed to the same ICDD of Y-123 phase. Y-123 phase was successfully attained by both methods with the existence of Y-211 as the secondary phase. The existence of Y-211 phase in Y-123 matrix is very common as incomplete peritectic reaction occurs (Chainok et al., 2015). Rietveld refinement X'pert High Score revealed that the percentage of Y-123 phase is higher in TT samples, 91.5 % compared to 90.2 % in COP. The peaks observed for both samples are in good agreement with other literature (Bolzan et al., 1996). The major and significant peak with (hkl) (103) for Y-123 phase are observed in both samples at approximately $2\theta = 32.8^\circ$. Other significant peaks are found at peak position 32.54° (013), 58.22° (123), 46.45° (020), 40.38° (113), 22.85° (003), and 38.52° (005). However, extra peaks in COP sample showed traces of impurities which are due to BaCuO_2 . As for the lattice parameter, both samples follows the results obtained by other literatures where $a=3.2\text{\AA}$, $b=3.8\text{\AA}$ and $c=11.6\text{\AA}$ (A. A. Bolzan et al., 1996; Gholipour et al., 2011). They also possess orthorhombic crystal structure, known to be the superconducting structure in YBCO system. The summary of T_C , lattice parameter and percentage of phases are as in Table 1.

Table 1: The summary of $T_{C\text{-onset}}$, $T_{C\text{-offset}}$, percentage of phases and lattice parameter for each sample.

Methods	$T_{C\text{ onset}}$ (K)	$T_{C\text{ offset}}$ (K)	% Y123	% Y211	% BacuO ₂	$a/\text{\AA}$ (± 0.001)	$b/\text{\AA}$ (± 0.001)	$c/\text{\AA}$ (± 0.001)
COP	90	83	90.2	6.4	3.4	3.8252	3.8856	11.658
TT	92	88	91.5	8.5	-	3.8201	3.8846	11.676

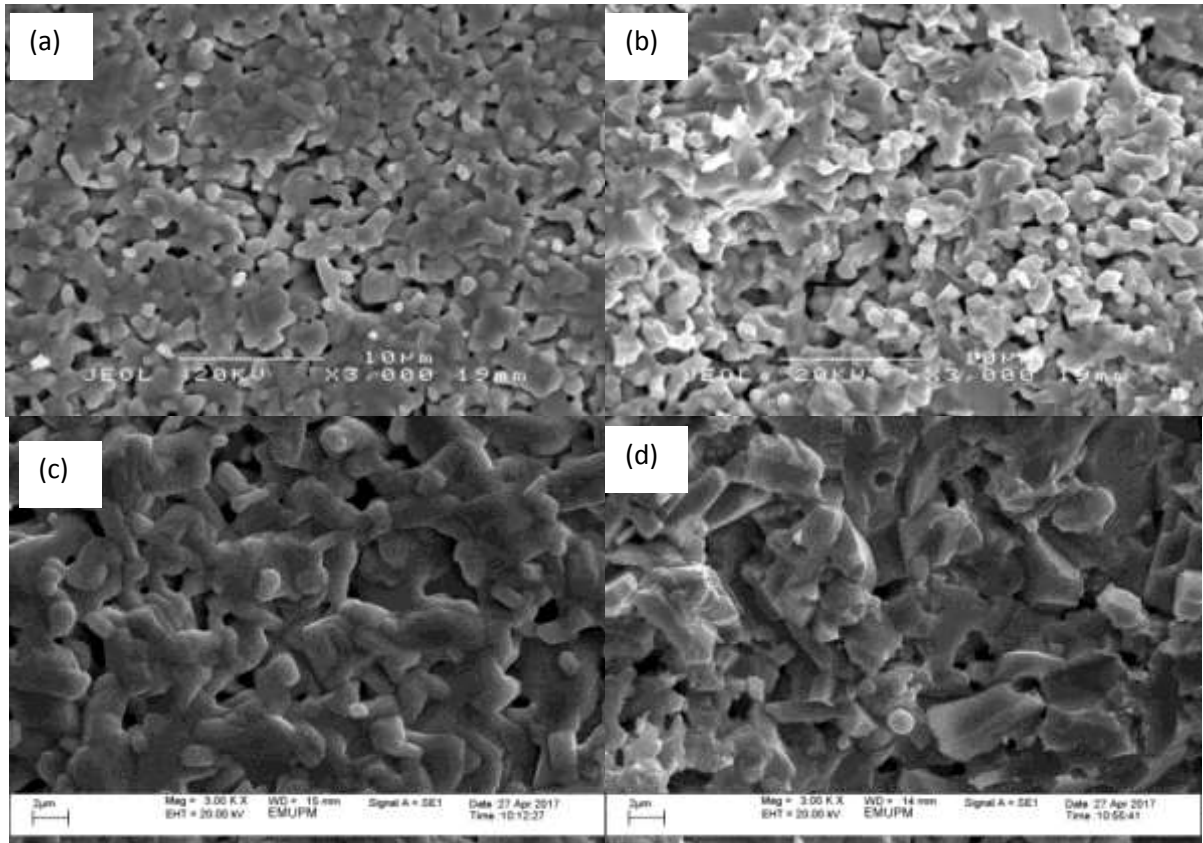


Figure 5: SEM images of Y-123 samples prepared via COP (a) surface, (b) cross section, and TT method (c) surface and (d) cross section.

Scanning electron microscope (SEM) images in Figure 5 showed the surface and cross section morphology for both bulk samples. In Fig 3 (a) and (c), TT sample is observed to have larger grain size sample compared to COP. The measured average grain size for both methods is $1.592\ \mu\text{m}$ and $0.99\ \mu\text{m}$ in TT and COP respectively. A better view of the grain size distribution is presented in figure 4. TT method also yields a denser grain alignment with less porosity compared to COP as seen in Fig 3 (b) and (d) which is suitable for tape application (Yeoh & Abd-Shukor, 2008). The large grain growth is due to the higher temperature used during the sintering process. EDX analysis on both surfaces further confirmed the materials in the sample and the co-existence of Y-123 and Y-211 phases as well as BaCuO_2 as per listed in Table 1.

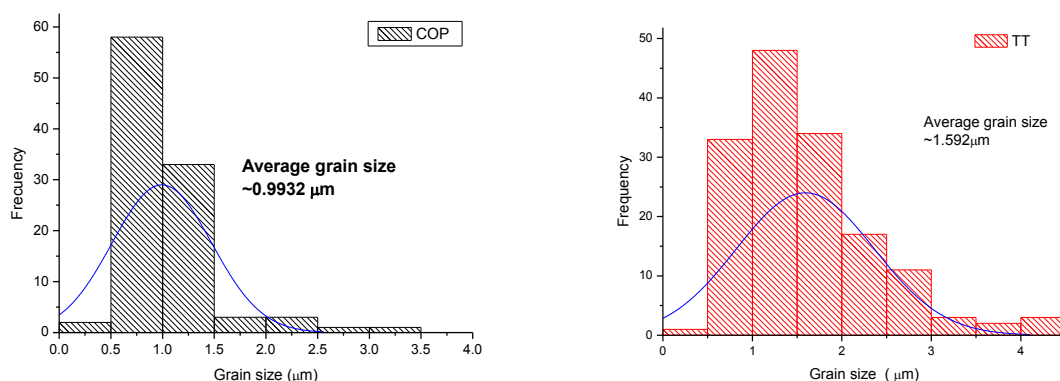


Figure 6: The grain size distribution of both samples.

Conclusion

In terms of the feasibility of the two methods discussed, thermal treatment method seems to have better advantage with its hassle free technique. In COP method, pH of the solutions needed to be maintained to ensure that none or less metal salts ended up in the filtrate altering the initial composition of the material. Thermal treatment simply neglects this feature since it only uses evaporation to dry and obtain the precursor. Hence, the initial can be better maintained. It was also observed that thermal treatment used less material and causes less by-product effluents. The results showed that TT method shows better quality Y123 with sharper transition and closer value of T_c to the standard. Both method yields high percentage of Y123 with Y211 as the secondary phase. COP however showed the presence of other impurities due to $BaCuO_2$. The SEM images show a significant difference in the size of both samples. TT yields larger grain size with much more dense morphology compare to COP samples due to its higher sintering temperature. While the differences on terms of T_c and phase percentage are not much, one could consider TT treatment for a more environmental friendly route.

Acknowledgement

The authors would like to thanks to Ministry of Education Malaysia (MOE) for Exploratory Research Grant Scheme (ERGS 5527174) and JPA, PMC scholarship for funding the project.

References

- Bhargava, A., Mackinnon, I. D. R., Yamashita, T., & Page, D. (1995). Bulk manufacture of YBCO powders by coprecipitation. *Physica C: Superconductivity*, 241, 53–62.
- Bolzan, A. a., Millar, G. J., Bhargava, A., Mackinnon, I. D. R., & Fredericks, P. M. (1996). A spectroscopic comparison of YBCO superconductors synthesised by solid-state and coprecipitation methods. *Materials Letters*, 28(September), 27–32.
- Bolzan, A. A., Millar, G. J., Bhargava, A., Mackinnon, I. D. R., & Fredericks, P. M. (1996). A spectroscopic comparison of YBCO superconductors synthesised by solid-state and coprecipitation methods. *Materials Letters*, 28(1–3), 27–32.
- Chainok, P., Khuntak, T., Sujinnapram, S., Tiyasri, S., Wongphakdee, W., Kruaehong, T., ... Udomsamuthirun, P. (2015). Some properties of $YBa_mCu_{1+m}O_y$ ($m=2,3,4,5$)

- superconductors. *International Journal of Modern Physics B*, 29(9), 1–12.
- Chen, D. H., Liu, T. W., Huang, J. C., Cheng, C. H., Chang, C. T., Sheen, S. R., ... Wu, M. K. (1994). Synthesis of $\text{YBa}_2\text{Cu}_3\text{O}_7$ and $\text{YBa}_2\text{Cu}_4\text{O}_8$ superconductors via carbonate coprecipitation. *Materials Letters*, 21(September), 15–20.
- Dihom, M. M., Shaari, A. H., Baqiah, H., Al-Hada, N. M., Kien, C. S., Azis, R. S., ... Abd-Shukor, R. (2017). Microstructure and superconducting properties of Ca substituted $\text{Y}(\text{Ba}_{1-x}\text{Ca}_x)_2\text{Cu}_3\text{O}_7$ ceramics prepared by thermal treatment method. *Results in Physics*, 7, 407–412.
- Dubinsky, S., Lumelsky, Y., Grader, G. S., Shter, G. E., & Silverstein, M. S. (2005). Thermal degradation of poly(acrylic acid) containing metal nitrates and the formation of $\text{YBa}_2\text{Cu}_3\text{O}_{7-x}$. *Journal of Polymer Science, Part B: Polymer Physics*, 43(10), 1168–1176.
- Gene, S. A., Saion, E. B., Shaari, A. H., Kamarudeen, M. A., & Al-Hada, N. M. (2015). Fabrication and Characterization of Nanospinel ZnCr_2O_4 Using Thermal Treatment Method. *Advanced Materials Research*, 1107, 301–307.
- Gholipour, S., Daadmehr, V., Rezakhani, A., H. Khosroabadi, F., Shahbaz Tehrani, R., & Akbarnejad, H. (2011). Y358 against Y123 structural phase in a Y-based superconductor. *arXiv*, 1. Retrieved from <http://arxiv.org/abs/1110.0893>
- Hamadneh, I., Agil, A., Yahya, A. K., & Halim, S. A. (2007). Superconducting properties of bulk $\text{Bi}_{1.6}\text{Pb}_{0.4}\text{Sr}_2\text{Ca}_{2-x}\text{Cd}_x\text{Cu}_3\text{O}_{10}$ system prepared via conventional solid state and coprecipitation methods. *Physica C: Superconductivity and Its Applications*, 463–465(SUPPL.), 207–210.
- Hamadneh, I., Halim, S. A., & Lee, C. K. (2006). Characterization of $\text{Bi}_{1.6}\text{Pb}_{0.4}\text{Sr}_2\text{Ca}_2\text{Cu}_3\text{O}_y$ ceramic superconductor prepared via coprecipitation method at different sintering time. *Journal of Materials Science*, 41(17), 5526–5530.
- Keiji Kaneko, Hideo Ihara, asayuki Hirabasyi, Norio Terada, K. S. (1987). On the Coprecipitation Method for the Preparation of High T_c M-X-Cu-O (M=Ba, Sr, X=La, Y) System. *Jap*, 26(5), L734–L735.
- Khalid, N. A. (2016). *Carbon Nanofibers (CNFs) and Carbon Nanotubes (CNTs) Effect on The Superconducting and Physical Properties of Superconductor $\text{YBa}_2\text{Cu}_3\text{O}_{7-\delta}$ Bulks*. Univerisiti Putra Malaysia.
- Patnaik, P. (2003). *Handbook of Inorganic Chemicals. Ebook*. Retrieved from [ftp://pvictor.homeftp.net/public/Sci_Library/Chem Library/Handbooks/Patnaik P. Handbook of inorganic chemicals \(MGH, 2003\)\(T\)\(1125s\).pdf](ftp://pvictor.homeftp.net/public/Sci_Library/Chem Library/Handbooks/Patnaik P. Handbook of inorganic chemicals (MGH, 2003)(T)(1125s).pdf)
- Patta, Y. R., Wesolowski, D. E., & Cima, M. J. (2009). Aqueous polymer-nitrate solution deposition of YBCO films. *Physica C: Superconductivity and Its Applications*, 469(4), 129–134.
- Petropoulou, M., Argyropoulou, R., Tarantilis, P., Kokkinos, E., & Parissakis, G. (2002). Comparison of the oxalate co-precipitation and the solid state reaction methods for the production of high temperature superconducting powders and coatings, 127, 122–128.
- Ramli, A. (2016). *Role Nd2O3 nanoparticles addition on mircostructural and superconducting properties of $\text{YBa}_2\text{Cu}_3\text{O}_7$ ceramics*. Unviversiti Putra Malaysia.
- Ramli, A., Shaari, A. H., Baqiah, H., Kean, C. S., Kechik, M. M. A., & Talib, Z. A. (2016). Role of Nd_2O_3 nanoparticles addition on microstructural and superconducting properties of $\text{YBa}_2\text{Cu}_3\text{O}_{7-\delta}$ ceramics. *Journal of Rare Earths*, 34(9), 895–900.
- Schildermans, I., Knaepen, E., Nouwen, R., Bael, M. K. Van, Vanhoyland, G., Mullens, J., ... Poucke, L. C. Van. (1999). Thermal treatment of a Y-123 precursor prepared using the hydroxide co-precipitation method q, 1, 351–355.
- Shter, G. E., & Grader, G. S. (1993). YBCO Oxalate Coprecipitation in Alcoholic Solutions, 1436–1440.
- Skirius, S. A., Mathias, H. H. G., Hascicek, Y. S., Shankle, G., & Clark, R. J. (1994). Synthesis of high temperature superconducting ceramics by oxalate coprecipitation

from non-aqueous solvents. *Applied Superconductivity*, 2(2), 127–133.

Yeoh, L. M., & Abd-Shukur, R. (2008). The study on various wet chemistry techniques on $\text{YBa}_2\text{Cu}_3\text{O}_{7-\delta}$ superconducting oxides powder preparation. *Journal of Non-Crystalline Solids*, 354(34), 4043–4048.

CHAPTER 5

SEMICONDUCTORS AND APPLICATIONS

5.1 The effect of sintering time on the microstructural and nonlinear electrical properties of Zn-V-Mn-Nb-Gd-O low-voltage varistor ceramics

Nor Hasanah Isa, Rabaah Syahidah Azis, Nor Kamilah Sa'at, Azmi Zakaria, Raheleh Mohammadi and Rosnu Kinsu

Abstract

There is lacking of study on the prolonged sintering time effect on the microstructural and nonlinear electrical properties of ZnO-V₂O₅-MnO₂-Nb₂O₅-Gd₂O₃-based low-voltage varistor ceramics sintered at 900 °C. The aim of this study is to investigate the effect of sintering time from 120 to 210 mins on the microstructural and nonlinear electrical properties of the ceramics. The prolonged sintering time normally is expected to disrupt the microstructural and to decrease the nonlinear electrical properties of the ceramics. The sample was prepared via solid-state method and sintered at 900 °C. XRD results shows that the MnV, GdMnO₃, Mn₂Nb₂Zn₂O₉ and ZnV₂O₄ phase disappeared with increasing sintering time. The ZnO peak shift to the low diffraction angle from 47.5341° to 47.4995° and the interplanar space increases slightly from 1.9129 to 1.9142 Å. The density decreases from 5.22 to 4.62 gcm⁻³. The average grain size decreases from 3.56 to 3.19 μm due to pinning action by Gd₂O₃ at the grain boundary which accelerate the annihilation of Zn and O elements as shown by EDX maps. Thus, the barrier height decreases from 0.67 to 0.65 eV and nonlinear α value is decreases as expected from 9.91 to 7.01 and correspondingly the breakdown field E_{1mA} decreases from 88.48 to 71.04 V/mm at 210 min.

Keywords: sintering time; microstructural properties; nonlinear electrical properties; Zn-V-Mn-Nb-Gd-O-based varistor; low-voltage varistor

Introduction

Zinc oxide (ZnO)-based varistors are semiconducting ceramic devices used to protect electrical devices from harmful overvoltage. The low voltage devices without varistor had risk being exposed to overvoltage transient repeatedly and have a high chance to damage. The ZnO-based varistor is a metal oxide varistor which produced by sintering ZnO powder containing additives of small amount such as vanadium (V), bismuth (Bi), manganese (Mn), niobium (Nb), and antimony (Sb) [1,2]. The nonlinear properties of ZnO-based varistors ceramics are ascribed to double Schottky barrier formed at active grain boundaries [3,4]. Double Schottky Barrier model proposed that the barrier in the ZnO varistors can be related to the n-p-n junction where the bulk of material behaves as an *n*-type semiconductor and the interface behaves as a *p*-type semiconductor [5].

The studies of Zn-V-Mn-Nb-O varistor ceramics substituted with rare earth oxides (REOs) such as gadolinium oxide (Gd₂O₃) and erbium oxide (Er₂O₃) at 900 °C shows low breakdown electrical field (E_{1mA}) value at 1 mA which are 536.5 and 544.4 V/mm which is

too low to meet the demand for high-voltage protection which above 1000 V [6,7]. However, the low-voltage varistor based on Zn-V-Mn-Nb-O ceramics substituted with 0.03 mol% of Gd₂O₃ and Nd₂O₃ sintered at 900 °C shows good nonlinear α value which are 9.91 and 9.94 and low E_{1mA} value which are 88.48 and 75.05 V/mm [8,9]. Study shows that the prolonged sintering time from 1 to 3 h deteriorates the varistor properties of the ZnO-based ceramics substituted with dysprosium oxide (Dy₂O₃) and yttrium oxide (Y₂O₃) where it reduces the nonlinear, α value from 55 to 38 and from 51.2 to 23.8 and the breakdown field from 182 to 127 V/mm and from 194.5 to 117.4 V/mm [10,11].

However, there is lacking of study on the prolonged sintering time effect on the microstructural and nonlinear electrical properties of ZnO-V₂O₅-MnO₂-Nb₂O₅-Gd₂O₃-based low-voltage varistor at 900 °C. The aim of this study is to investigate the effect of sintering time on the microstructural and nonlinear electrical properties of the ceramics. The prolonged sintering time is expected to diminish the microstructural and nonlinear electrical properties of the ceramics. In this paper, the effect of sintering time from 120 to 210 min on the microstructural and electrical properties of ZnO-V₂O₅-MnO₂-Nb₂O₅-Gd₂O₃-based low voltage varistor ceramics was discussed.

Materials and Methods

Sample Preparation

The sample was fabricated according to (97.37) ZnO (0.5) V₂O₅ (2) MnO₂ (0.1) Nb₂O₅ (0.03) Gd₂O₃ from high-purity reagent-grade raw materials (> 99.9%, Alfa Aesar). All the units used in the bracket are in mol percentage. Raw materials were ground using ball milling with zirconia balls with distilled water for 24 h. The slurry was dried at 70 °C for 12 h before adding the binder polyvinyl alcohols 1.75 wt% and then sieving through the 75 μ m mesh screen. The powder from each ceramic combination was pressed into pellets with 10 mm diameter and 1 mm in thickness at a pressure of 4 tonne/m². The pellets were sintered at a temperature of 900 °C in air for 120, 150, 180 and 210 min with heating and cooling rates of 5 °C/min.

Microstructure and density measurement

The crystalline phase was identified using Cu K α radiation ($\lambda = 1.540598 \text{ \AA}$) with PANalytical X'Pert. XRD software X'Pert high score software Pro PW3040/60) was used to analyse crystalline phases. The surface microstructure was examined by a scanning electron microscope (SEM, model: LEO 1455 VPSEM). One side of the samples was lapped and ground with SiC paper, and then polished with 0.3 μ m Al₂O₃ powder to make a mirror-like surface. The average grain size (D) was determined by the linear intercept method through the expression;

$$D = \frac{1.56L}{MN} \quad \text{Eq. (1)}$$

where L is the length of a random line drawn on a micrograph of sample surfaces, M is the micrograph magnification, N is the number of grain boundaries intercepted by the line, and 1.56 is the correction factors required for converting the D from average intercept diameter [12]. The average density (ρ_{avg}) of sintered sample was determined using an electronic densimeter (Alfa Mirage, Model MD-300S), working based on the Archimedes principle.

Electrical measurement

The current density, J - electric field, E characteristics at room temperature were measured using a low-voltage source-measure unit (Keithley Model 2410) to obtain pellet sample non-linear coefficient (α). The measurement was performed by varying the applied voltage from 0 to 100 V. All samples were coated with silver conductive paint and cured at 550 °C for 10 mins to make the electrodes. The nonlinear α value was determined from J - E plot through the expression:

$$\alpha = \frac{\log J_2 - \log J_1}{\log E_2 - \log E_1} \quad \text{Eq.(2)}$$

where E_1 and E_2 are the electric fields corresponding to $J_1 = 1 \text{ mAcm}^{-2}$ and $J_2 = 10 \text{ mAcm}^{-2}$, respectively. The breakdown field ($E_{1\text{mA}}$) was measured at current density of 1 mAcm^{-2} . It is well accepted that thermionic emission is the predominant conduction mechanism in the pre-breakdown region. For this reasons, the barrier height Φ_b is estimated by:

$$J = AT^2 \exp\left(\frac{\beta E^{1/2} - \phi_B}{k_B T}\right) \quad \text{Eq. (3)}$$

where k_B is the Boltzmann constant ($8.167 \times 10^{-5} \text{ eVK}^{-1}$), A is the Richardson's constant for ZnO ($30 \text{ A/cm}^2\text{K}^2$), T is the absolute temperature, β is a constant related to the relation as $\beta \sim (r\omega)^{-1}$, where r is grains per unit length and ω is the barrier width [13].

Results and Discussion

Figure 1 shows the XRD patterns of ZnO-based varistor ceramics substituted with 0.03 mol% of Gd_2O_3 which sintered at different sintering time. The major diffraction peaks belong to ZnO as the primary phase and the minor diffraction peaks show the MnV, GdMnO_3 , $\text{Mn}_2\text{Nb}_2\text{Zn}_2\text{O}_9$ and ZnV_2O_4 as the secondary phase which disappeared at sintering longer than 120 mins. The disappearance of secondary phase causes the ZnO peak shift to the low diffraction angle from 47.5341 to 47.4995° and increases the interplanar space slightly from 1.9129 to 1.9142 \AA . The similar trends of peak position shift also reported by Duhan (2009). Figure 2 shows the SEM micrographs of Gd_2O_3 substituted ZnO-based varistor ceramic sintered at different times. The liquid phase observed at the grain boundaries and the triple point junction for sample sintering longer than 120 min. EDX elemental maps in Figure 3 show the surface of ZnO grain exhibit Zn-rich and O-rich element at 120 min become Zn-poor and O-poor element at 210 min. Meanwhile the grain boundaries exhibit O-poor element at 120 min and almost disappeared at 210 min.

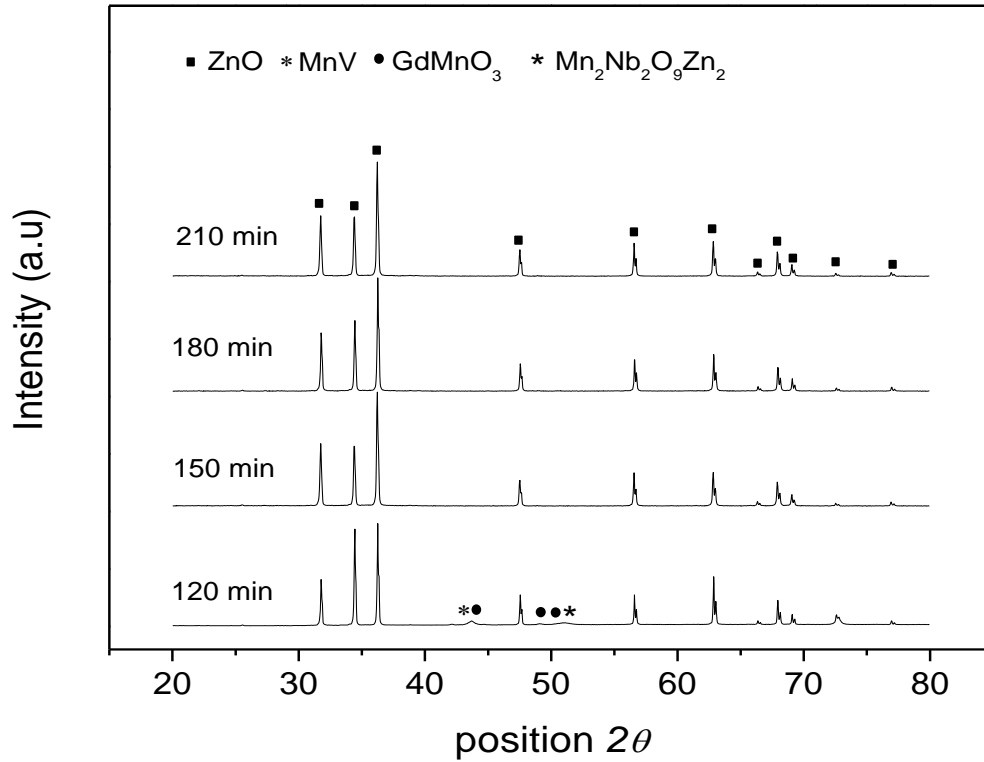


Figure 1: XRD patterns of Gd₂O₃ substituted ZnO based varistor ceramics sintered at different time

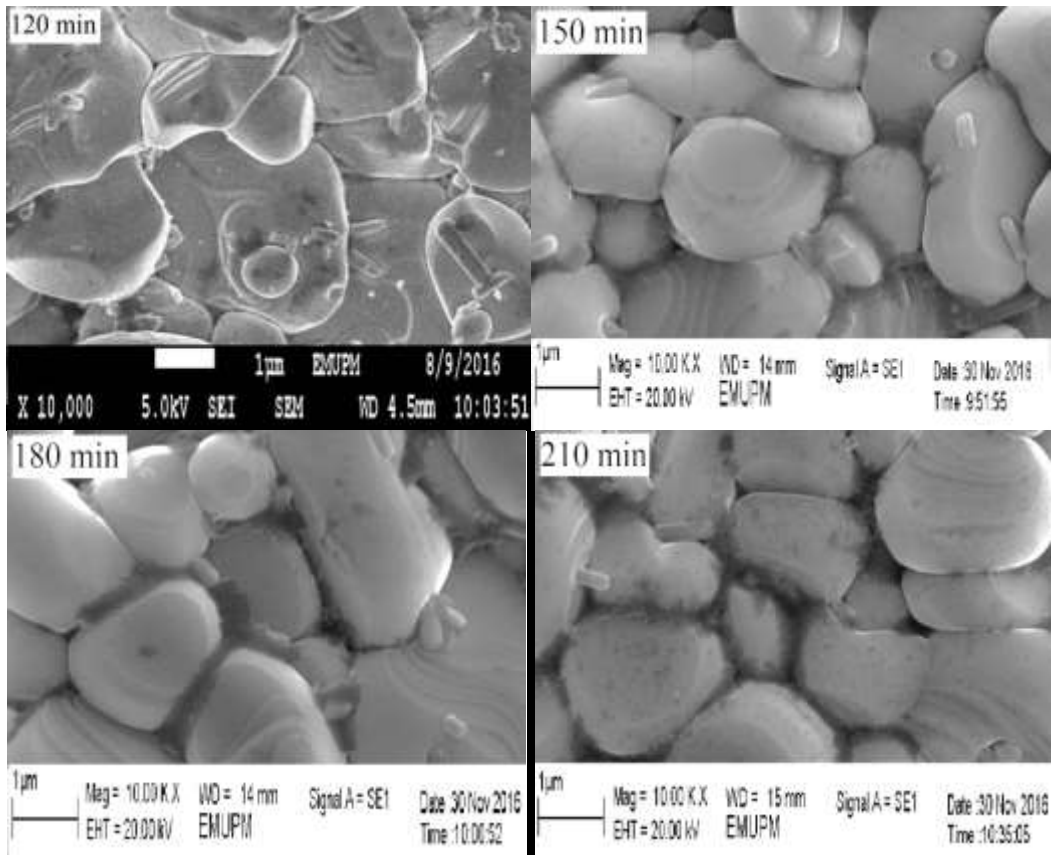


Figure 2: SEM micrograph of ZnO-based varistor sintered at different time

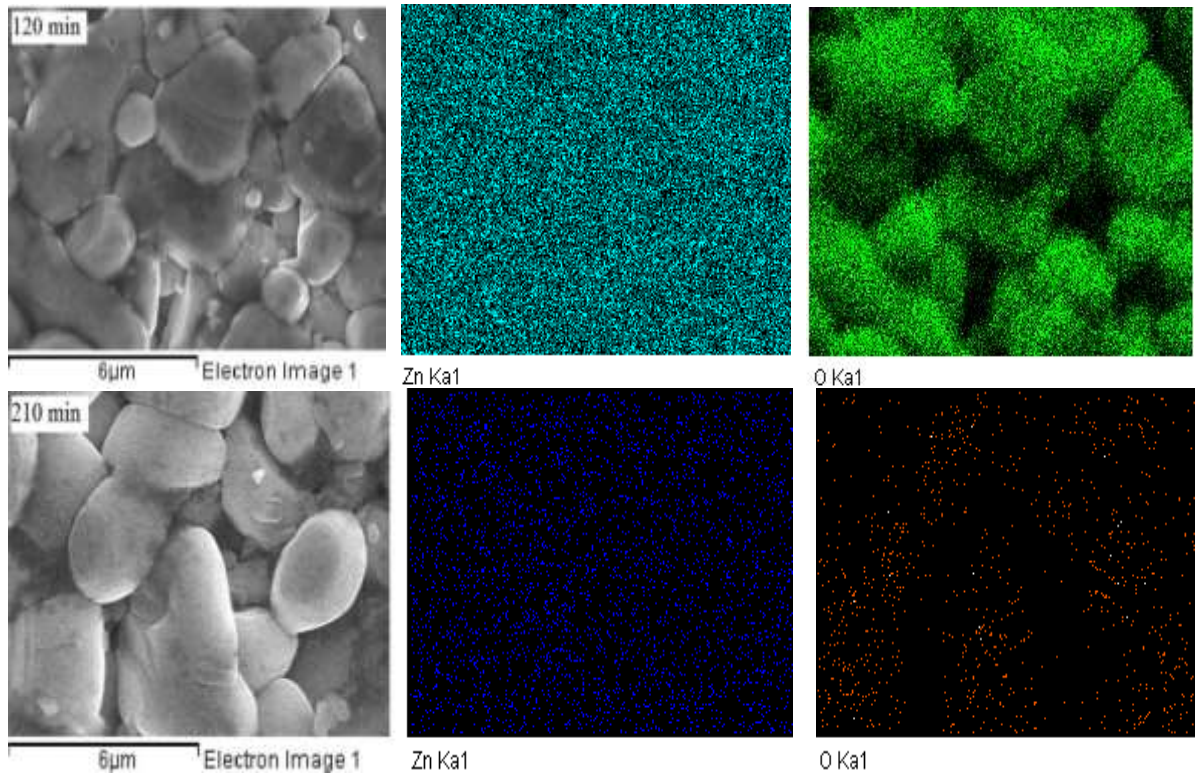


Figure 3: The EDX elemental maps of Gd_2O_3 substituted ZnO sintered at 120 and 210 min

Figure 4 shows the density (ρ) and average grain size (D) dependent on sintering time. The ρ decreases from 5.22 to 4.62 $g\,cm^{-3}$ with increasing sintering time due to the secondary phase disappearance but increases to 4.68 $g\,cm^{-3}$ at 210 mins due to the uniform distributed liquid phase around the sample microstructure. It is expected that the liquid phase act as a sintering aid that enhances the densification by a solution and re-precipitation of ZnO [15]. The average D decreased remarkably from 3.56 to 3.19 μm as the sintering time is increased. The liquid phase which is supposedly promoting the grain growth might react with Gd_2O_3 that acts as the grain inhibitor [8].

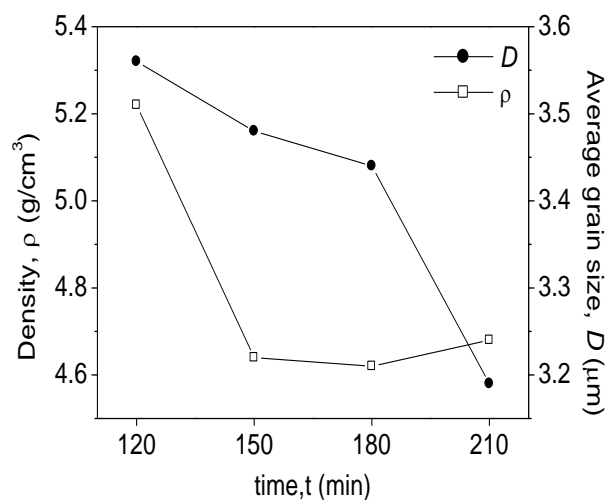


Figure 4: ρ and D dependence on sintering time

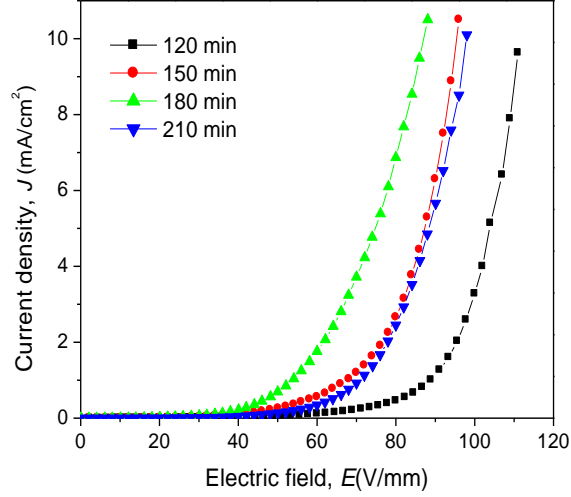


Figure 5: J - E curve of Gd_2O_3 substituted ZnO-based varistor sintered at different time

Table 1: Nonlinear coefficient (α), barrier height (Φ_b), and breakdown electric field (E_{1mA}) of Gd_2O_3 substituted ZnO-based ceramic varistors at different sintering time.

Sintering time (min)	α	Φ_b (eV)	E_{1mA} (V/mm)
120	9.91	0.67	88.48
150	7.28	0.65	68.69
180	5.05	0.64	55.43
210	7.01	0.65	71.04

Figure 5 shows the J - E curves Gd_2O_3 substituted ZnO varistor ceramics shift to the lower electric field region at longer sintering time except at 210 min where it shifts to the higher electric field region. The sharp knee of J - E curves indicate the non-linearity properties in Gd_2O_3 substituted ZnO varistor ceramics. The J - E parameters obtained from the characteristic curves are summarized in Table 1. The α value has been used to estimate nonlinear properties quantitatively. It has been well accepted that the oxygen species promote the density of interfaces states, thus increases the Φ_b and α value [16]. The Φ_b decreases from 0.67 to 0.64 eV and consequently decreases the α value from 9.91 to 5.05 with increasing sintering time up to 180 min as expected. The prolonged sintering time might increase the O-depleted due to the disappearance of secondary phase from 120 to 180 min and reduces the Φ_b . However, the Φ_b increased to 0.65 eV at 210 min which lead to an increasing the α value to 6.93. A well distributed of liquid phase around the grains might reduce the O-depleted which resulting increase in the Φ_b . The E_{1mA} decreases from 88.48 to 55.43 V/mm with increasing sintering time up to 180 min due to disappearance of secondary phases but increases to 71.04 V/mm at 210 min due to the increase of density.

Conclusion

The effect of sintering time on the nonlinear coefficient of Zn-V-Mn-Nb-O varistor ceramics substituted Gd_2O_3 were studied systematically. The prolonged sintering time disrupt the microstructural properties as expected where the Zn and O elements and secondary phases disappear which causes decreasing in density and grain size with increasing sintering time. The sintering time also diminish the nonlinear electrical properties as expected where the Φ_b , α and E_{1mA} value decrease with increasing sintering time up to 180 min.

Acknowledgements

The authors are grateful to the Universiti Putra Malaysia for supporting this work under the Universiti Putra Malaysia GRANT No. GP-IPS/2016/9493000 and FRGS/2016/5524942.

References

1. Matsuoka, M., (1971). Nonohmic Properties of Zinc Oxide Ceramics. *Jpn. J. Appl. Phys.* 10(6): 736- 746.
2. Kim, E.D., Kim, C.H., and Oh, M.Y., (1985). Role and effect of Co_2O_3 additive on the upturn characteristics of ZnO varistors, *J. Appl. Phys.*, 58, 3231.
3. Cheng, P., Li, S., and Alim, M.A., (2007). Soft core behavior in ZnO– Bi_2O_3 -based varistors containing oxides of Ce and Gd. *Phys. Stat. Sol.* 204(3), 887–899
4. Nahm, C.W. and Shin, B.C., (2003). Highly stable nonlinear properties of ZnO– Pr_6O_{11} –CoO– Cr_2O_3 – Y_2O_3 -based varistor ceramics. *Mater. Lett.*, 57,1322–1326
5. Mantas, P.Q., and Baptista, J.L., (1995). The Barrier Height Formation in ZnO Varistors, *J. Europ. Ceram. Soc.*, 15: 605–615
6. Nahm, C.W. (2011). Er_2O_3 Doping Effect on Electrical Properties of ZnO– V_2O_5 – MnO_2 – Nb_2O_5 Varistor Ceramics. *J. Am. Ceram. Soc.*, 94(10), 3227–3229
7. Nahm, C.W. (2013). Effect of gadolinia addition on varistor characteristics of vanadium oxide-doped zinc oxide ceramics, *J. Mater. Sci.: Mater Electron*, 24, 4839–4846
8. Isa, N.H., Zakaria, A., Azis, R.S., and Rizwan, Z., (2017). Microstructural and Nonlinear Properties of Zn-V-Mn-Nb-O Varistor Ceramics with Gd_2O_3 substitution for Low Voltage Application, *Solid State Phenom.*, 268,181-185
9. Isa, N.H., Zakaria, A., Azis, R.S., and Abdullah, W.R.W., (2017). Microstructure and Nonlinear Properties of Zn-V-Mn-Nb-O Varistor Ceramics with Nd_2O_3 Substitution, *Dig. J. Nanomater. and Biostruct.*, 12 (3), 821-827
10. Nahm, C.W. (2004). Effect of sintering time on varistor properties of Dy_2O_3 -doped ZnO– Pr_6O_{11} -based ceramics, *Mater. Lett.* 58: 3297–3300
11. Nahm, C.W. and Shin, B.C., (2004). Effect of sintering time on electrical properties and stability against DC accelerated aging of Y_2O_3 -doped ZnO– Pr_6O_{11} -based varistor ceramics, *Ceram. Int.* 30, 9–15
12. Wurst, J.C., and Nelson, J.A., (1972). Linear Intercept Technique for Measuring Grain Size in Two-phase Polycrystalline Ceramics. *J. Am. Ceram. Soc.*, 55(2), 109
13. Li, C., Wang, J., Su, W., Chen, H., Wang, W., and Zhuang, D., (2001). Investigation of electrical properties of $\text{SnO}_2 \cdot \text{Co}_2\text{O}_3 \cdot \text{Sb}_2\text{O}_3$ varistor system. *Phys. B*, 307, 1–8

14. Duhan, S., (2009). Effect of sintering time on particle size of rare earth compound (R=Nd) prepared by wet chemical method. *Indian J. Pure App.Phys.* 47, 872-875
15. Zahid, R., Azmi, Z., and Sabri, M.G.M, (2011). Photopyroelectric Spectroscopic Studies of ZnO-MnO₂-Co₃O₄-V₂O₅ Ceramics. *Int. J. Mol. Sci.*, 12(3), 1625-1632
16. Abdullah, W.R.W., Zakaria, A., and Ghazali, M.S.M., (2012). Synthesis Mechanism of Low-Voltage Praseodymium Oxide Doped Zinc Oxide Varistor Ceramics Prepared Through Modified Citrate Gel Coating, *Int. J. Mol. Sci.* 13(4), 5278-5289

5.2 Controlled surface layer conditions of anodic aluminum oxide (AAO) templates during electrodeposition of Indium Antimonide nanowires

Osamah Ali Fayyadh, Intan Nur Ain Arifin, Azelah Khairudin, Jumiah Hassan, Suriati Paiman

Abstract

Indium antimonide (InSb) nanowires are remarkable combination of group III-V semiconductors that have been used in various electronic devices due to its narrow band gap and high electron mobility. The samples were synthesized using AAO template-assisted electrodeposition technique. Prior to the nanowires growth, bottom side of the AAO templates were deposited with a gold (Au) film to be used as a conductive layer. In order to study the effects of the template conditions on structural properties of InSb nanowires, templates were covered with insulating tape on top of the conductive gold layer. The nanowires synthesized from both covered and uncovered templates were characterized using field emission scanning electron microscopy (FESEM) and energy dispersive x-Ray (EDX) techniques. For the covered template condition, the FESEM images indicated that the sample have less presence of overgrown rough film on the topside of AAO template and smooth sidewall surface of the nanowires. Whereas for uncovered template condition, longer nanowires (5.6 ± 0.8) μm with rougher surface were observed. The overall EDX analysis shows that the nanowires from the covered template condition exhibited right stoichiometric ratio than the ones from the uncovered template condition. This study provides better results for structural properties in order to study the electrical properties for InSb nanowires and open new opportunities for using these nanowires in future devices.

Keywords: *InSb nanowires, AAO template, electrodeposition, conductive layer, insulating tape*

Introduction

III-V Semiconductor nanowires (NWs) represent as a unique system for exploring phenomena at the nanoscale and are also expected to play a critical role in future electronic and optoelectronic devices (Lu and Lieber 2006). In addition, their large surface to volume ratio allows for distinct structural and chemical behavior (Yang, 2010). Indium antimony (InSb) is among the group III-V semiconductors nanowires that have advantages of high electron mobility with speed of about $77,000 \text{ cm}^2 \text{ V}^{-1} \text{ S}^{-1}$, which is found to be higher than those of other types of known semiconductors (Kuo et al., 2013). Due to its unique electronic and optoelectronic properties, InSb has been employed in a wide variety of applications, such as in medical application as biosensor (Singh et al., 2015), infrared detectors (Dixit et al., 2013), emitters (Gangloff et al., 2004), magnetic field sensors (Takamura et al., 2015), toxic gas sensors for detecting gases of acetone, ammonia, NO_2 , ethanol, hydrogen and ozone (Gang 2011), and most recently in low power high-speed electronics devices (Zhang et al., 2005). The potential use of InSb nanowires in these nanodevices has attracted intensive interest to synthesize and understand their structural properties.

Anodic alumina oxide (AAO) templates are widely employed in the nanowire growth methods such as electrodeposition technique due to its ability to withstand higher temperatures, insoluble in organic solvent and cost-effective (Sisman, 2011). This technique is also fast and straightforward for fabricating highly ordered and well-aligned nanowires (Khan et al., 2008; Hnida et al., 2013). However, the drawback of using the template as a growth substrate is that there is a tendency of an overgrown bulk microlayer to be produced on top of it, despite having used the optimized growth parameter (Singh, Algarni, and Philipose, 2017). The presence of this bulk microlayer causes for unstable stoichiometry of the nanowires and its rougher surfaces, which will significantly reduce the performance of its electrical (Fang et al., 2014) and optical properties (Sahu and Nanda 2000). Therefore, the study of the

template condition is important as an effort to minimize the bulk microlayer, and hence achieving good stoichiometry as well as smooth surface of the nanowires.

Some literature works have reported on the utilization of insulating tapes in the fabrication of nanowires, which were found to be well-aligned with high aspect ratio and reasonable high pore-filling factor (Irshad et al., 2014). However, detailed analysis on its structural properties due to the presence of the insulating tape was not properly discussed (Irshad et al., 2014). This paper aims to investigate the effects of AAO template conditions on the structural properties of InSb nanowires by comparing between the uncovered and covered template with insulating tape.

Experimental

InSb nanowires were synthesis by AAO template-assisted using electrochemical deposition. The electrodeposition was carried out in a typical three-electrode electrochemical cell, which was equipped with a platinum (Pt) electrode as the counter electrode, Ag/AgCl as references electrode, and the AAO template as the working electrode. The AAO template was purchased from the Whatman Inc. Florham Park, and its bottom side was coated with a gold (Au) layer in order to serve as a conduction contact. The diameters of the pores in the AAO are 200 nm. The deposition was controlled by a potentiostatic, conducted for 30 mins under the deposition potential of -1.5 V at room temperature. Some of AAO templates were then covered with insulating tape at the bottom of the conductive gold layer, to investigate the growth and morphology of nanowires. The insulating tape was applied during the preparation process before the beginning of electrodeposition. Then, the electrolyte was composed of 0.03 M indium trichloride ($InCl_3$), 0.02 M antimony trichloride ($SbCl_3$), 0.1 M tartaric acid ($C_4H_6O_6$), 0.002 M hydrochloric acid (HCl) and distilled water. The $InCl_3$ and $SbCl_3$ used as metal ion sources. The tartaric acid is used as complexing agents to bring the deposition potential of In and Sb closer to maintain binary growth. After the deposition, the sample was washed several times in distilled water. After that, the AAO templates were immersed in 3 M NaOH solution for 20 minutes until all the AAO completely dissolve. The samples were then centrifuged with deionized water. Immediately after centrifuged, the solution was pipetted on glass slides for characterization purposed. Structural and elemental composition studied of InSb nanowires was performed using Field Emission Scanning Electron Microscope (FESEM JEOL JSM-7600F) equipped with energy dispersive X-ray spectroscopy (EDX).

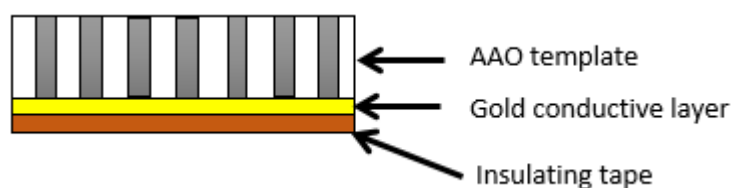


Figure 1: The schematic diagram of AAO with insulating tape

Results and Discussion

Field emission scanning electron microscopy (FESEM) were used to study the structural properties of InSb nanowires for characterizing the surface morphology, length and diameter. It is important to produce the InSb nanowires with the right stoichiometric for chemical composition and better morphology. Figure 2 a) and b) show the side view FESEM images of AAO template for the uncovered and covered with insulating tape sample. Clearly the insulating tape has a significant effect on the template-assisted nanowires growth. It was observed that the AAO template surface in Figure 2a exhibit much less overgrown rough film compared to the template surface in Figure 2b. The movement

of ions in the insulating-covered samples cannot attract to the conductive layer, while in uncovered samples have strong attraction force to the conductive layer. It's believed that this process changed the InSb ions direction to enter the pores from the bottom side to the upper side of AAO as shown in the sketched in Fig 1). It is possible that, when the chemical and electrical contacts between the directing substrate and the material in the pore channel were hindered by the insulating obstruction layer (Zhao, Seo, Lee, & Lee, 2007). On the other hand, the thick overgrowth microlayer seen in the Figure 2(b) indicates the increased dispersion of InSb ions to the nanowires growth front due to the steady increase in current with the growth time. Similar morphology were observed with rough films formed on the top of AAO template when the nanowires entirely completed the pores (Singh, Algarni and Philipose 2017).

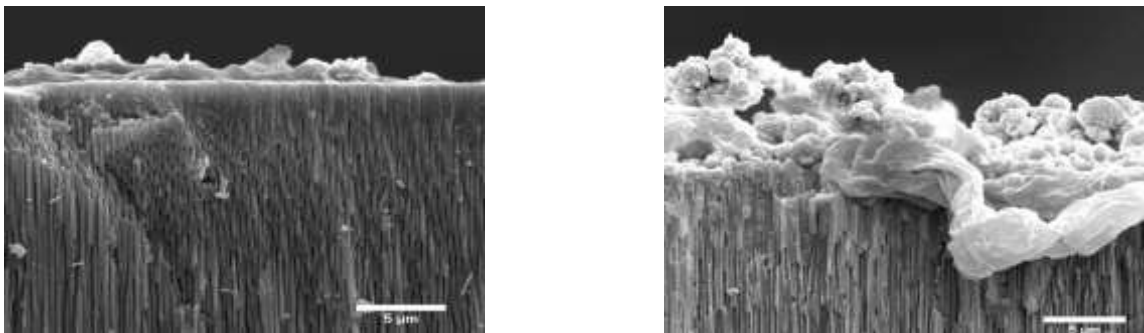


Figure 2. (a) AAO with insulating tape, (b) AAO without insulating tape.

The EDX measurements of AAO on the rough films in Fig 3 a) and b) confirmed the formation of InSb but in micro structure. While other elements were obtained such as Al from the AAO template did not dissolve completely and Au was from gold layer that sputtered on the AAO template before the deposition process. Table 1 shows the chemical composition for the covered samples Fig 3 a) less than in un covered samples in Fig 3 b) due to the presence of insulating tape as we mentioned earlier.

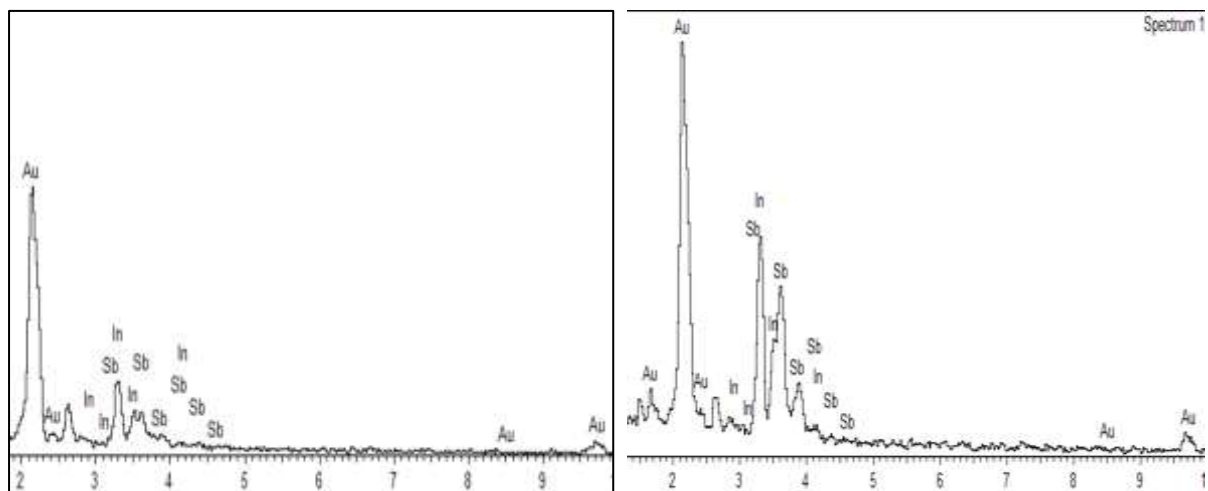


Figure 3: a), b) EDX analysis spectrum for the rough films of the AAO template for with and without insulating tape respectively.

Table 1: The chemical composition of InSb on the rough films of AAO template with different conditions

AAO conditions	Atomic	
	In	Sb
AAO template with insulating tape	16.60	10.66
AAO template without insulating tape	28.69	22.20

The drop-casted InSb nanowires on glass substrates after dissolving the AAO were then carefully studied by FESEM and ImageJ. The top-view FESEM images show different surface sidewalls morphology where sample with insulating tape (Figure 3a) exhibit a smooth surface as compared to those without insulating tape (Figure 3b). The rough sidewalls of nanowires in Figure 3b was possibly resulted from the high presence of the overgrown rough film. Once the AAO template was dissolved, the rough film was distributed into tiny particles and attached to the surface of the nanowires.

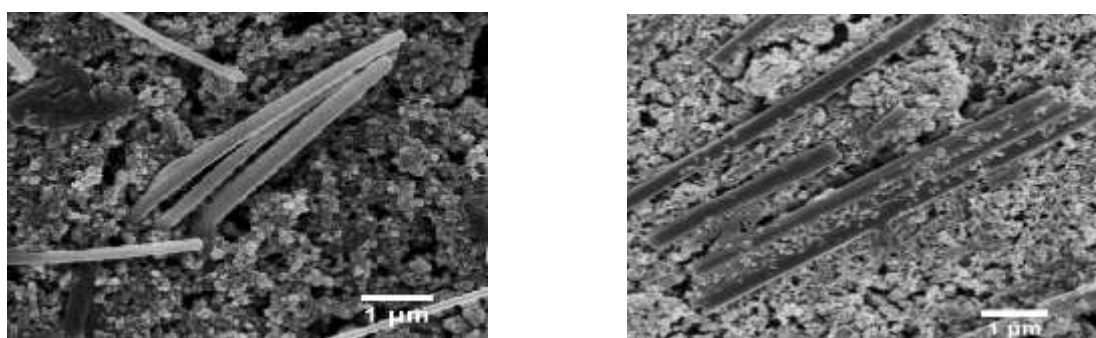


Figure 4. (a) drop-casted InSb nanowires for sample with insulating tape, (b) drop-casted InSb nanowires for sample without insulating tape.

To determine the influence of AAO condition on the chemical composition and atomic ratio, the EDX analysis through FESEM observation was carried out. The EDX spectrum for InSb nanowires of AAO templates with and without insulating tape was shown in Figure 5 below. Figure 5 confirmed the formation of InSb nanowires in spite of other elements than In and Sb were presented. The oxide (O) present due to oxidation that may have formed during the preparation of the electrolyte and post storage. While, the Au element came from the gold layer that was sputtered on the AAO template before the deposition process and Au sputtered on the glass slide before the FESEM characterization for a better image.

Table 2 shows the ratio of In:Sb for different AAO template condition. The quantitative analysis of AAO template with and without insulating tape have showed an atomic composition ratio of In:Sb is 1.27:1 and 1.4:1 respectively. Therefore, the AAO template with insulating tape has a better result that achieved the right stoichiometric composition of InSb nanowires.

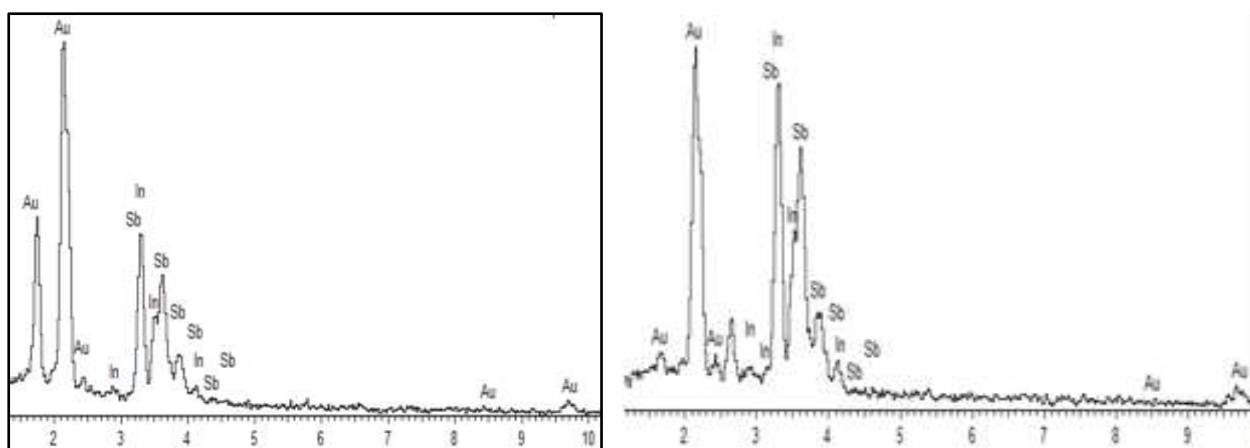


Figure 5: a), b) EDX analysis spectrum for InSb nanowires (drop casted) after dissolving the AAO template for with and without insulating tape respectively.

Table 2: The ratio of InSb nanowires (drop casted) after dissolving the AAO template with different conditions

AAO conditions	Atomic		Ratio
	In	Sb	In:Sb
AAO template with insulating tape	23.53	19.48	1.27:1
AAO template without insulating tape	35.20	26.70	1.4:1

The average length of InSb nanowires for AAO template that has insulating tape on the conductive layer is $2.3 \mu\text{m}$, while for AAO template without insulating tape is $5.6 \mu\text{m}$ due to the strong electrostatic force. Moreover, the average diameter of InSb nanowires is 112 nm in Figure 4 a), which is corresponding to the pore diameter of the top of AAO compared with the diameter of Figure 4 b), is 326.3 nm .

In addition, the rate of ionic mass transfer was controlled in nanosized space by motivating a type of natural convection around working electrode. The electrochemical handling of nanowire clusters utilizing an attractive or high gravity field is in progress (Konishi et al., 2003)

Conclusion

In summary, we had successfully synthesis InSb nanowires by template assisted electrochemical deposition with various conditions of conductive layer of AAO template using potentiostatic technique. The nanowires were deposited have a uniform diameter with having high aspect ratio. The length, diameter, and morphology of InSb nanowires are strongly influencing by using different conditions of conductive layer of AAO template. It was found that a smother side wall and right stoichiometry can be obtained from AAO template with insulating tape. On the other hand, longer nanowires with rougher surface were observed from AAO without insulating tape. Achievement, of good morphology and right stoichiometric for InSb nanowires that demonstrators are possible and very beneficial for future devices application.

Acknowledgement

The author would like to thank the Malaysia government for fund support through IPB (grant no.9457700). The laboratory facilities provided by Institutes of Advanced Technology and the department of physics and chemistry faculty of science University Putra Malaysia are also acknowledged.

References

- Fang, M., Han, N., Wang, F., Yang, Z., Yip, S., Dong, G., Hou, J., Ghueh, Y., and Ho, J. (2014) III-V Nanowires: Synthesis, Property Manipulations, and Device Applications. *Journal of Nanomaterials*.
- Gang, Yuan (2011). "Electronic Structure of In₂O₃ Nanowires Synthesized at Low Temperature." *22:272-76*.
- Gangloff, L., E. Minoux, K. B. K. Teo, P. Vincent, V. T. Semet, V. T. Binh, M. H. Yang, I. Y. Y. Bu, R. G. Lacerda, G. Pirio, J. P. Schnell, D. Pribat, D. G. Hasko, G. A. J. Amaratunga, W. I. Milne, and P. Legagneux (2004). "Self-Aligned, Gated Arrays of Individual Nanotube and Nanowire Emitters." *Nano Letters* 4(9):1575-79.
- Hnida, K., Justyna, M. and Grzegorz, D. S. (2013). "Template-Assisted Electrodeposition of Indium antimony Nanowires Comparison of Electrochemical Methods." *Applied Surface Science* 287. Elsevier B.V.: 252-56.
- Irshad, M. I., Ahmad, F., Mohamed, N. M., & Abdullah, M. Z. (2014). Preparation and structural characterization of template assisted electrodeposited copper nanowires. *International Journal of Electrochemical Science*, 9, 2548-2555.
- Irshad, M. I., Ahmad, F., Mohamed, N. M., & Abdullah, M. Z. (2014). Preparation and characterization of electrodeposited cobalt nanowires. *3rd International Conference of Fundamental and Applied Science*, 1621, 538-542.
- Konishi, Y., Motoyama, M., Matsushima, H., Fukunaka, Y., Ishii, R., & Ito, Y. (2003). Electrodeposition of Cu nanowire arrays with a template. *Journal of Electroanalytical Chemistry*, 559, 149-153.
- Kuo, C. H., Wu, J. M, Lin, S. J. and Chang, W. C. (2013). High Sensitivity of Middle-Wavelength Infrared Photodetectors Based on an Individual InSb Nanowire. *Nanoscale Research Letters* 8 (1). *Nanoscale Research Letters*: 327.
- Lu, Wei and Charles M. Lieber. (2006). "Semiconductor Nanowires." *Journal of physics*, R387-R406
- Sahu, S and Nanda, K. (2001) Nanostructure Semiconductors Physics and Applications. *Proceedings of the National Academy of Sciences*. 67, 103-130.
- Shafa, M., Akbar, S., Gao, L., Fakhar-e-Alam, M., & Wang, Z. M. (2016). Indium Antimonide Nanowires: Synthesis and Properties. *Nanoscale Research Letters*, 11(1), 1
- Singh, A, Algarni, Z and Philipose, U. (2017). Template-Assisted Electrochemical Synthesis of p-Type InSb Nanowires. *ECS Journal of Solid State Science and Technology*, 6 (5) 39-43.
- Singh, Joginder, Tarun Chandel, and P. Rajaram. (2015). "Structural , Morphological and Raman Studies of Pulse Electrosynthesised Indium Antimonide Thin Films." 30008:1-5.
- Sisman, I. (2011). *Template-assisted electrochemical synthesis of semiconductor nanowires*. In *Nanowires—Implementations and Applications* (pp. 41-58). InTech
- Takamura, Tsukasa et al. (2015). "Magnetic-Particle-Sensing Based Diagnostic Protocols and Applications." *Sensors (Switzerland)* 15(6):12983-98.
- Yang, P. Y. P. (2010). Semiconductor nanowires for energy conversion. *Nanoelectronics Conference (INEC), 2010 3rd International*, 527-546.
- Zhang, X., Yufeng, H., Guowen, M. and Lide, Z. (2005). Fabrication of Highly Ordered InSb Nanowire Arrays by Electrodeposition in Porous Anodic Alumina Membranes. *Journal of The Electrochemical Society* 152 (10): C664.
- Zhao, X., Seo, S.-K., Lee, U.-J., & Lee, K.-H. (2007). Controlled Electrochemical Dissolution of Anodic Aluminum Oxide for Preparation of Open-Through Pore Structures. *Journal of The Electrochemical Society*.

CHAPTER 6

CARBON NANOMATERIALS

Synthesis of carbon nanomaterials by chemical vapor deposition: Effect of catalyst

Yazid Yaakob, Mohammad Adib Hazan, Ellyanie Balqis Hasmuei, Mackinley Bujang Anak Guma, Mohamad Shuhazly Mamat, Mohamad Saufi Rosmi, Subash Sharma, and Masaki Tanemura

Abstract

Carbon nanomaterials (CNMs) such as carbon nanotubes (CNTs), carbon nanofibers (CNFs) and graphene attracts much attention owing to their outstanding properties for many potential applications. There are various techniques for synthesis of CNMs, and chemical vapour deposition (CVD) is one of the most popular method. Basically, catalysts were the key factor to synthesize those materials. It is necessary to understand the effect of the type of catalyst to the CNMs growth. For this purpose, different type of catalyst were employed for CNMs growth in the CVD process. Different type of catalyst : Nickel Oxide (NiO) and iron oxide (Fe_3O_4) powder, and copper (Cu) foil were used in this work. The CNMs characteristics were confirmed by high resolution transmission electron microscopy (HRTEM) and energy-dispersive x-ray spectroscopy (EDX). The results revealed that Fe_3O_4 produced higher yield of CNMs compared to NiO. The bigger size of catalyst (above 20 nm) result in no formation of CNTs while smaller size of catalyst (below 10 nm) produce CNTs. The bigger size of catalyst will result in encapsulated of metal carbide. Cu foil produced graphene film on the re-solidified Cu surface. Thus, selection of the type of catalyst are very crucial in order to produce desires type of CNMs.

Keywords: chemical vapor deposition; graphitization; carbon nanomaterials; catalyst

Introduction

Ever since the discovery of hollow carbon spheres in 1985, it trigger researchers to explore a new class of materials, namely carbon nanomaterials (Kroto,1985). Nowadays, these materials: carbon nanotubes (CNTs), carbon nanofibers (CNFs) and graphene have become one of the most attractive materials owing to their extraordinary properties and characteristics (Iijima, 1991; Novoselov, 2004). These material can be many time stronger than steel, harder than diamond, higher electrical conductivity than copper and so on. Therefore, many studies have attempted to identify the most efficient synthesis method of these materials, in order to satisfy the demand in green technology and nanotechnology field (Liu, 2014).

Chemical vapor deposition (CVD) are very popular techniques of producing CNMs. Compared to any other methods such as laser ablation and arc discharge, the CVD technique is considered to be more economical and simple process, which only require low temperature and ambient pressure. This method have advantages in term of the ability to produce high yield and purity of CNMs with low cost and consume less time. It also offer great control over CNMs growth parameters and can be produce from any state (solid, liquid, gas) of hydrocarbon precursor (Abdeladim,2011; Shinde,2014; Vlasiouk,2013). Basically, in CVD process, hydrocarbon precursor will be vaporized by thermal decomposition with an assistance of metal catalyst. The ability of those catalyst were related to its catalytic activity for the decomposition and diffusion of hydrocarbon precursor on the active site and the formation of hexagonal carbon, as well as the catalyst deactivation and the formation of meta-stable carbides. Typically, metal nanoparticles are required to enable hydrocarbon decomposition to occur at a lower temperature than

their spontaneous decomposition temperature. Most commonly-used transition metals are Fe, Co and Ni because of two main reasons: (i) high solubility of carbon in these metals at high temperatures; and (ii) high carbon diffusion rate in these metals (Dupuis, 2005). Besides that, high melting point and low equilibrium-vapor pressure of these metals offer a wide temperature window of CVD for a wide range of carbon precursors. Fe, Co, and Ni also have stronger adhesion with the growing CNTs compared to other transition, hence they are more efficient in forming high-curvature (low-diameter) CNTs such as SWCNTs.

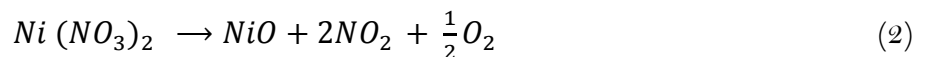
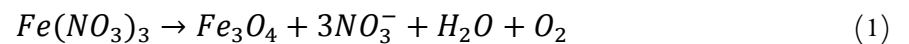
Apart from the popular transition metals, Cu, Au, Ag, Pt and Pd were also found to catalyze various hydrocarbons for CNTs growth (Takagi, 2006). Compared to transition metals, noble metals have lower carbon solubility hence have lower formation of CNT and not suitable as catalyst for higher yield formation of CNTs. However, if they are in small particle size (less than 5nm) has been found to be useful for CNTs growth. Therefore, these apparently different type of catalysts might share a common growth mechanism of CNMs, which is not yet clear. Hence this is an open field of research to correlate the catalyst's role to the CNMs growth.

Here we report a systematic study of the effect of Fe₃O₄, NiO and Cu on the growth of CNMs using simple chemical vapor deposition (CVD) system. The results clearly revealed that the morphology and microstructure of CNMs depended on the type of catalysts, which is promising for a controllable growth of various kinds of carbon nanostructures.

Materials and Methods

Sample preparation

Fe₃O₄ and NiO catalyst were prepared by using hydrolysis-oxidation reaction of iron nitrate salt (Fe(NO₃)₃) and nickel nitrate hexahydrate (Ni (NO₃)₂) • 6H₂O solution with the addition of ammonia solution (NH₄OH) until the formation of precipitate is completely formed. The precipitate is then being filtered and dried in an oven at temperature around 80 °C for 24 h to remove the water. After the dried process, the sample is crushed and grind into a fine powder. Then, the sample will go through a calcination process for 4 hours at 400 °C. The powders were fully oxidized to form Fe₃O₄ and NiO powder. The decomposition process is summarize by the equation (1) and (2).



Cu catalyst was prepared by using Cu foil (Nilaco Corp., purity 99.9%) with 20 μm thickness. The sample were annealed in an enclosed tube at 1100 °C for 60 min with flow of 100 sccm (standard cubic centimeter per minute) of hydrogen gas to form resolidified Cu.

Synthesis of CNMs

Fe₃O₄ and NiO was placed in the reaction chamber of the furnace in atmospheric pressure CVD (APCVD) system, respectively. The argon gas was flow for 15 minutes to expel all the contaminants. The system then heated to 400 °C within 30 min with 100 sccm of pure hydrogen gas to increase sample

crystallinity for carbon growth. Then, at temperature of 700 °C, methanol was introduced with the aid of argon gas into the reaction chamber. The reaction time for the carbon growth was set to 30 minutes.

For Cu case, Cu foil was placed into the reaction chamber of the furnace in low pressure CVD (LPCVD) system (Saufi, 2016). Magnetic boat containing chicken oil, which act as carbon precursor was placed near the opening of the inlet. The system was pumped down to a vacuum pressure of 2 Pa for 10 min, and then heated to 1080 °C within 120 min with 100 sccm of pure hydrogen gas. Then, the mixture of argon and hydrogen gas with a molar ratio of 98:2 sccm were introduced into the LPCVD system and the magnetic boat containing chicken oil was brought into the zone and placed at 5 cm away from the zone for the graphene growth at 1080 °C under pressure of 150 Pa for 60 min. After the synthesis process complete, the furnace was set to cool down until it reach room temperature.

The characterization of CNMs were performed by high resolution transmission electron microscopy (HRTEM : JEOL JEM 2100, operated at 200 kV) equipped with Energy Dispersive X-Ray Spectroscopy (EDS), Raman spectroscopy (NRS 3300 laser Raman spectrometer with a laser excitation wavelength of 532.08 nm), and UV-vis spectroscopy (ASCO V-670K spectrophotometer).

Results and Discussion

The yield of CNMs are differ from each sample. For Fe_3O_4 , the sample has a high percentage of yield, which is 71.6%. The mass of Fe_3O_4 was taken before synthesis and directly after CVD process ended. During the weighing process, the sample showed a significant increase in weight. The increasing mass after CVD process indicates that there are additional element, namely CNMs growth on the initial catalyst. On the other hand, for NiO, the percentage yield of the sample is in negative percentage, which is -8.65%. This indicates that the final mass of the sample is less than initial mass. There are a reason for some losses in mass of the sample. During the synthesis process, oxide element combine with hydrogen from methanol gas and carbon from methanol gas will deposit above nickel catalyst. Compare the weight of carbon and oxide, oxide has higher mass than carbon. When NiO lost the oxide element, the sample will become lighter than initial NiO. Only then carbon will grow above the nickel. The mass growth of carbon element added some mass to nickel catalyst but the losses mass from the oxide are much greater. Thus make the final mass of the sample reduce.

Different type of catalysts employed were highly effect the morphology and structural of the CNMs growth. The utmost appropriate method to analyse the composition of the samples is by using TEM. Figure 1 shows TEM observation results of the Fe_3O_4 sample. Carbon is clearly seen grow on the catalyst in Fig. 1a. High magnification of the image (Fig. 1b) shows a hollow structure of carbon nanotube (CNT). The average diameter of the CNT grow is around 12 nm average diameter hollow of CNT is around 2.5 nm.

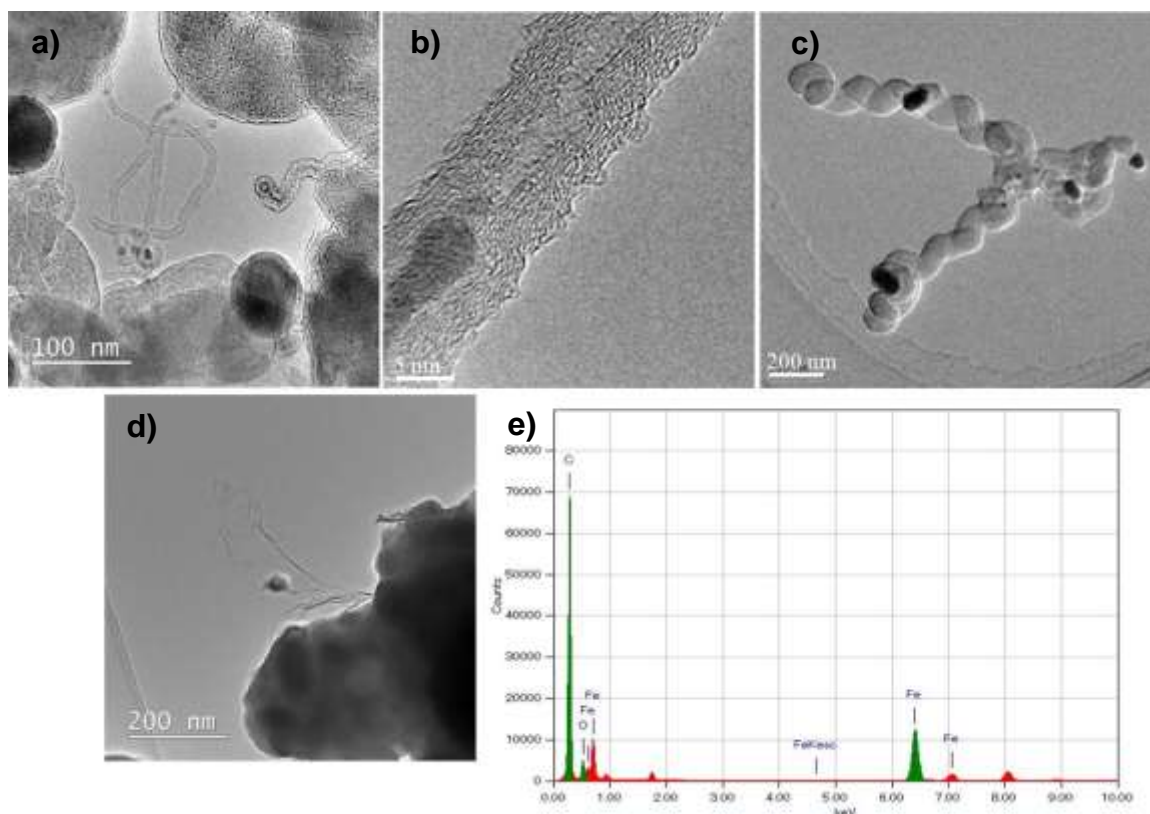


Figure 1: TEM image for CNMs growth using Fe_3O_4 as catalyst at 700°C .

Fig. 1a also shows that the size of the nanoparticles catalyst play an important role in synthesis CNTs. If the nanoparticles catalyst used is big around 50 nm, the carbon grow around the catalyst, make it encapsulate the nanoparticles catalyst. If the size of nanoparticles catalyst is small (10 nm), the CNT will be grow. It can be deduce that to grow CNT, the size of catalyst used must be in range of 10 nm. Catalysts with higher iron content exhibit larger metallic iron particles. This will lead to other forms of carbon structure such as carbon nanofiber or metal encapsulated graphitic carbon as shown in Fig. 1c and 1d, respectively. Therefore it appear that larger nanoparticles are unable to catalyze CNT growth (Dupuis, 2005). The corresponding EDX spectra in Fig. 1e confirmed that the sample contained carbon and iron elements.

Figure 2 show TEM observation results for NiO sample. Figure 2a show the carbon encapsulated NiO particle with 400 nm in diameter. Fig. 2b and 2c show the high magnification of the image, where there is graphitic structure layer spotted in range of 7 - 9 nm. The CNTs didn't grow on nickel might be due to the reaction temperature. The reaction temperature was not optimum for the CNTs growth. The growth of CNTs using nickel catalyst is more efficient at lower temperature that is in range of $500-600^\circ\text{C}$ (Allaedini, 2016). Yoshida et al. (2008) has identified the catalyst nanoparticle at the end of nanotubes to be Fe_3C starting from an iron catalyst. CNTs can grow above nickel nanoparticles catalyst same as iron because of the carbon solubility characteristic in both catalyst. The finite carbon solubility of 3d-metals in certain temperature ranges may play an important part in the growth process (Dai, 2002). Once the hydrocarbon molecules are broken, carbon atoms are believed to diffuse into the catalyst particle, this will lead to the growth of carbon atom above the nanoparticles of the catalyst. Nickel has higher carbon solubility compared to iron, so the result should show that NiO catalyst has the higher yield percentage compare to iron Fe_3O_4 . However, the result from the experiment contradict from the statement. One of the reason that lead to this result is due to the flow rate of the carbon source during synthesis on Fe_3O_4 , where a lot of graphite are grown compared to CNT.

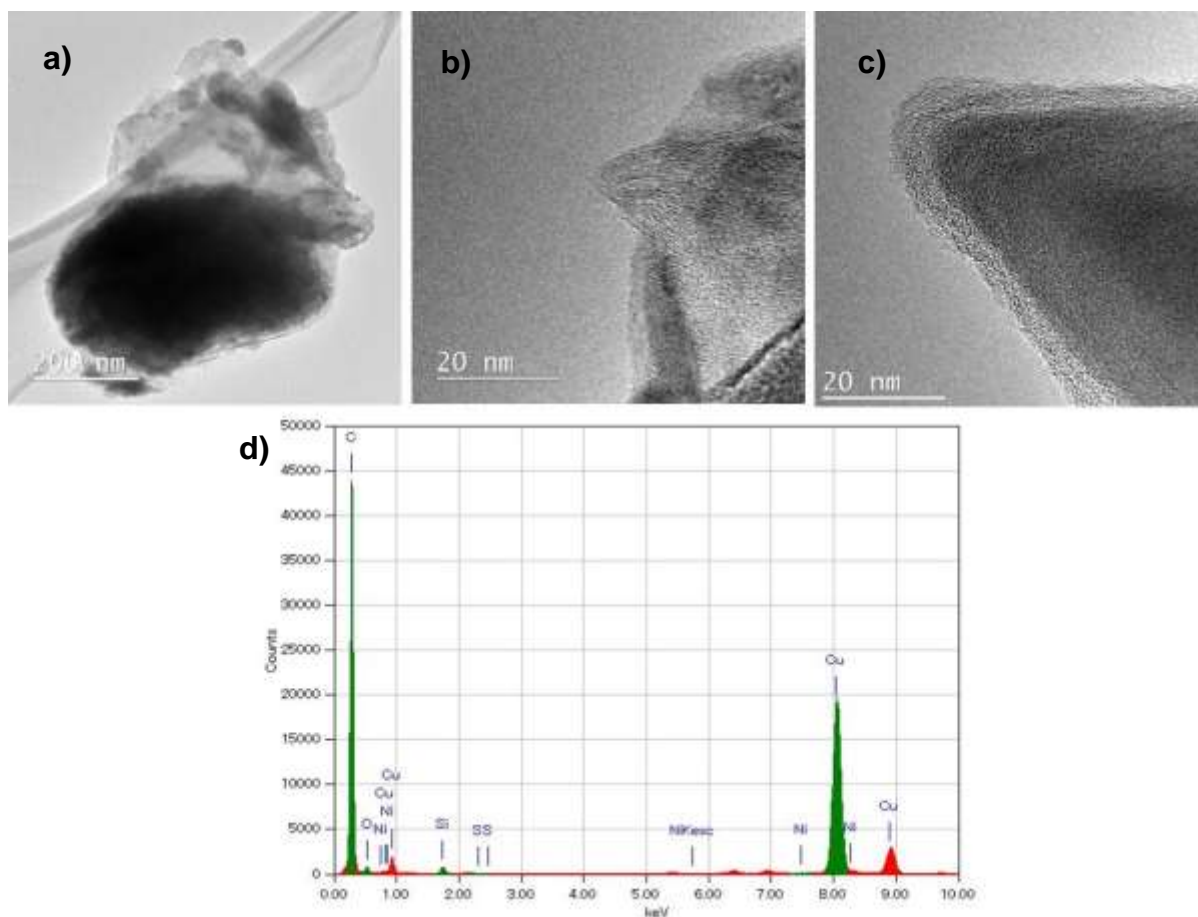


Figure 2: TEM image for CNMs growth using NiO as catalyst at 700°C.

Other reason that might related to no sign of CNT growth is due to the size of NiO nanoparticles. It can be observe in Fig. 2a that the particle size is over 100 nm. Therefore, CNTs cannot grow thus produce a carbon layer that wraps the catalyst (encapsulate). Figure 2d shows the corresponding EDX spectra, which confirmed that the sample contained carbon and nickel elements. Cu element peak detected due to the Cu grid that being employed for TEM observation.

Figure 3 shows different morphology and structural of the CNMs growth by using Cu foil as catalyst. In order to examine the graphene film, a Raman mapping over 90×90 mm² area was explored. Fig. 3b shows the Raman spectra of the graphene film on the Cu foil. An intense graphitic G and second order resonance 2D peaks are observed at 1584 and 2695 cm⁻¹, respectively, while there is no clear sign of defect related D peak. This indicates that the graphene produced on Cu foil catalyst have a good crystallinity. TEM images and selected area electron diffraction (SAED) pattern were observed to investigate the crystal structure of a monolayer graphene film. The graphene was transferred to a C-net TEM grid, where most of the area of graphene was determined to be crystalline by its hexagonal diffraction pattern (Fig. 3c) and was continuous as shown in Fig. 3a. The edge of graphene corresponds to monolayer graphene. The graphene film was transferred to a quartz substrate for UV-vis analysis. The graphene film exhibit transmittance of 87 % at 550 nm corresponds to the monolayer nature of graphene as shown in Fig. 3d. The graphene that synthesized in LPCVD using chicken oil, ethanol and methane prove that in the growth condition where carbon flux is low, self-limiting growth of graphene on Cu surface is independent of the precursor structure (Bhaviripudi, 2010). This is in contra with APCVD, wherea high pressure of precursor in APCVD will generates more active carbon atoms and reduces the effective diffusion length, resulting in more graphene nuclei to expand into a continuous

graphene sheet and increase in layer number (Jacobberger, 2013).

Conclusion

We have demonstrated the synthesis of CNMs via CVD using different type of catalysts. The dependence of the CNMs structures on the type of catalysts were investigated. Fe_3O_4 produced higher yield of CNMs compared to NiO. This is due larger particle size of NiO powder compare to Fe_3O_4 . Low surface area to volume ratio of NiO catalyst yielded inefficient, less uniform and instable catalytic activity. The bigger size of catalyst (above 20 nm) result in no formation of CNTs while smaller size of catalyst (below 10 nm) produce CNTs. The bigger size of catalyst will result in encapsulated of metal carbide. Cu foil, which have uniform and larger surface area than powder produced graphene film on the re-solidified Cu surface.

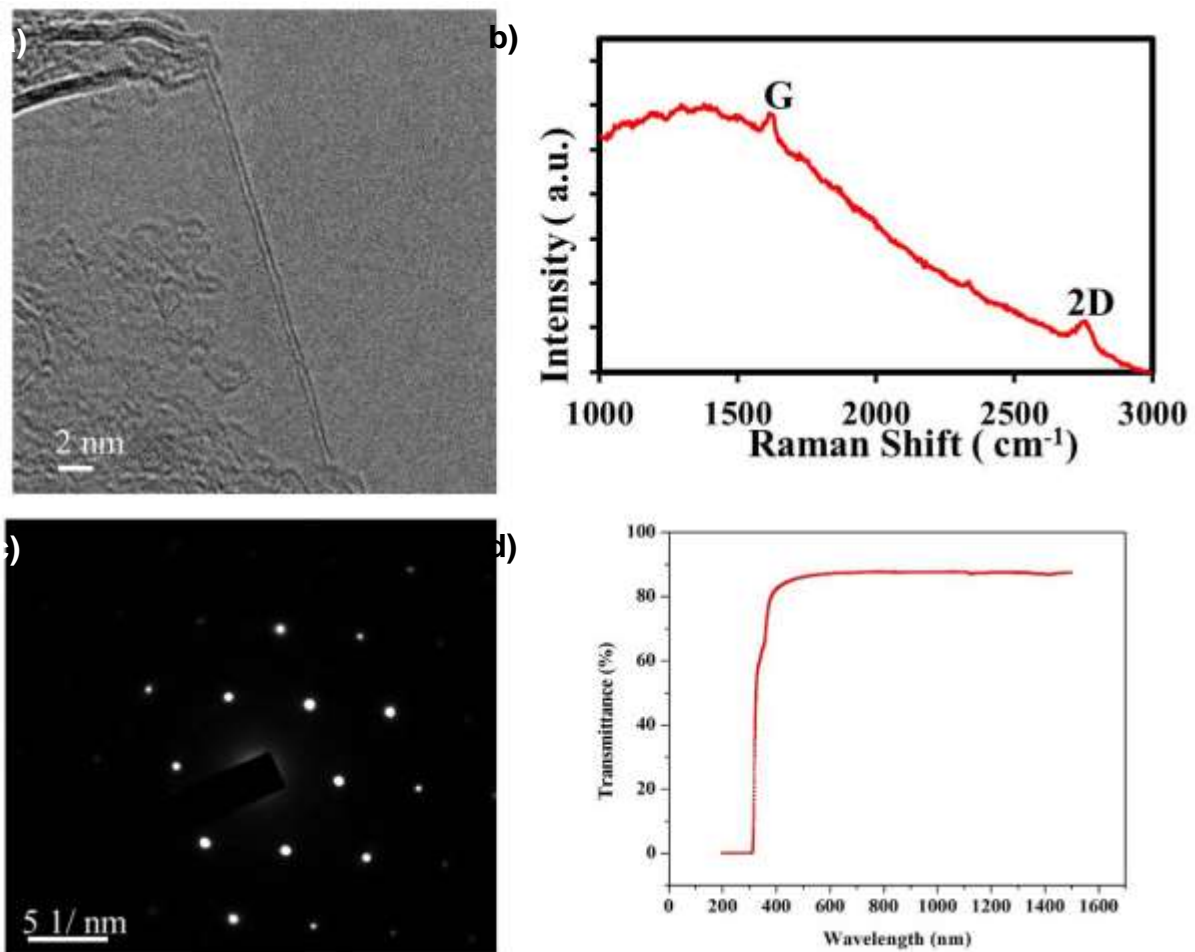


Figure 3: TEM image for CNT growth using NiO as catalyst at 700°C.

Acknowledgement

This work is partially supported by Fundamental Research Grant Scheme (FRGS) (UPM 5524809) from Malaysian Ministry of Education and Grant-in-Aid for Young Scientists (B) from Japan Society for the Promotion of Science (Grant No.15K21076).

References

- Abdeladim, G., Tarun, C., Filip, P., Shadi, S.S., Jonathan, G., & Helgi, S.S. (2011). Chemical vapor deposition synthesis of graphene on copper with methanol, ethanol, and propanol precursors, *Carbon*, 49, 4204–4210.
- Allaadini, G., Tasirin, S. M., Aminayi, P., Yaakob, Z., & Meortalib, M. Z. (2016). Carbon nanotubes via different catalysts and the important factors that affect their production: A review on catalyst preferences, *International Journal of Nano Dimension*, 7(3), 186–200.
- Bhaviripudi, S., Jia, X.T., Dresselhaus, M.S., & Kong, J. (2010) Role of kinetic factors in chemical vapor deposition synthesis of uniform large area graphene using copper catalyst, *Nano Letter*, 10, 4128–4133.
- Dai, H. (2002). Carbon Nanotubes : Synthesis , Integration , and Properties, *Accounts of Chemical Research*, 35(12), 1035–1044.
- Dupuis, A. C (2005). The catalyst in the CCVD of carbon nanotubes — a review, *Progress in Materials Science*, 50, 929–961.
- Iijima, S. Helical microtubules of graphitic carbon. *Nature*, 354, 56, 1991.
- Jacobberger, R.M., & Arnold, M.S. (2013). Graphene growth dynamics on epitaxial copper thin films, *Chemical Materials*, 25, 871–877.
- Kroto, H. W., Heath, J. R., O'brien, C., Curl, R. F., & Smalley, R. E. (1985). C₆₀: Buckminsterfullerene. *Nature*, 318, 162–163.
- Liu, W., Chai, S., Mohamed, A. R., & Hashim, U. (2014). Synthesis and characterization of graphene and carbon nanotubes: A review on the past and recent developments. *Journal of Industrial and Engineering Chemistry*, 20, 1171–1185.
- Novoselov, K. S., Geim, A. K., Morozov, S. V., Jiang, D., Zhang, Y., Dubonos, S. V., Grigorieva, V., & Firsov, A. A. (2004). Electric Field Effect in Atomically Thin Carbon Films, *Science*, 306, 666–669.
- Rosmi, M. S., Shinde, S. M., Rahman, N. D. A., Thangaraja, A., Sharma, S., Sharma, K. P., Yaakob, Y., Vishwakarma, R. K., Bakar, S. A., Kalita, G., Ohtani, H., & Tanemura, M. (2016). Synthesis of uniform monolayer graphene on re-solidified copper from waste chicken fat by low pressure chemical vapor deposition, *Materials Research Bulletin*, 83, 573–580.
- Shinde, S.M., Kalita, G., Sharma, S., Papon, R., Mohd Yusop, M.Z., & Tanemura, M. (2014). Synthesis of a three dimensional structure of vertically aligned carbon nanotubes and graphene from a single solid carbon source, *RSC Advances*, 4, 13355–13360.
- Takagi, D., Homma, Y., Hibino, H., Suzuki, S., & Kobayashi, Y. (2006). Single-Walled Carbon Nanotube Growth from Highly Activated Metal Nanoparticles. *Nano Letter*, 6, 2642–2645.
- Vlassiuk, I., Fulvio, P., Meyer, H., Lavrik, N., Dai, S., & Datskos, P. (2013). Large scale atmospheric pressure chemical vapor deposition of graphene, *Carbon*, 54, 58–67.
- Yoshida, H., Takeda, S., Uchiyama, T., Kohno, H., & Homma, Y. (2008). Atomic-scale in situ observation of carbon nanotube growth from solid state iron carbide nanoparticles. *Nano Letter*, 8(7):2082–2086.

CHAPTER 7

SURFACE AND COATING TECHNOLOGY

Effects of PTFE coating on the Stainless Steel Surface for the Reduction of Powder Stickiness during Spray Drying Process

Nadiyah Ramlan, Mohamad Yusof Maskat, Saiful Irwan Zubairi

Abstract

Spray-drying is the liquid food drying method where stickiness and wall deposition has most commonly been a major issue. For that reason, the efficacy of chemical surface coating was introduced to reduce stickiness and improve product recovery. The stainless steel (SS) plate used to mimic wall of drying chamber, coated with liquid polytetrafluoroethylene (PTFE) to increase its hydrophobicity. The hydrophobicity and morphological properties were determined by means of goniometer, SEM and EDX respectively. From the results obtained, the exposure of PTFE on SS has reduced significantly the powder stickiness ($p < 0.05$). Moreover, the treated SS shows higher contact angle than the untreated one ($p < 0.05$). In fact, the SEM images of the treated SS showed rough surfaces as to indicate its hydrophobicity shifting. The surface roughness will reflect the value of contact angle where hydrophobic surface is rougher compare to hydrophilic surface. In summary, we reported that a simple surface modification using PTFE on the SS slide has successfully proven to be one of the potential approaches to reduce the powder stickiness on the wall of spray dryer.

Keywords: spray drying, stainless steel, PTFE coating, contact angle, hydrophobicity, stickiness

Introduction

Drying is a process commonly used in food preservation to reduce the moisture content in the food system. In general, food systems which contain a low level of water activity have a longer shelf life. Dehydration by spray drying is used in the wide range of products in food industries to produce dry powders and agglomerates (Phisut, 2012). By decreasing water content and water activity, spray-drying is used in food industry to ensure a microbiological stability of products, avoid the risk of chemical and/or biological degradations, reduce the storage and transport costs, and finally obtain a product with specific properties (Gharsallaoui et al., 2007).

Stickiness has most been recognized commonly as a major issue in operation of spray drying that indirectly affects the quality and quantity of the product. The powder may deposit on the wall or blockage may occur in the duct or cyclone (Bhandari & Howes, 2005). For that reason, the development of wall deposition deteriorates the yield of the products and hence increases the costs of manufacturing and maintenance (Keshani et al., 2015). The degree of wall deposition is affected by several factors including operating parameters, type and size of spray dryer and the spray dryer wall properties. The properties of the wall of the dryer in which deposition occurs also play a significant role in the mechanism of product deposition. Moreover, it is well known that the adhesion of liquids onto walls depends on the wall properties (Bhandari & Howes, 2005).

Some available approaches to reduce the stickiness problem include process based (such as use of low temperature and low humidity air) and material science based (such as introducing of drying aids)

methods (Jayasundera et al., 2009). However, these approaches also have limitations in practice. For example, large amounts (often >35%) of drying aid (maltodextrin) are required to convert sugar-rich fruit juices into a powder form (Bhandari et al., 1993). Addition of such large amounts of drying aids increases the cost and may alter the original flavour and taste of the product, and risks consumer disapproval. An alternative and novel way to minimize the stickiness problem is to modify the surface properties of the drying chamber and cyclone of the spray dryer.

The work described in this paper is motivated by a search for new surface material for industrial spray drying equipment. The material should have hydrophobic properties, chemically inert, easy to clean yet have high temperature resistant. Polytetrafluoroethylene (PTFE) is chemically very inert and has a relatively high melting point (325°C). PTFE also has non-stick property due to its low surface energy. Its coefficient of friction (0.05) is lower than that of almost any other polymer. This research is attempted to increase the efficiency of spray dryer by reducing its product stickiness through chemical surface treatment such as PTFE on the SS surface of drying chamber and cyclone of spray dryer.

Materials and Methods

Materials

Polytetrafluoroethylene (PTFE) preparation 60 wt% dispersion in H₂O. Full cream milk (Dutch Lady) was obtained from nearby supermarket. Stainless steel 316 plate (25mm x 25mm x 1.2mm) was acquired from Ikhlas Resmi (M) Sdn. Bhd.

Methods

1. PTFE coating process on the stainless steel plate

The coating process was done by applying method from (Van Der Wal & Steiner 2007) with slight modification. The substrates were microscopy stainless steel plate, cut to 25 mm x 25 mm x 1.2 mm squares. The suspension was applied to the substrate by using spread coating method. The 60% solution was spread-coated by moving a sharp blade across a drop of suspension on the substrate. After coating, the sample was transferred to a hot-plate set to 120°C C to let the water evaporate. The temperature was then raised to 290°C for 5 minutes.

2. Spray Drying Process

The SS plate was weighed before and after drying process to determine the weight of powder adhered on the SS plate. Oven drying method was used to determine the flux adhesion weight on the SS plate. Oven drying process was used to resemble the spray drying process. Firstly, all slides were put in the oven (180°C) for 10 minutes before vertically sprayed with 0.5ml of commercially available liquid milk. The temperature of 180°C was used to resemble the normal temperature of spray drying process. After 2 minutes drying, all the plates were cooled in the room temperature before weighed. The weight of the slides before and after the drying process was measured (n = 3) using an analytical balance. After that, the flux adhesion weight between the treated and untreated plates were calculated using the following equation:

Flux adhesion weight = weight of SS plate after drying – weight of SS plate before drying

3. Contact angle measurements

The surface wettability was determined by water droplet contact angle measurements. The measurement was taken on the SS plate which act as a mimic to the spray dryer chamber. The SS plate were treated with different concentration of PTFE and were compared for contact angle value. Static

contact angle measurement was recorded and analysed for 3 replications (n=3) at room temperature on Automated Contact Angle Goniometer (model 100) from Rame-Hart Inc. with Western Vision software.

4. Structure Analysis and Morphology: Scanning Electron Microscope (SEM)

The surface morphology of SS plate treated with PTFE was determined by means of microscopy. The sample was attached to the stub of the aluminium and was coated with gold in an argon environment. Then the sample was analyzed using Scanning Electron Microscope (SEM) with the magnification of 5K to 10K times.

5. Determining Thermal Stability of The PTFE coated SS

The treated SS plate was exposed to spray drying normal temperature (180°C) in the oven for 30 minutes, the time used to spray dry 10ml of milk using pilot scale spray dryer. Then the plate was analysed for contact angle after cooled in dessicator. These processes were repeated until 12 cycles.

6. Statistical analysis

Data analysis was performed using SPSS for Windows, version 20.0 (SPSS Inc., Chicago, IL, USA). The data were analysed by analysis of variance (ANOVA) method and the differences between means were determined, at 5% significance different ($p < 0.05$). Mean values obtained for each analyses studied on the different samples were compared by One-Way ANOVA (Tukey's multiple comparison) and independent t-Test.

Results and Discussion

1. Powder Stickiness and efficacy of PTFE surface treatment on SS Plate

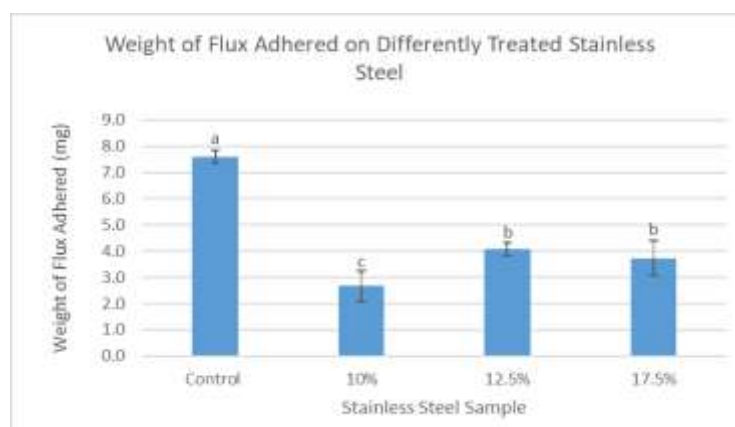


Figure 1: Weight of flux deposited on differently treated SS plate.

PTFE is well known for its non-stick properties for various applications due to the presence of high bonding energy of carbon and fluorine. This results in an inert surface chemistry. The PTFE solution were deposited by spread coating method on the SS plate. Figure 1 shows the weight of flux adhesion

of non-coated SS plate (control) and SS coated with different PTFE concentration (10%, 12.5%, 17.5%). 0.5ml liquid milk sample was sprayed on the plate during drying process at 180°C. The adhesion flux was calculated from the weight difference of SS before and after the drying process. It can be observed that the usage of PTFE at 10%, 12.5%, and 17.5% had successfully reduced the weight of flux deposited as compared to non-coated SS ($p < 0.05$). Such observation is in agreement with the findings obtained by Woo et al. (2009), where usage of Teflon resulted with less deposit when compared to untreated SS. Relatively high drying temperature in this experiment caused the particle-plate rubbery due to the induction of immobile liquid bridges (Woo et al. 2009). The reduction in deposition was more significant at higher temperatures when the particles become rubbery (Keshani et al, 2013). Therefore, a reduction in deposition flux was observed at this temperature. In spray drying, dry particles may become charged by friction with the walls of the equipment. Charged particles may stay and adhere to the walls of spray dryers by electrostatic forces (Ozmen & Langrish, 2003).

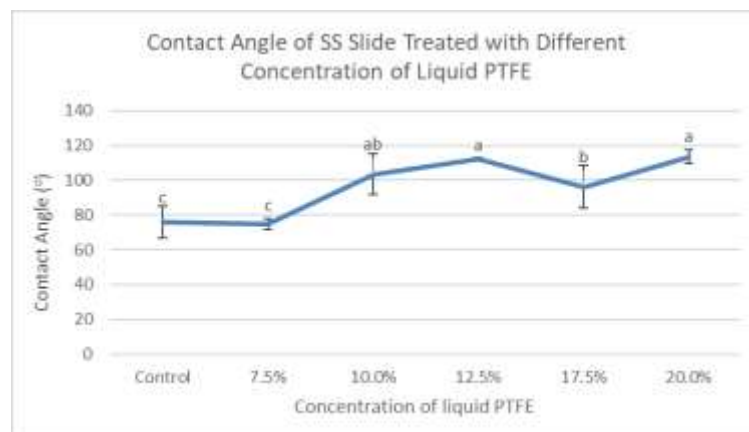


Figure 2: Contact angle of SS plate treated with different concentration of liquid PTFE.

Measuring the contact angle is a simple method to evaluate the level of wettability. The static (equilibrium) contact angles of sessile drops of liquids on both substrates were measured as a function of time with a goniometer. The results of the measured static contact angles are presented in Figure 2. From the results in Figure 2, it is clearly seen that the PTFE is adequate to increase the contact angle of the stainless steel plate ($p < 0.05$). While differences were not statistically significant, it was observed that contact angles increased from untreated slide to the treated one (7.5%). For each different concentration except 7.5%, contact angles were higher on treated stainless steel than untreated sample, as expected ($p < 0.05$). This high contact angle is important to reduce powder stickiness on the wall of drying chamber. In general, the hydrophobicity of modified surface increase with higher contact angle. It was reported that the water contact angle of a typical hydrophobic surface was approximately 65° to 95° (Wade et al., 1991). Small contact angles ($\leq 90^\circ$) also correspond to high wettability, while large contact angles ($\geq 90^\circ$) correspond to low wettability (Yuan & Lee, 2013). Such results are in agreement with the previous work done by (Woo et al, 2009) in which surface energy manipulation through the usage of PTFE plate during spray dryer showed clear difference in term of deposit strength compared to stainless steel plate. The PTFE plate recorded up to 70% powder removal, while stainless steel only 30%. The untreated surface is covered with large number of terminal hydroxyl groups. This group is the most common sites for hydrogen bonding and leading to hydrophilic surface (Mahadik et al., 2010). These findings show that a change in chemistry of the surface using PTFE coating technique can lead to change in SS wettability and increase the contact angle of the SS.

2. Structure Analysis and Morphology: Scanning Electron Microscope (SEM) and Energy Dispersive X-ray Analysis (EDX)

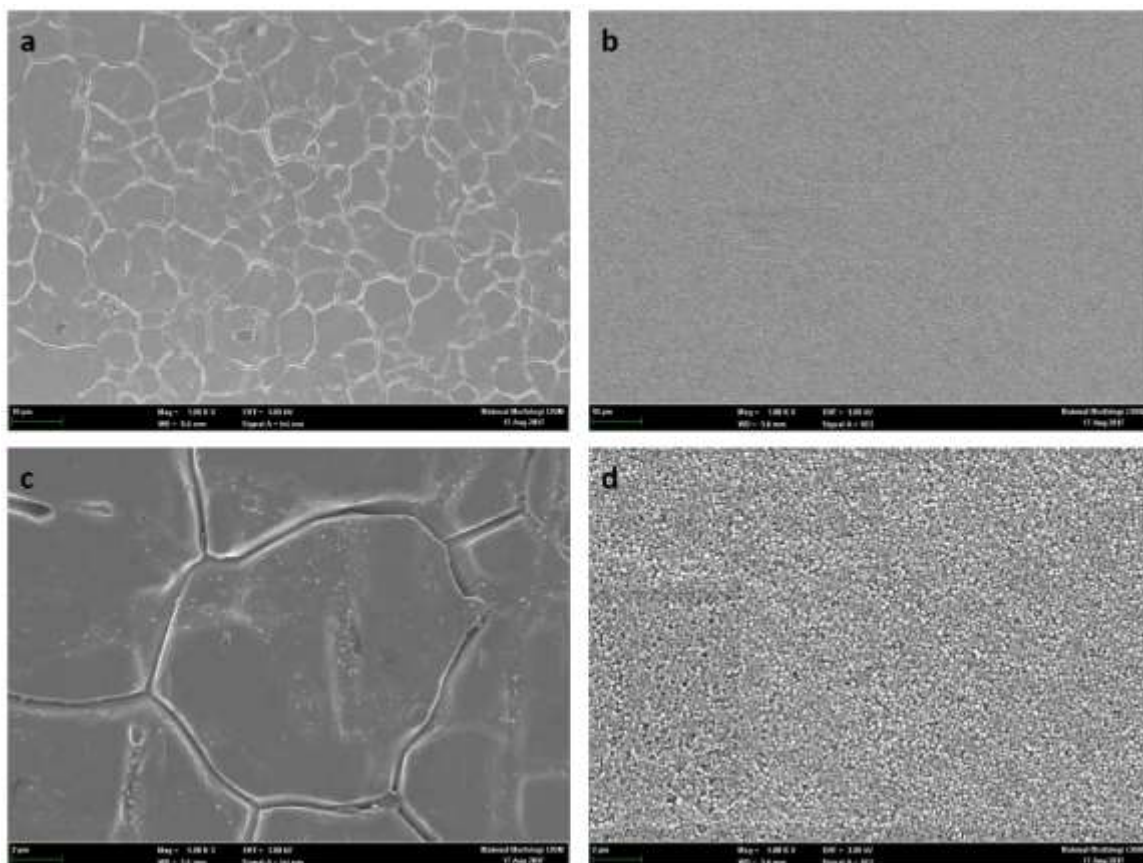


Figure 3: SEM images for untreated slide (a and c) and slide treated with 7.5% liquid PTFE (b and d) with different magnification (a)(b) 1K x; (c)(d) 50K x.

In order to observe the physical changes on the treated glass surface with respect to contact angle analysis, topography of the substrate surface was 100apour100d by SEM technique. Surface roughness or physical structure was one of the most important factors of the hydrophobicity like a lotus effect (Bhushan & Jung, 2011). The PTFE coating masked all surface characteristic of the stainless steel plate. After the deposition of the PTFE a moderate increase of roughness from Figure 3a to 3b (1K magnification) and from 3c to 3d (5K magnification) give rise to the increase in contact angle values thus producing a hydrophobic surface. This hydrophobicity increases with the increase of surface roughness, leading to a surface on which drops of water assume a nearly spherical shape (Van Der Wal & Steiner, 2007). Because of a reduced adhesion of any material to such surface, contaminants adhere preferentially to the water drop and thereby effectively removed from the surface (Van Der Wal & Steiner, 2007). These results are in agreement with (Santos et al, 2004) the only modification that significantly changes the morphology of the stainless steel is the Ni-P-PTFE coating compared to other surface modification technique (SiF^{+}_3 and MoS^{2+}_2 ion implantation; diamond-like carbon (DLC) sputtering; DLC, DLC-Si-O and SiO_x plasma enhanced chemical 100apour deposition (PECVD); and silica coating). Topographical SEM images of the treated surface showed that the coating process has been able to create uniform nanostructure particles on the SS surface.

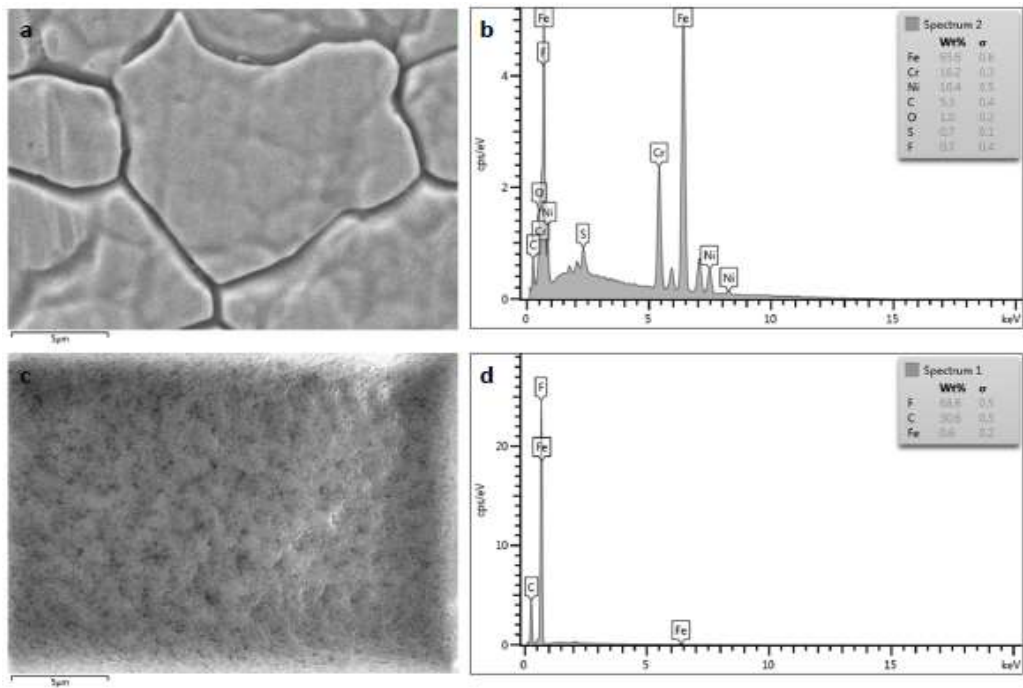


Figure 4: Elemental composition of untreated SS (b) and treated SS plate (d)

The EDX analysis used in this investigation gave a quantitative element composition analysis. Figure 4 shows the elemental compositions of the untreated stainless steel and treated stainless steel with 7.5% PTFE in the solution. EDX analysis results show the presence of high fluorine percentage in elemental compounds of the treated stainless steel (68.8%) as compared to non-treated one (0.7%), which is a verification of the existence and deposition of fluorocarbon polymer film on the sample surface.

3. Thermal Stability of Treated Stainless Steel

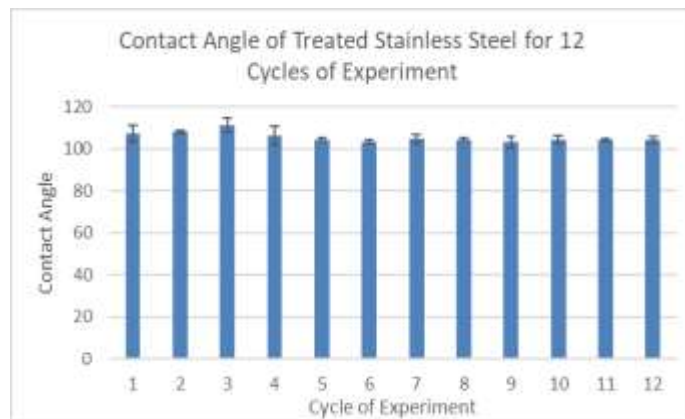


Figure 5: Contact angle of Treated SS plate for 12 cycles of experiment.

The treated SS was exposed to 180°C oven drying for 30 minutes each cycle repeated until 12 cycles to investigate the effect of spray drying temperature on PTFE coating. From Figure 5, a clear maintained contact angle of the PTFE treated SS can be seen from the graph for 12 cycles. The coated SS sustained its contact angle above 100°C even exposed to high drying temperature repeatedly. This finding proved that the PTFE coating is not affected by the temperature used during spray drying. This is because PTFE generally has a high melting point (approximately 327°C). The crystalline or partially crystalline PTFE structure will undergo several phase transitions from sub-ambient temperatures up to the

melting point, at atmospheric pressures (Villani, 1990). Below 19°C, a well-ordered hexagonal crystal structure is obtained. When heated to higher temperatures, the crystalline PTFE turns into a partially ordered hexagonal phase. Above 30°C, the material converts into a disordered phase pseudo-hexagonal. This phase is stable until the material reaches the melting region around 330°C (Blumm et al, 2010). This finding is similar to the previous research where PTFE polymers maintained its wetting behaviour, even at high temperature (200°C) the polymer maintain a high contact angle with the oil (Ashokkumar et al., 2012).

Conclusion

In this work, we evaluated the influence of PTFE coating on hydrophobicity of wall of spray dryer chamber. The PTFE modification significantly increased the hydrophobicity of the SS surface and reduced the weight of flux adhered on the SS plate ($p < 0.05$). In order to observe the efficacy of the chemical used on the glass chamber hydrophobicity, contact angle value was compared between the treated and untreated plate. It has shown that the chemical used were significantly increased the contact angle for all treated plate at concentration 10%, 12.5%, 17.5%, 20% as compared to untreated one ($p < 0.05$). The hydrophobicity changes on the treated SS plate were indicated by the SEM and EDX analysis on the SS plate. The SEM results showed that the chemical used was effectively increased the roughness of the SS and proved with high fluorine content from EDX analysis. The coating also was thermally stable and the hydrophobicity was maintained even after twelve cycle of drying process.

Acknowledgement

The authors would like to thank the National University of Malaysia, (GGPM-078-2013), Ministry of Higher Education (MOHE) (FRGS/2/2013/TK04/UKM/03/1; PPRN-2015-017; PPRN-2015-018; PPRN-2015-021) and Ministry of Science, Technology and Innovation (MOSTI) (06-01-02-SF1271) and for providing financial support to this project.

References

1. Ashokkumar, S., Nissen, J.A., Møller, P. (2012). Factors Affecting the Wettability of Different Surface Materials with Vegetable Oil at High Temperatures and Its Relation to Cleanability. *Applied Surface Science*, 263, 86-94.
2. Bhandari, B. & Howes, T. (2005). Relating the Stickiness Property of Foods Undergoing Drying and Dried Products to Their Surface Energetics. *Drying Technology*, 23, 781-797.
3. Bhushan, B. & Jung, Y.C. (2011). Natural and Biomimetic Artificial Surfaces for Superhydrophobicity, Self-Cleaning, Low Adhesion, and Drag Reduction. *Progress in Materials Science*, 56, 1-108.
4. Bhandari, B., Senoussi, A., Dumoulin, E., and Lebert, A. (1993). Spray Drying of Concentrated Fruit Juices. *Drying Technology*, 11, 1081-1092.
5. Blumm, J., Lindemann, A., Meyer, M., Strasser, C. (2010). Characterization of PTFE Using Advanced Thermal Analysis Techniques. *International Journal of Thermophysics*, 31, 1919-1927.
6. Gharsallaoui, A., Roudaut, G., Chambin, O., Voilley, A., and Saurel, R. (2007). Applications of Spray-Drying in Microencapsulation of Food Ingredients: An Overview. *Food Research International*, 40, 1107-1121.

7. Jayasundera, M., Adhikari, B., Aldred, P., and Ghandi, A. (2009). Surface Modification of Spray Dried Food and Emulsion Powders with Surface-Active Proteins: A Review. *Journal of Food Engineering*, 93, 266-277.
8. Keshani, S., Daud, W.R.W., Nourouzi, M., Namvar, F., and Ghasemi, M. (2015). Spray Drying: An Overview on Wall Deposition, Process and Modeling. *Journal of Food Engineering*, 146, 152-162.
9. Keshani, S., Daud, W.R.W., Woo, M.W., Nourouzi, M.M., Talib, M.Z.M., Chuah, A.L., Russly, A.R. (2013). Reducing the Deposition of Fat and Protein Covered Particles with Low Energy Surfaces. *Journal of Food Engineering*, 116, 737-748.
10. Mahadik, S.A., Kavale, M.S., Mukherjee, S., and Rao, A.V. (2010). Transparent Superhydrophobic Silica Coatings on Glass by Sol-Gel Method. *Applied Surface Science*, 257, 333-339.
11. Ozmen, L. & Langrish, T.A.G. (2003). An Experimental Investigation of the Wall Deposition of Milk Powder in a Pilot-Scale Spray Dryer. *Drying Technology*, 21, 1253-1272.
12. Phisut, N. (2012). Spray Drying Technique of Fruit Juice Powder: Some Factors Influencing the Properties of Product. *International Food Research Journal*, 19, 1297-1306.
13. Santos, O., Nylander, T., Rosmaninho, R., Rizzo, G., Yiantsios, S., Andritsos, N., Karabelas, A., Steinhagen, H.M., Melo, L., Petermann, L.B., Gabet, C., Braem, A., Trägårdh, C., Paulsson, M. (2004). Modified Stainless Steel Surfaces Targeted to Reduce Fouling-Surface Characterization. *Journal of Food Engineering*, 64, 63-79.
14. Van Der Wal, P., & Steiner, U. (2007). Super-Hydrophobic Surfaces Made from Teflon. *Soft Matter*, 3, 426-429.
15. Villani, V. (1990) A Study on the Thermal Behaviour and Structural Characteristics of Polytetrafluoroethylene. *Thermochimica Acta*, 162, 189-193.
16. Wade, W.L., Mammone, R.J., and Binder, M. (1991). Surface Properties of Commercial Polymer Films Following Various Gas Plasma Treatments. *Journal of Applied Polymer Science*, 43, 1589-1591.
17. Woo, M.W., Daud, W.R.W., Tasirin, S.M., and Talib, M.Z.M. (2009). Controlling Food Powder Deposition in Spray Dryers: Wall Surface Energy Manipulation as an Alternative. *Journal of Food Engineering*, 94, 192-198.
18. Yuan, Y., Lee, T.R. (2013). Contact Angle and Wetting Properties. In: Bracco, G., Holst, B. (Eds.), *Surface Science Techniques* (pp. 1-33). Berlin, Heidelberg: Springer.

CHAPTER 8

WLAN POSITIONING SYSTEM

WLAN Positioning Based on Enhanced k-Nearest Neighbour Classifier

Mohd Amiruddin Abd Rahman and Zulkifly Abbas

Abstract

This paper proposes a different type of kNN algorithm for positioning in $WLAN$ deployment area based on statistical learning – the multi-class kNN classifier. The principle of kNN classifier is based on statistical learning classification analysis and the nearest distance calculation is made for each pairwise AP signals. The classifier is further enhanced by considering multiple nearest RSS distance to obtain optimal location. The location decision is made based on majority voting of the chosen locations. The proposed algorithm is tested in realistic $WLAN$ environment. The algorithm is evaluated with classical kNN and maximum likelihood algorithm shows improvement of the mean localization error up to 23.1%. The algorithm is also efficient in different $WLAN$ environment conditions such as in reduced number of fingerprint samples and lower number of access points.

Keywords: Localization, Indoor positioning, $WLAN$, k -Nearest Neighbor (kNN)

Introduction

Wireless local area network (WLAN) positioning is still an interesting research topic to be explored. Despite introduction of personalized sensor type to help indoor positioning and navigation such as inertial sensor [1], gyroscope [2], and Li-Fi [3], WLAN is still a viable solution because it has been widely deployed in indoor environments. The most promising method of WLAN positioning is based on fingerprinting technique. The steps involved in fingerprinting method are offline and online phase. During the offline phase, surveyor with WLAN receiver equipped device measures received signal strength (RSS) of the access points at specified fingerprint measurement locations. The collected signals will be gathered to build the database called as radio map which could either be stored within the device itself or on a centralized server. During the online phase, the receiver inquires the location from the device or the server where computation of the location is made. The embedded algorithm computes the location estimates of the device location based on the most matched fingerprint location measured during the training phase.

The main objective to develop a positioning algorithm is to ensure it could give accurate estimation as possible. One of the most popular positioning algorithms based on WLAN fingerprinting is the k-Nearest Neighbor (kNN). In fact, the firstly developed WLAN positioning system implements kNN as the positioning algorithm. The kNN algorithm has been served as comparison algorithm to validate newly developed algorithm for indoor positioning. The main reason kNN is chosen is because its simplicity and flexible to work in any distribution of fingerprint data in WLAN environment. For example in a worst case condition where only one signal data is captured at any measured location, the location could still be estimated by the kNN algorithm. The k is referred to the number of nearest possible location based on set of nearest signal distance that is taken into account in calculating the estimated position of the device. The optimal value of k is decided by varying the number of possible location using a set of test sample data before it is implemented in online phase.

Lately, there has been research on WLAN positioning implementing statistical learning technique which includes support vector machines (SVM) techniques such as least square SVM [4], ILW-SVM [5], axial decoupled SVM [6], and neural networks such as back propagation [7]. It was found that the technique could outperform traditional positioning algorithms including kNN. Even though those algorithms could offer significant positioning accuracy improvement, they still require moderate amount of time to train the classifiers before positioning estimation could be done. For example, SVM technique requires training of support vectors and neural network needs to establish appropriate weighting function. To remove those training necessities, here we integrate the kNN computation within classification task of the statistical learning.

In this paper we introduce a novel approach of positioning with kNN algorithm. Unlike the traditional kNN technique which calculates the signal distance directly, we first map the RSS data on feature spaces following the statistical learning approach. A feature space contains information of RSS of pairwise combination of access points (AP). In theory, considering pairwise RSS vector would offer improved estimation compared to considering single RSS as in traditional kNN algorithm. The nearest signal distance is calculated according to nearness of those offline RSS vector pairwise to the online RSS vector of similar APs. Our approach also offers additional advantage compared to classical kNN where we could pre-select certain amount RSS vector to be considered in the computation which further mitigate the effect of noisy RSS data.

In the experiment, we evaluate the proposed algorithm by comparing with the traditional kNN algorithm and also another popular approach namely maximum likelihood (ML) [8]. Compared to those approaches, our algorithm offers superiority in terms of positioning accuracy where the mean positioning error is reduced up to 23.1% in the tested environment. We also show that the algorithm could also perform well in reduction of fingerprint offline samples and reduction of AP lists.

Methods

Multi-class kNN Classifier

In this work, a different approach to estimate the location based on principle of nearest neighbour estimation is proposed. Unlike the classical approach that considers only singular AP signal for calculating the neighbours, the proposed approach offers better choice of neighbours as the combination of signals of pairwise AP are considered during calculation of nearest neighbour. The online and offline signal vectors of pairwise APs are first transposed into a feature space and the distance between the pairwise signal vectors are calculated to determine the nearest signal neighbour. Since the classification of multi-class kNN (MkNN) is based on the theory of statistical learning, we briefly review the statistical learning classification in the first part of this section before describing the proposed multi-class kNN classifier.

The working principle in statistical learning classification is first extracting the data into feature space. The classification in general is done for two dimensional datasets. The top figure in Figure 1 shows the projection of fingerprint data in feature space for classification based on two different APs RSS dataset. A classifier needs to map an input data r to output y which is a category of prior data given $y \in \{1, 2, \dots, Y\}$ where Y is the total number of categories or classes. For $Y = 2$, the problem is solved by binary classification. For more than two classes, the problem becomes multiclass classification.

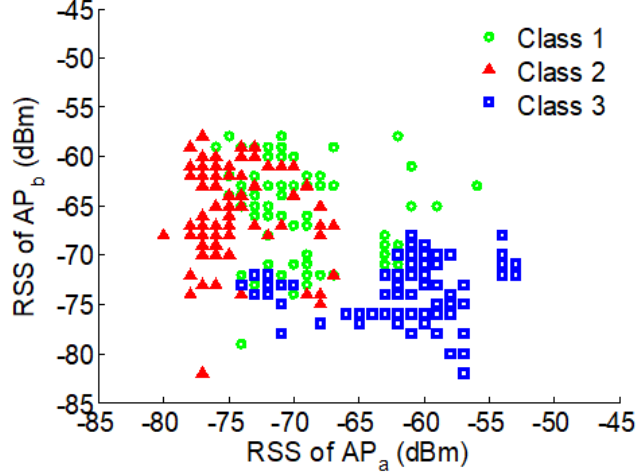


Figure 1. Projection of RSS fingerprint dataset into feature space for classification based on two different APs.

In indoor positioning, the problem is the multiclass classification because there are more than two fingerprint locations (classes). The fingerprint dataset should be represented as vectors of data according to each pairwise AP set. For L APs presents for a fingerprint dataset, the number of classification to be considered is $(L(L-1)/2)$. To solve the localization problem using classification, the fingerprint entries are reconstructed as AP pairwise dataset which its element is defined as follows:

$$\mathbf{A}_v(\mathbf{p}_i) \triangleq \left(\begin{bmatrix} r_i^{v_1}(1) \\ r_i^{v_2}(1) \end{bmatrix}; \quad \dots \quad ; \begin{bmatrix} r_i^{v_1}(\tau) \\ r_i^{v_2}(\tau) \end{bmatrix} \right) \quad (1)$$

where $(v = 1, \dots, \frac{V(V-1)}{2})$ and V is the total number of unique APs in the fingerprint database) is the pairwise AP combination index at location \mathbf{p}_i and τ is the number of matching pairwise signal over duration of the fingerprint collection time. Here, for non-matching pairwise signal, the signals are neglected and thus τ will vary according to available signal at every \mathbf{p}_i . The header of the new AP pairwise based-database could be defined as collection of similar group of pairwise AP at multiple locations given $\mathbf{A}_v = [\mathbf{A}_v(\mathbf{p}_1); \dots; \mathbf{A}_v(\mathbf{p}_I)]$ where I is the total number of fingerprint locations.

Since the kNN is an unsupervised classifier, the prediction of the location could be done by finding the nearest signal distance between the vector signals of the related pairwise AP. The distance of online sample to each data in each class for every online sample AP combination \mathbf{A}_β is defined as follows:

$$D_\beta(\psi_{\Theta u}) = \left\| \mathbf{r}_o^\beta - \mathbf{r}_i^\beta(\psi_{\Theta i}) \right\| \quad (2)$$

where $\psi_{\Theta i}$ is each data sample labelled Θ of class or location i , β is the number of matching pairwise APs, and $\mathbf{r}_i^\beta(\psi_{\Theta i}) \in \mathbf{r}_i^v$ is the signal vector of the data sample in the related class u .

In this work, the signal vector that contains the weakest signals is neglected and therefore the number of $\psi_{\Theta i}$ in different class may vary. The signal vector $\mathbf{r}_i^\beta(\psi_{\Theta i})$ could be visualised in Figure 2 as the red, green, and magenta circles that indicates signal vectors in three classes. The location could be estimated by taking the nearest data $\psi_{\Theta i}$ of each class i that gives the minimum $D_\beta(\psi_{\Theta i})$ is chosen where:

$$D_{\beta i} = \arg \min D_{\beta}(\psi_{\theta i}) \quad (3)$$

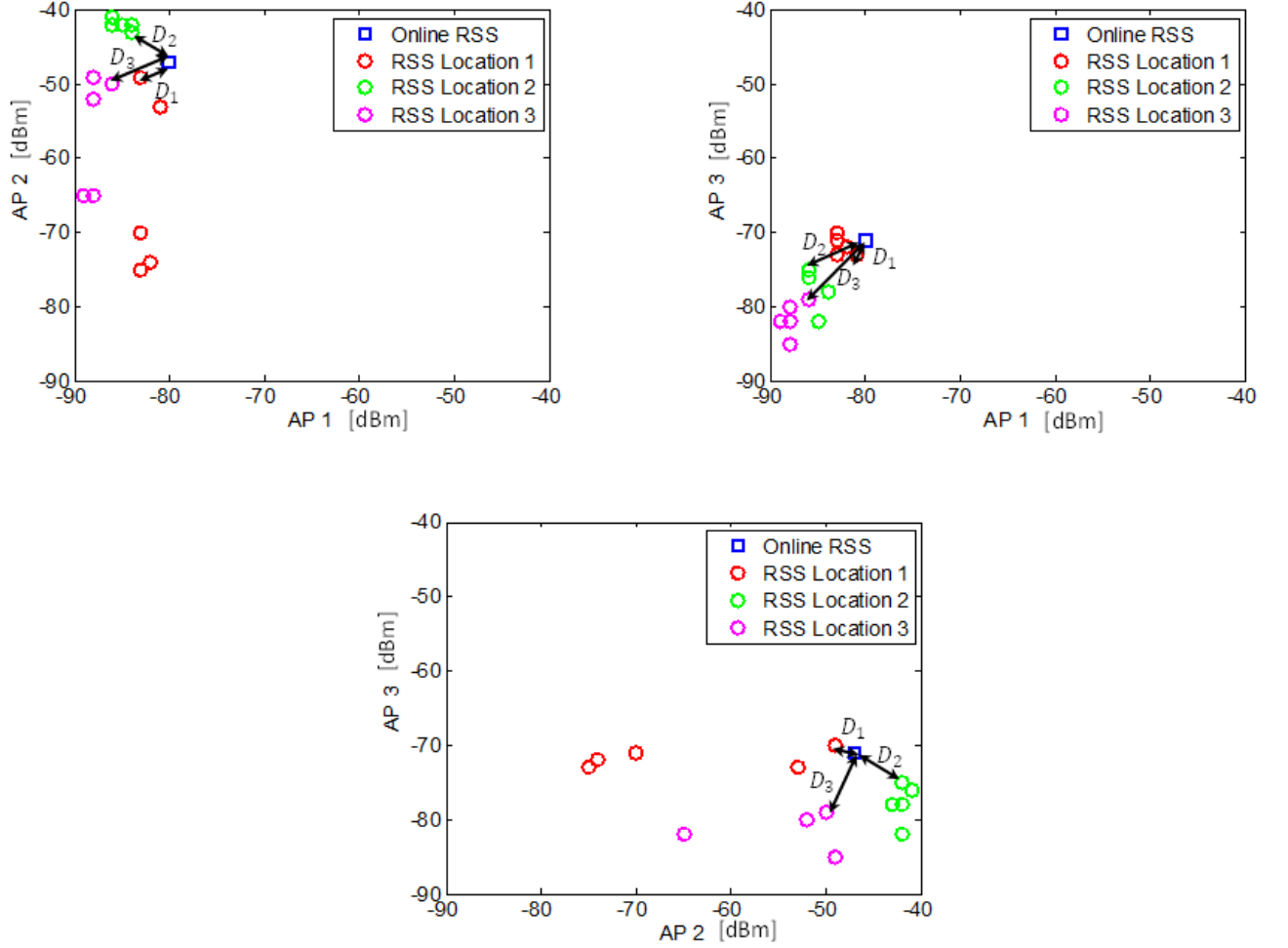


Figure 2: The kNN classifier for 3 AP case.

Since there are multiple combinations exists for each online sample \mathbf{A}_{β} , the decisive signal distance for every potential estimated class i is calculated as the average value of each class minimum distance for every online sample AP combination given as follows:

$$\Omega_i = \frac{1}{B} \sum_{\beta=1}^B D_{\beta i} \quad (4)$$

The distance Ω_i is sorted in ascending order and first k classes are used to determine the estimated class (location), $\hat{\mathbf{p}}$ which is calculated as follows:

$$\hat{\mathbf{p}} = \frac{1}{k} \sum_{k=1}^k \hat{\mathbf{p}}_k \quad (5)$$

Figure 2 shows the example of multiple multi-class k NN classification using 3 APs dataset. First the average distance of D_1 , D_2 , and D_3 for three AP combinations are computed. Next, the average distance is sorted in ascending order. If the required k is 2, the top two classes with lowest average distance are chosen and the estimated distance is the average class of the two classes (locations).

Measurement Setup

To evaluate the performance of the proposed technique, we carried out measurements of RSS in WLAN environment on the ground floor of an academic building in Universiti Putra Malaysia, Malaysia. The floor plan of the building is as shown in Figure 3. There are a total of 37 AP signals are detected during the measurement. The measurement was carried out using a Google Nexus 5 mobile phone which acts as the UE. The RSS samples were collected using Airplace Logger android app [15]. We collected 100 RSS measurements at each allocated offline fingerprint locations. The locations of the offline measurement are noted in Figure 3. There were a total of 102 locations which are separated within 2 m between each location. To test the algorithm, online samples were measured at different time and at distant locations from the offline location. The location of online samples is also depicted in Figure 3.

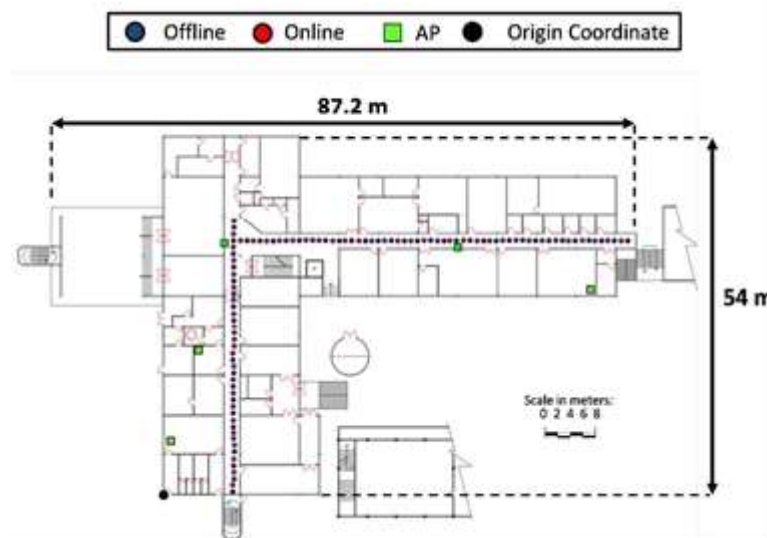


Figure 3. Floor plan where WLAN signals are measured.

Results and Discussion

To evaluate the performance of the proposed MkNN algorithm, the cumulative density function (CDF) of the distance error is plotted using as in Figure 4(a). We evaluate the performance of the proposed algorithm by comparing with the classical kNN using the best fixed k values for the environment which is 1. It is noted that the proposed algorithm performs better than the classical algorithms. It is also seen that the performance of MkNN is significantly improved compared to classical kNN. This shows that applying the signal distance based on pairwise AP signals could offer better location estimation compared to considering only singular AP signal information. Additionally, Table 1 shows detail result of performance of the localisation algorithms numerically. In the table, five error measures are depicted which are mean, standard deviation, median, 90% and 95% of CDF. It is found that the performance of normal kNN classifier is better than the classical kNN. At 90% of localisation error, the multi-class kNN classifier could obtain as high as 69.7% compared to existing algorithm. The mean error of normal multi-class kNN classifier is the lowest compared to classical kNN. The results presented in Figure 4(a) and Table 1 indicates classification of signal vectors of group of pairwise APs works better to discriminate information of fingerprint datasets at different locations thus giving good and robust location estimates. Moreover, the main advantage of the multiclass kNN classifier algorithm could be seen in terms of localisation accuracy within spacing of fingerprint location as plotted in Figure 4(b). The accuracy within fingerprint spacing is defined as percentage of estimated location errors within each fingerprint distance which is 2 m. This means the higher the percentage, the better algorithm performs. In all environments, the performance of multiclass kNN classifiers is better than kNN. It is

noted that the accuracy of the localisation within fingerprint spacing increases 36%, compared to the classical kNN. This shows that most of the classification works correctly using the proposed classifier to identify the nearest available location in the fingerprint dataset.

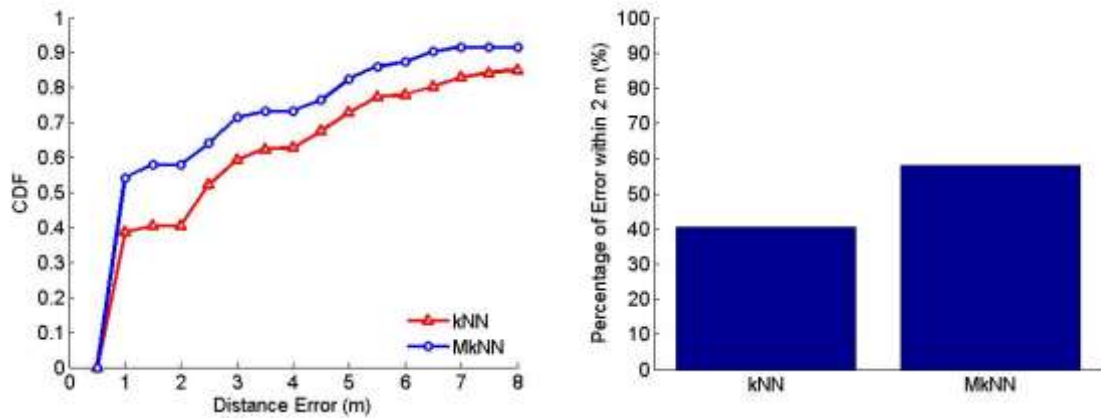


Figure 4. (a) CDF of mean errors of tested positioning algorithms, (b) Localisation accuracy within fingerprint spacing of kNN and MkNN.

Table 1. Error measures of different horizontal positioning algorithm

Algorithm	Error measures				
	Mean	Standard Deviation	Median	90% of CDF	95% of CDF
k Nearest Neighbour	3.9	3.7	2.3	9.0	11.0
Multi-class k NN classifier	3.0	3.6	1.0	6.1	11.0

Effect on Number of Fingerprint Measurement Samples

The performance of the MkNN algorithms is further analysed by varying the number of training sample in the radio map database. The aims of varying the number of trainings samples are twofold. First, to investigate if similar or better performance of the algorithm could be achieved by using different number of training samples. Second, to study at what range of number of training samples the performance of the proposed algorithms is better than existing algorithms. Figure 5 presents the mean error of every horizontal localisation algorithms at different number of training samples. The number of samples at each fingerprint location in the dataset is chosen between 4 to 100 samples at 4 sample interval. The implementation of the multi-class kNN classifiers as plotted in Figure 5 is observed. The MkNN algorithm has already outperformed classical kNN algorithm at 1w samples. This shows that lower sample number could be used to achived similar or better localisation accuracy based on the proposed algorithm.

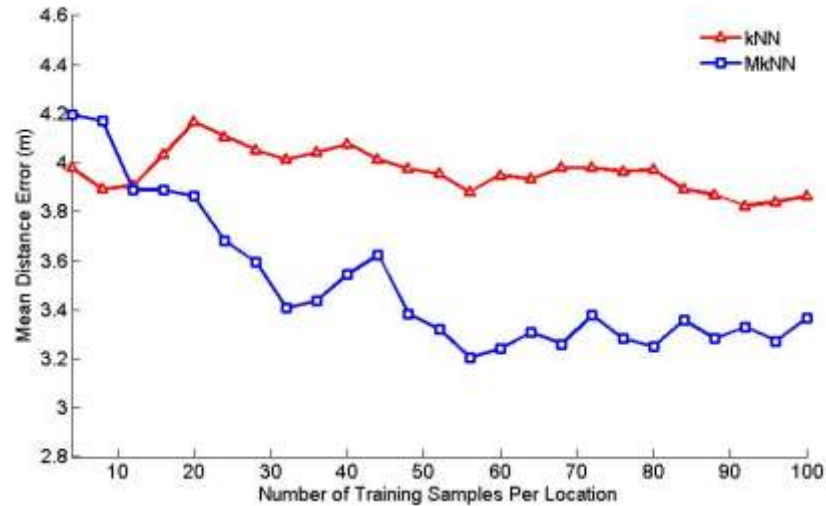


Figure 5. Effect of reducing the number of training samples.

Acknowledgement

The authors would like to thank Ministry of Higher Education Malaysia for funding this project under fundamental research grant scheme (FRGS) FRGS/1/2017/TK04/UPM/02/5.

References

1. Y. Liu, M. Dashti, M. A. A. Rahman, and J. Zhang, "Indoor localization using smartphone inertial sensors," in *Positioning, Navigation and Communication (WPNC), 2014 11th Workshop on*, 2014, pp. 1–6.
2. S.-E. Kim, Y. Kim, J. Yoon, and E. S. Kim, "Indoor positioning system using geomagnetic anomalies for smartphones," *Indoor Positioning and Indoor Navigation (IPIN), 2012 International Conference on*. pp. 1–5, 2012.
3. Q. Huang, Y. Zhang, Z. Ge, and C. Lu, "Refining Wi-Fi based indoor localization with Li-Fi assisted model calibration in smart buildings," *arXiv Prepr. arXiv1602.07399*, 2016.
4. L. Pei, J. Liu, R. Guinness, Y. Chen, H. Kuusniemi, and R. Chen, "Using LS- SVM based motion recognition for smartphone indoor wireless positioning," *Sensors*, vol. 12, no. 5, pp. 6155–6175, 2012.
5. YuFeng, JiangMinghua, LiangJing, QinXiao, HuMing, PengTao, and HuXinrong, "An Improved Indoor Localization of WiFiBased on Support Vector Machines," *Int. J. Futur. Gener. Commun. Netw.*, vol. 7, no. 5, pp. 191–206, 2014.
6. W. Yanhua, W. DongH, and Z. Yan, "Axial decoupled LS-SVMs for indoor positioning using RSS fingerprints," in *Control Conference (CCC), 2015 34th Chinese*, 2015, pp. 3920–3925.
7. R. S. Campos, L. Lovisolo, and M. L. R. de Campos, "Wi-Fi multi-floor indoor positioning considering architectural aspects and controlled computational complexity," *Expert Syst. Appl.*, vol. 41, no. 14, pp. 6211–6223, Oct. 2014.
8. T. Roos, P. Myllyma, H. Tirri, P. Misikangas, and J. Sieva, "A Probabilistic Approach to WLAN User Location Estimation," vol. 9, no. 3, 2002.

9. P. Bahl and V. N. Padmanabhan, "RADAR: an in-building RF-based user location and tracking system," *Proc. IEEE INFOCOM 2000. Conf. Comput. Commun. Ninet. Annu. Jt. Conf. IEEE Comput. Commun. Soc. (Cat. No.00CH37064)*, vol. 2, no. c, 2000.
10. B. Li, Y. Wang, H. K. Lee, A. Dempster, and C. Rizos, "Method for yielding a database of location fingerprints in WLAN," *IEE Proceedings-Communications*, vol. 152, no. 5, pp. 580–586, 2005.
11. B. Li, J. Salter, A. G. Dempster, and C. Rizos, "Indoor positioning techniques based on wireless LAN," in *LAN, First IEEE International Conference On Wireless Broadband And Ultra Wideband Communications*, 2006, vol. CD-ROM pro, pp. 13–16.
12. J. Machaj, P. Brida, and R. Piche, "Rank based fingerprinting algorithm for indoor positioning," *2011 Int. Conf. Indoor Position. Indoor Navig.*, pp. 1–6, Sep. 2011.
13. B. Shin, J. H. Lee, T. Lee, H. S. Kim, B. S. -, J. H. L. -, T. L. -, and H. S. K. -, "Enhanced Weighted K-Nearest Neighbor Algorithm for Indoor Wi-Fi Positioning Systems," *Int. J. Networked Comput. Adv. Inf. Manag.*, vol. 2, no. 2, pp. 15–21, Oct. 2012.
14. I. Lee, M. Kwak, and D. Han, "A Dynamic k -Nearest Neighbor Method for WLAN-Based Positioning Systems," *J. Comput. Inf. Syst.*, vol. 56, no. 4, pp. 295–300, 2016.
14. C. Laoudias, G. Constantinou, M. Constantinides, S. Nicolaou, D. Zeinalipour-Yazti, and C. G. Panayiotou, "Demo: the airplace indoor positioning platform," *Proc. 10th Int. Conf. Mob. Syst. Appl. Serv. - MobiSys '12*, p. 467, 2012.